

NUMERICAL MODELING OF LINEAR AND NONLINEAR SEISMIC WAVE ATTENUATION

**J. Bernard Minster
Heming Xu**

Institute of Geophysics and Planetary Physics
University of California, San Diego

Steven M. Day

Department of Geological Sciences
San Diego State University

Final Report to
Air Force Office of Scientific Research

April 1998

Project Title: Nonlinear Nearfield Wave Propagation
in an Endochronic Solid

Grant Number: F49620-94-1-0204

Period: March 15, 1994 - March 14, 1998

DTIC QUALITY INSPECTED 4

20000804 207

REPORT DOCUMENTATION PAGE AFRL-SR-BL-TR-00-

Public reporting burden for this collection of information is estimated to average 1 hour per response, including gathering and maintaining the data needed, and completing and reviewing the collection of information. Send comments regarding this burden estimate or any other aspect of this collection of information, including suggestions for reducing this burden to Washington Headquarters Services, Directorate for Information Operations and Reports, 1215 Jefferson Davis Highway, Suite 1204 Arlington, VA 22202-4302, and to the Office of Management and Budget, Paperwork Reduction Project (0704-01888) Washington, D.C. 20503.

0344

sources,
of this

1. AGENCY USE ONLY (Leave blank)		2. REPORT DATE April 1998	3. REPORT TYPE AND DATES COVERED Final technical report (3/15/94-3/14/98)	
4. TITLE AND SUBTITLE Numerical Modeling of Linear and Nonlinear Seismic Wave Attenuation			5. FUNDING NUMBERS grant F49620-94-1-0204	
6. AUTHOR(S) J. Bernard Minster, Heming Xu, and Steven M. Day				
7. PERFORMING ORGANIZATION NAME(S) AND ADDRESS(ES) University of California, San Diego Scripps Institution of Oceanography IGPP (0225) La Jolla, CA 92093			8. PERFORMING ORGANIZATION REPORT NUMBER	
9. SPONSORING/MONITORING AGENCY NAME(S) AND ADDRESS(ES) AFOSR/PKA 110 Duncan Avenue, Room B115 Bolling AFB DC 20332-8050			10. SPONSORING /MONITORING AGENCY REPORT NUMBER	
11. SUPPLEMENTARY NOTES				
12a. DISTRIBUTION/AVAILABILITY STATEMENT approved for public release; distribution unlimited.			12b. DISTRIBUTION CODE	
13. ABSTRACT (Maximum 200 words) CTBT verification requires an understanding of the propagation of seismic phases over complex regional paths which cut across major structural boundaries. The computation of synthetic seismograms by finite difference methods plays an important role in developing such understanding. In order for synthetic seismograms to be realistic, the models must account not only for regional elastic structure of the path, but also for anelastic losses. In addition, high amplitudes near the source require that numerical models take account of nonlinearity. Heretofore, 3D finite difference simulations have generally neglected attenuation, due in large part to the onerous storage requirements entailed by realistic seismic Q models. We describe a novel solution to this problem which we call memory-variable coarse-graining. The coarse-graining method leads to an order of magnitude reduction in computer storage requirements for anelastic memory variables. We then develop and demonstrate a method for modeling nonlinear wave propagation in rock under conditions of intermediate strain, defined as strain levels below the threshold for failure and damage, but above the threshold for onset of nonlinear response. The resulting model reproduces the stress-strain behavior of rock in this strain regime, as measured in quasi-static laboratory tests, and is consistent with key features of laboratory wave propagation measurements.				
14. SUBJECT TERMS CTBT verification, nonlinear wave propagation			15. NUMBER OF PAGES 78	
			16. PRICE CODE	
17. SECURITY CLASSIFICATION OF REPORT unclassified	18. SECURITY CLASSIFICATION OF THIS PAGE unclassified	19. SECURITY CLASSIFICATION OF ABSTRACT unclassified	20. LIMITATION OF ABSTRACT SAR	

NSN 7540-01-280-5500 Standard Form 298 (Rev 2-89)

Prescribed by ANSI Std. Z39-18
298-102

DTIC QUALITY INSPECTED 4

03-07-00 P10:37 16

TABLE OF CONTENTS

1.	Summary	1
	1.1 Overview	1
	1.2 Summary of Section 2	1
	1.3 Summary of Section 3	2
2.	Efficient simulation of constant Q using coarse-grained memory variables	4
	2.1 Abstract	4
	2.2 Introduction	5
	2.3 Anelasticity and memory variables	6
	2.4 Coarse graining of memory variables	9
	2.5 Numerical Example	16
	2.6 Discussion	18
	2.7 Summary	20
	2.8 References	22
3.	Model for nonlinear wave propagation derived from rock hysteresis measurements	33
	3.1 Abstract	33
	3.2 Introduction	34
	3.3 Background	35
	3.4 Implementation of the endochronic model	40
	3.5 Fitting quasi-static laboratory data	44
	3.6 Nonlinear wave propagation	46
	3.7 Discussion	53
	3.8 Conclusions	55
	3.9 References	57

1. SUMMARY

1.1 OVERVIEW

This project addresses the problem of incorporating seismic wave attenuation into numerical modeling codes which use time stepping to integrate the equations of motion. Such codes include time domain finite difference and finite element methods. CTBT verification requires an understanding of the propagation of regional seismic phases over complex regional paths which cut across major structural boundaries. The computation of synthetic seismograms by finite difference methods, 2D and 3D, plays an important role in developing such understanding. In order for ground motion estimates to be realistic, however, the models must account not only for regional elastic structure of the path, but also for anelastic losses; in the case of high-amplitude, near source parts of the propagation path, nonlinear losses influence the signal as well, and a comprehensive numerical model should be able to simulate realistic nonlinear attenuation.

We report work done under Grant No. F49620-94-1-0204 during the period March 1994 through March 1997. This work has been done in coordination with a parallel effort led by Steven M. Day at the San Diego State University (Grant F49620-94-1-0205). Section 2 addresses the computational problem of modeling realistic linear, anelastic attenuation in 2D and 3D. Heretofore, 3D finite difference simulations have generally neglected attenuation, due in large part to the onerous storage requirements entailed by realistic seismic Q models. We describe a novel solution to this problem which we call memory-variable coarse-graining. The coarse-graining method leads to an order of magnitude reduction in computer storage requirements for anelastic memory variables.

Section 3 develops and demonstrates a method for modeling nonlinear wave propagation in rock under conditions of intermediate strain, defined as strain levels below the threshold for failure and damage, but above the threshold for onset of nonlinear response. We develop a model which reproduces the stress-strain behavior of rock in this strain regime, as measured in quasi-static laboratory tests, and show that the resulting model is consistent with key features of laboratory wave propagation measurements.

1.2 SUMMARY OF SECTION 2 -- ANELASTIC COARSE-GRAINING

Improvements in computing speed have progressively increased the usable bandwidth of seismic wavefield simulations computed with time-stepped numerical schemes (e.g., finite difference, finite element, pseudospectral). As computational bandwidth increases, anelastic losses become increasingly significant for some important applications such as earthquake ground motion modeling, whole earth seismogram

simulation, and exploration seismic profile modeling, and these losses need to be included in the simulations. As bandwidth increases, however, the memory variables necessary to incorporate realistic anelastic losses account for an increasing proportion of total computational storage requirements, a consequence of the broad relaxation spectrum of typical earth materials. To reduce these storage requirements, we introduce a new method in which the memory variables are coarse-grained, i.e., redistributed in such a way that only a single relaxation time is represented at each node point (and therefore a single memory variable per stress component is required). Guided by a perturbation analysis, we effect this redistribution in such a way that spatial variability of this single relaxation time simulates the full relaxation spectrum. Such coarse-graining reduces memory-variable storage requirements by a factor of 8 for 3D problems, or a factor of 4 for 2D problems.

In fourth-order finite difference computations for the 3D acoustic wave equation, the method simulates frequency-independent Q within a 3% tolerance over 2 decades in frequency, and is highly accurate and free of artifacts over the entire usable bandwidth of the underlying finite difference scheme. These results should also hold for the elastodynamic equations. The method is readily generalized to approximate specific frequency-dependent Q models such as power laws, or to further reduce memory requirements. In its present implementation, the main limitation of the method is that it generates artifacts at wavelengths equal to 4 grid cell dimensions and shorter, which may, in some limited circumstances, overlap the usable bandwidth of very high-order finite difference and/or pseudospectral schemes.

1.3 SUMMARY OF PART II -- NONLINEAR WAVE PROPAGATION

We develop a method for modeling nonlinear wave propagation in rock at intermediate strain levels, i.e., strain levels great enough that nonlinearity cannot be neglected, but low enough that the rock does not incur macroscopic damage. The constitutive model is formulated using a singular-kernel endochronic formalism, and this formulation is shown to satisfy a number of general observational constraints, including producing a power law dependence of attenuation (Q^{-1}) on strain amplitude. Once the elastic modulus is determined, and a second parameter fixed to give Q^{-1} linear in the strain amplitude, the model has 2 remaining free parameters. One of these represents cubic anharmonicity, and we set it to agree with laboratory observations of harmonic distortion. The other parameter controls the amount of hysteresis, and it is set to approximate stress-strain curves measured in laboratory uniaxial stress experiments on Berea sandstone by Boitnott and Haupt. The constitutive equations, though fundamentally nonlinear and rate-independent, have a superficial, formal resemblance to viscoelasticity, which we exploit to produce an efficient, stable numerical algorithm. We solve 1D wave propagation problems for this constitutive model using both finite difference and pseudospectral methods. These

methods are shown to reproduce, to high precision, analytical results for quasi-harmonic wave propagation in a nonlinearly elastic medium.

Application of the Berea sandstone model to quasi-harmonic wave propagation shows several departures from results obtained with nonlinear elasticity. The Berea model shows more rapid decay with distance of the fundamental frequency component, due to nonlinear, amplitude-dependent attenuation, than does nonlinear elasticity. The Berea model also shows enhanced excitation of the order 3 harmonic, in agreement with laboratory observations. In addition, the growth with propagation distance of the harmonics of the source excitation shows a saturation, relative to the nonlinear elasticity results. This behavior reflects the competing effects of amplitude growth via energy transfer from the source frequency, and energy dissipation due to hysteresis, the dissipation increasing as the harmonic amplitude grows. In additional numerical experiments, we find that a two-frequency source function generates harmonics with frequencies which can be expressed as linear combinations of integer multiples of the two source frequencies, in agreement with published laboratory results for other solids.

2. EFFICIENT SIMULATION OF CONSTANT Q USING COARSE-GRAINED MEMORY VARIABLES

Steven M. Day

2.1 ABSTRACT

Improvements in computing speed have progressively increased the usable bandwidth of seismic wavefield simulations computed with time-stepped numerical schemes (e.g., finite difference, finite element, pseudospectral). As computational bandwidth increases, anelastic losses become increasingly significant for some important applications such as earthquake ground motion modeling, whole earth seismogram simulation, and exploration seismic profile modeling, and these losses need to be included in the simulations. As bandwidth increases, however, the memory variables necessary to incorporate realistic anelastic losses account for an increasing proportion of total computational storage requirements, a consequence of the broad relaxation spectrum of typical earth materials. To reduce these storage requirements, we introduce a new method in which the memory variables are coarse-grained, i.e., redistributed in such a way that only a single relaxation time is represented at each node point (and therefore a single memory variable per stress component is required). Guided by a perturbation analysis, we effect this redistribution in such a way that spatial variability of this single relaxation time simulates the full relaxation spectrum. Such coarse-graining reduces memory-variable storage requirements by a factor of 8 for 3D problems, or a factor of 4 for 2D problems.

In fourth-order finite difference computations for the 3D acoustic wave equation, the method simulates frequency-independent Q within a 3% tolerance over 2 decades in frequency, and is highly accurate and free of artifacts over the entire usable bandwidth of the underlying finite difference scheme. These results should also hold for the elastodynamic equations. The method is readily generalized to approximate specific frequency-dependent Q models such as power laws, or to further reduce memory requirements. In its present implementation, the main limitation of the method is that it generates artifacts at wavelengths equal to 4 grid cell dimensions and shorter, which may, in some limited circumstances, overlap the usable bandwidth of very high-order finite difference and/or pseudospectral schemes.

2.2 INTRODUCTION

As computing has become progressively cheaper, it has become possible to use discrete numerical methods such as the finite difference and finite element methods to synthesize seismic wavefields over spatial domains which are relatively large compared with the minimum numerically resolvable wavelength. When a seismic pulse propagates a distance many times its dominant wavelength, anelastic attenuation cannot generally be ignored. Even three dimensional elastodynamic problems can now be solved over domains sufficiently large that attenuation should not be neglected, and the problem of modeling attenuation efficiently and accurately will become increasingly important as computational capabilities advance. Accurate treatment of anelastic attenuation has already become a priority in some important practical applications in 3D, including, for example, the modeling of earthquake strong ground motion in sedimentary basins (e.g., Frankel and Vidale, 1992; Graves, 1993; Yomogida and Etgen, 1993; Olsen et al., 1995a), synthesis of the elastic response of whole earth models (e.g., Yoon and McMechan, 1995; Igel and Weber, 1995) and the simulation of seismic reflection profiles (e.g., Carcione et al. 1992). Applications such as these now frequently entail three-dimensional computations over domains with dimensions roughly two orders of magnitude larger than the minimum wavelength (e.g., Olsen et al., 1995b).

The most general anelastic law represents the stress at (\mathbf{x}, t) as a convolution integral over the complete strain history at \mathbf{x} , a form of the stress-strain relation which is not tractable for numerical calculations, since it imposes enormous storage and computational requirements. Day and Minster (1984) developed a framework for incorporating anelastic attenuation laws into time-stepped numerical methods such as the finite difference method by approximating them using internal, or "memory", variables. This approach can be viewed in the time domain as the replacement of the convolution operator by a low-order differential operator. Alternatively, it can be viewed in the Laplace transform domain as the approximation of an algebraic transfer function by a pole-zero representation. Each pole then corresponds to a memory variable which evolves according to a first-order differential equation analogous to that governing a standard linear solid. The latter can be time-stepped to compute the evolution of the memory variable(s) along with the other field variables such as velocity and stress. This framework has been refined and improved by a number of investigators, who have used a variety of methods to determine efficient pole-zero representations of the stress-strain relationship (e.g., Emmerich and Korn, 1987; Carcione et al., 1988; Witte and Richards, 1990; Krebs and Quiroga-Goode, 1994; Blanch et al., 1995).

While the memory variable framework is effective, it does impose stringent demands for computer memory. To approximate an anelastic quality factor (Q) which is approximately constant over a specified frequency band requires 2 to 3 memory variables per decade of bandwidth per stress component per computational unit cell, even under the

most highly optimized memory variable formulations (e.g., Robertsson et al., 1994; Blanch et al., 1995). This requirement becomes particularly onerous in 3D, where there are 6 independent stress components per computational unit cell. The typical 3D elastic (non-attenuative) staggered grid finite difference method requires 9 words of storage per unit cell for the field variables, i.e., the velocity and stress components. Anelastic computations in 3D, in contrast, would require the addition of roughly 30 memory variables per unit cell to achieve a near-constant Q over a bandwidth of 2 decades. Thus, the total memory requirement would be roughly quadrupled. It is therefore not surprising that, for example, none of the 3D simulations of basin response to earthquakes done to date have included anelastic memory variables.

We present a method that approximates constant Q to very high accuracy, over 2 to 3 decades of frequency, with a single memory variable per stress component per unit cell. The method is most efficient in higher dimensions. In 2D the method achieves a 4-fold reduction in memory variable storage requirements (to achieve Q constant over a given bandwidth), compared with the most efficient current methods. In 3D the method provides an 8-fold reduction. The operations count associated with the memory variable evolution is reduced in the same proportions.

The method is conceptually simple and easily implemented. Given an N -pole description of the anelastic relaxation function, we distribute the N memory variables over the stress node-points of the computational grid, one per stress component per unit cell, in such a way that spatial averages of the relaxation function remain well approximated. This procedure can be viewed as replacement of the microscopic relaxation structure of the medium with a coarse-grained equivalent.

The following section reviews the operational form of the stress-strain relationship of linear anelasticity, its representation in terms of a relaxation spectrum, and its approximation via first order differential equations governing a set of memory variables. The subsequent section analyzes the effect of coarse graining the memory variables. The analysis is approximate, and is intended to demonstrate the plausibility of the technique and to indicate how the evolutionary equations should be weighted in the coarse-grained medium to achieve the desired Q value. We then test the method with a numerical application to constant Q simulation in 3D. Finally, we discuss possible extensions, as well as limitations, of the method.

2.3 ANELASTICITY AND MEMORY VARIABLES

This section reviews the reduction of the one-dimensional, anelastic stress-strain relationship to differential form, resulting in its (approximate) expression in terms of N internal, or "memory", variables. In higher dimensions, there will be one such relationship for each independent stress component. Adhering to the notation of Day and Minster (1984), we write the one-dimensional stress-strain relation as a convolution integral over the step response M :

$$\sigma(t) = \int_0^t M(t-t') d\varepsilon(t'), \quad (1)$$

where σ is the stress and ε is the strain. We apply the Laplace transform in s-multiplied form, i.e.,

$$\bar{f}(s) = s \int_0^\infty f(t) e^{-st} dt, \quad (2)$$

to transform the stress-strain relation to its operational form:

$$\bar{\sigma}(s) = \bar{M}(s) \bar{\varepsilon}(s). \quad (3)$$

Note that the operational modulus \bar{M} has the same dimensions as the step response M . The unrelaxed modulus M_u , the relaxed modulus M_R , the relaxation of the modulus, δM , and the normalized relaxation function ϕ , are given by

$$M_u = M(0) = \bar{M}(\infty), \quad (4)$$

$$M_R = M(\infty) = \bar{M}(0), \quad (5)$$

$$\delta M = M_u - M_R, \quad (6)$$

and

$$M(t) = M_R + \delta M \phi(t). \quad (7)$$

We represent the relaxation function in terms of a relaxation spectrum Φ ,

$$\phi(t) = \int_{-\infty}^{\infty} e^{-t/\tau} \Phi(\ln \tau) d(\ln \tau), \quad (8)$$

resulting in the following integral expression for the operational modulus:

$$\bar{M}(s) = M_u - \delta M \int_{-\infty}^{\infty} \frac{\Phi(\ln \tau)}{s\tau + 1} d(\ln \tau), \quad (9)$$

which is equivalent to Equation 8 of Day and Minster (1984). We use (9) and the definition of Q^{-1} (as a function of angular frequency ω)

$$Q^{-1}(\omega) = \frac{\text{Im}[\bar{M}(i\omega)]}{\text{Re}[\bar{M}(i\omega)]}, \quad (10)$$

to get, in the low loss approximation ($Q^{-1} \ll 1$),

$$Q^{-1}(\omega) \approx \frac{\delta M}{M_u} \int_{-\infty}^{\infty} \frac{\omega \tau}{\omega^2 \tau^2 + 1} \Phi(\ln \tau) d(\ln \tau). \quad (11)$$

To reformulate (9) in differential form, we approximate the integral in (9) by a numerical quadrature, i.e., a sum over N discrete relaxation times τ_i ,

$$\int_{-\infty}^{\infty} \frac{\Phi(\ln \tau)}{s\tau + 1} d(\ln \tau) \approx \sum_{i=1}^N \frac{\lambda_i}{s\tau_i + 1}. \quad (12)$$

where the λ_i are the quadrature weights. Next, we substitute the approximation into (3) and invert the Laplace transform, obtaining

$$\sigma(t) = M_u \left[\varepsilon(t) - \sum_{i=1}^N \zeta_i(t) \right], \quad (13)$$

The ζ_i , $i=1, \dots, N$ are then internal, or memory, variables which evolve, respectively, according to the N first-order differential equations

$$\tau_i \frac{d\zeta_i(t)}{dt} + \zeta_i(t) = \lambda_i \frac{\delta M}{M_u} \varepsilon(t), \quad (14)$$

which are specified by the $2N$ values of τ_i and λ_i . The latter are, respectively, the poles and residues of the operational modulus (Day and Minster, 1984). Each stress component, at each computational node, thus has associated with it the N memory variables ζ_i . The resulting low-loss approximation to Q^{-1} is then

$$Q^{-1}(\omega) \approx \frac{\delta M}{M_u} \sum_{i=1}^N \frac{\lambda_i \omega \tau_i}{\omega^2 \tau_i^2 + 1} \quad (15)$$

The natural criterion on which to judge the approximation (12) is the degree to which the corresponding approximation (15) to $Q^{-1}(\omega)$ matches the exact value (11). Most seismic applications entail approximating a $Q^{-1}(\omega)$ which is nearly constant over a broad frequency range. To accomplish this, Day and Minster (1984) transformed the integration variable in (9) to τ^{-1} and applied Gaussian quadrature to derive analytical expressions for the poles and residues τ_i and λ_i (and showed that this is equivalent to a Padé approximant of the operational modulus). Subsequent investigators have made substantial improvements by using numerical optimization to determine the τ_i and λ_i , usually leading to roughly uniform distribution of the poles over $\ln(\tau)$ (e.g., Emmerich

and Korn, 1987). For practical purposes, about 1 pole per octave is sufficient (Robertsson et al., 1994; Blanch et al., 1995) to approximate a frequency independent Q function.

2.4 COARSE GRAINING OF MEMORY VARIABLES

Outline of the Method

Our objective is to reduce the number of memory variables to at most 1 per stress component per node, without sacrificing accuracy in representing $Q(\omega)$. We do so by introducing a single, spatially variable, relaxation time $\tau(\mathbf{x})$, together with a weighting function $w(\mathbf{x})$, in place of the spectrum of relaxation times in (8). Then, in place of (13), we write

$$\sigma(\mathbf{x}, t) = M_u [\varepsilon(\mathbf{x}, t) - \zeta(\mathbf{x}, t)], \quad (16)$$

where ζ satisfies

$$\tau(\mathbf{x}) \frac{d\zeta(\mathbf{x}, t)}{dt} + \zeta(\mathbf{x}, t) = w(\mathbf{x}) \frac{\delta M}{M_u} \varepsilon(\mathbf{x}, t). \quad (17)$$

We will show by analysis and numerical examples that this method can be made highly successful when the relaxation time function $\tau(\mathbf{x})$ and weight function $w(\mathbf{x})$ satisfy two conditions. First, $\tau(\mathbf{x})$ and $w(\mathbf{x})$ should be constructed so that their spatial distributions approximate the target relaxation spectrum, in the sense described in the next paragraph. Second, the scale length of their spatial variability should be limited to a few times the computational cell dimension, as shown by the perturbation analysis in the next section.

Note that $\Phi(\ln \tau)$ in Eqn. 8 is non-negative and has unit area. We can thus think of $\Phi(\ln \tau)$ as a probability density function, in which case the integral in (9) defining the operational modulus would be the expected value of $(s\tau + 1)^{-1}$ when $\ln \tau$ is sampled from the distribution Φ . It is natural to specify $\tau(\mathbf{x})$ such that it is analogously distributed, in the following sense. Choose $\tau(\mathbf{x})$ to be a measurable function on domain X , and define the set A by

$$A = \{\mathbf{x} : \ln \tau(\mathbf{x}) < a\} \quad (18)$$

where a is a real number. We introduce a measure ν , such that the measure of a subset E of X is defined by

$$\nu(E) = \int_E w(\mathbf{x}) dV, \quad (19)$$

where $w(\mathbf{x})$ is a Lebesgue-measurable, non-negative function having unit mean value on domain X . This means that

$$\nu(X) = m(X), \quad (20)$$

where m is the Lebesgue measure of X (i.e., the volume of the domain of interest). Then we would specify $\tau(x)$ such that the measure of A , $v(A)$, satisfies

$$\frac{v(A)}{v(X)} = \int_{-\infty}^a \Phi(\ln \tau) d(\ln \tau), \quad (21)$$

for all real a . In other words, given a $w(x)$ satisfying (20), we specify $\tau(x)$ such that, if spatial points were sampled randomly, with probability weighted by $w(x)$, the resulting $\ln \tau$ samples would have distribution Φ . In practice, of course, we will only need to specify w and τ at a discrete set of computational nodes.

There are actually two distinct scales of spatial variation implicit in Equation 17. The micro-scale (sub-wavelength) variation which we have just discussed, and which is designed to simulate the relaxation spectrum, is indicated explicitly by the notation in (17). Equation 17, however, does not explicitly note the spatial variation of the factor $\delta M/M_\infty$, though it too may vary spatially. This factor, however, scales the *macroscopic* Q , and its variation will usually have a scale length larger than that of τ and w .

We will refer to the conventional description of anelasticity, as given by Eqn 9, as the "relaxation-spectrum" representation. We will call the method based on a heterogeneous relaxation time, as given by Eqns 16 and 17, the "coarse-grain" representation, in accordance with the physical analogy described below.

Physical analogue

Some motivation for this approach and terminology may be found in the physical origin of the relaxation spectra of earth materials. The characteristic attenuative behavior of rock results from the fact that rock is a heterogeneous aggregate. Relaxation mechanisms corresponding to a broad range of scale lengths and activation energies are present on the microscopic level (see, e.g., Minster, 1980). When the material is deformed over wavelengths large compared to the scale of the heterogeneities, these relaxation mechanisms are activated concurrently, giving rise to a broad spectrum of relaxation times. Conventionally, these relaxations are subsumed into a constitutive equation describing the mean behavior of the aggregate. Our method, in a sense, reverses this synthesis. We revert to the more fundamental, heterogeneous description of the relaxations, albeit in an artificial, coarser-grained aggregate, with "grain size" equal to the computational unit cell. In this coarse aggregate, each computational unit cell has only a single relaxation time.

In discrete time-stepped numerical wave propagation computations (e.g., finite difference, finite element, pseudospectral), the minimum wavelength which can be computed accurately necessarily exceeds several times the cell size of the grid. Thus, it is plausible that we can coarse-grain the medium in such a way that its attenuative properties will be preserved for all wavelengths of computational interest. The following analysis of

the coarse-grain representation by means of perturbation theory suggests that this is indeed the case.

Analysis of the method

In the coarse-grain representation of the medium, the effective attenuation can no longer be regarded as a purely local process with properties derivable from constitutive equations alone. To understand the nature of the approximation, it is necessary to introduce the elastodynamic equations into the analysis. We begin with the well-known analysis, via perturbation theory, of anelastic attenuation in terms of an eigenfunction expansion of the elastodynamic field. We simplify the analysis, without sacrificing any useful insights, by restricting consideration to wavefields in a bounded volume (and by neglecting issues raised by eigenfrequency degeneracy).

In a finite volume V with homogeneous boundary conditions, all solutions to the elastodynamic equations (without anelastic losses) can be written as linear combinations of $\mathbf{u}_n(\mathbf{x})e^{i\omega_n t}$, $n=1,2 \dots$, where \mathbf{u}_n is the (normalized) eigenfunction belonging to the eigenvalue ω_n^2 of the operator H^0 given by

$$H_i^0(\mathbf{u}) = \rho^{-1} \left(C_{ijpq}^0 u_{p,q} \right)_{,j} \quad (22)$$

In (22), $\mathbf{u}(\mathbf{x})e^{i\omega t}$ is the displacement field, $\rho(\mathbf{x})$ the density, and $\mathbf{C}^0(\mathbf{x})$ the elastic tensor. The eigenvalues are positive and the eigenvectors are orthogonal under the inner product defined by

$$(\mathbf{f}, \mathbf{g}) = \int_V \mathbf{f}(\mathbf{x}) \cdot \mathbf{g}^*(\mathbf{x}) \rho(\mathbf{x}) dV. \quad (23)$$

The introduction of weak, anelastic attenuation has the effect of adding a small additional, frequency dependent term H' to H^0 . The new operator H is then

$$H = H^0 + H', \quad (24)$$

where

$$H_i'(\mathbf{u}) = \rho^{-1} \left(C'_{ijpq} u_{p,q} \right)_{,j} \quad (25)$$

Each component of \mathbf{C}' has the form of the second term on the right hand side of (9), evaluated at $s=i\omega$. The resulting perturbation to the eigenvalue ω_n^2 can be estimated from perturbation theory. The first-order correction $\delta\omega_n^2$ to the eigenvalue is

$$\delta\omega_n^2 = (H'(\mathbf{u}_n), \mathbf{u}_n), \quad (26)$$

where \mathbf{u}_n is the normalized, unperturbed eigenfunction of H^0 . The temporal Q_n^{-1} (Aki and Richards, 1980) of the mode, Q_n^{-1} , can be expressed in terms of $\delta\omega_n$, to first order in the components of \mathbf{C}' , as

$$\begin{aligned} Q_n^{-1} &= 2\omega_n^{-1} \text{Im}(\delta\omega_n), \\ &= \omega_n^{-2} \text{Im}(H'(\mathbf{u}_n), \mathbf{u}_n) \end{aligned} \quad (27)$$

To simplify the subsequent discussion, we now specialize to the case of an isotropic medium, though this assumption is not essential to the analysis. To begin with, we consider the relaxation-spectrum representation of the medium. We take a normalized relaxation spectrum Φ which is independent of position \mathbf{x} (though this assumption is not essential either). Then we can find H' from (9), replacing M and δM by their bulk and shear modulus equivalents:

$$H'(\mathbf{u}) = -\rho^{-1} \left(\delta\kappa \epsilon_{kk} \delta_{ij} + 2\delta\mu \epsilon'_{ij} \right)_{,j} \int_{-\infty}^{\infty} \frac{\Phi(\ln \tau)}{1 + i\omega\tau} d \ln \tau, \quad (28)$$

where ϵ is the infinitesimal strain tensor and ϵ' its deviatoric part, and κ and μ denote, respectively, bulk and shear moduli. Then, substituting (28) in (27), and applying the divergence theorem and the boundary conditions, we obtain

$$Q_n^{-1} = \omega_n^{-2} \int_{-\infty}^{\infty} D_{\omega_n}(\tau) \Phi(\ln \tau) d \ln \tau \int_V \left[\left(\frac{\delta\kappa}{\kappa_n} \right) \kappa_n \epsilon_{(n)ij} \epsilon'_{(n)kk} + \left(\frac{\delta\mu}{\mu_n} \right) 2\mu_n \epsilon'_{(n)jk} \epsilon'_{(n)jk} \right] dV, \quad (29)$$

where ϵ_n and ϵ'_n are strain tensors associated with the eigenvector \mathbf{u}_n , and $D_{\omega}(\tau)$ is defined by

$$D_{\omega}(\tau) \equiv \frac{\tau\omega}{1 + \tau^2\omega^2}. \quad (30)$$

Recalling our reinterpretation of $\Phi(\ln \tau)$ as a probability density function, we can interpret the first integral in (29) as the expected value of $D_{\omega_n}(\tau)$. Denoting this expected value by $\langle D_{\omega_n} \rangle$, and also introducing $E_{n\kappa}$ and $E_{n\mu}$ to denote, respectively, the bulk and shear strain energy densities of mode n , we can write (29) in the form

$$Q_n^{-1} = \omega_n^{-2} \int_V \left(2 \frac{\delta\kappa}{\kappa_n} E_{n\kappa} \langle D_{\omega_n} \rangle + 4 \frac{\delta\mu}{\mu_n} E_{n\mu} \langle D_{\omega_n} \rangle \right) dV. \quad (31)$$

Now we are ready to introduce the coarse-grain representation, as given by Eqn 16-21. Therefore, we drop the integral over the relaxation spectrum, i.e., $\langle D_{\omega_n} \rangle$, in our representation of H' , and instead allow the relaxation time τ to be a function of position,

$\tau(\mathbf{x})$, as described earlier. The result is that $\langle D_{\omega_n} \rangle$ in (31) is replaced by $w(\mathbf{x})D_{\omega_n}(\tau(\mathbf{x}))$. We denote by \tilde{Q}_n the resulting approximation to the temporal Q of mode n . Then, \tilde{Q}_n^{-1} is

$$\tilde{Q}_n^{-1} = \omega_n^{-2} \int_V \left(2 \frac{\delta\kappa}{\kappa_u} E_{\kappa} D_{\omega_n}(\tau(\mathbf{x})) + 4 \frac{\delta\mu}{\mu_u} E_{\mu} D_{\omega_n}(\tau(\mathbf{x})) \right) w(\mathbf{x}) dV. \quad (32)$$

We can assess the coarse-grain representation by evaluating the accuracy of (32) as an approximation to (31), since the latter is the relaxation-spectrum representation of the eigenfunction attenuation. The comparison is more informative with the further simplification that $\delta\kappa/\kappa_u$ and $\delta\mu/\mu_u$ are spatially uniform. From its method of construction, we know that the volume average of $w(\mathbf{x})D_{\omega_n}(\tau(\mathbf{x}))$ is also equal to the expected value $\langle D_{\omega_n} \rangle$ (see Eqns 18-21). We write $\bar{E}_{n\kappa}$ and $\bar{E}_{n\mu}$ for the corresponding volume averages of $E_{n\kappa}$ and $E_{n\mu}$, and (31) simplifies to

$$Q_n^{-1} = 2\omega_n^{-2} V \left(\frac{\delta\kappa}{\kappa_u} \bar{E}_{n\kappa} + \frac{\delta\mu}{\mu_u} \bar{E}_{n\mu} \right) \langle D_{\omega_n} \rangle. \quad (33)$$

The corresponding expression for attenuation of the eigenfunction in the coarse-grain representation is

$$\begin{aligned} \tilde{Q}_n^{-1} &= 2\omega_n^{-2} \left[\frac{\delta\kappa}{\kappa_u} \int_V E_{n\kappa}(\mathbf{x}) D_{\omega_n}(\tau(\mathbf{x})) w(\mathbf{x}) dV + 2 \frac{\delta\mu}{\mu_u} \int_V E_{n\mu}(\mathbf{x}) D_{\omega_n}(\tau(\mathbf{x})) w(\mathbf{x}) dV \right] \\ &= Q_n^{-1} + 2\omega_n^{-2} \left(\frac{\delta\kappa}{\kappa_u} C_{\kappa} + 2 \frac{\delta\mu}{\mu_u} C_{\mu} \right) \end{aligned} \quad (34)$$

The C_{κ} and C_{μ} in (34) are just the spatial correlations of $w(\mathbf{x})D_{\omega_n}(\tau(\mathbf{x}))$ with the bulk and shear strain energy densities, respectively:

$$C_M = \int_V [E_{nM}(\mathbf{x}) - \bar{E}_{nM}] [w(\mathbf{x})D_{\omega_n}(\tau(\mathbf{x})) - \overline{wD_{\omega_n}}] dV, \quad (35)$$

where M refers to either κ or μ , and $\overline{wD_{\omega_n}}$ is the volume average of $w(\mathbf{x})D_{\omega_n}(\tau(\mathbf{x}))$. We have used the equality between $\overline{wD_{\omega_n}}$ and $\langle D_{\omega_n} \rangle$ in deriving (34) and (35). Eqn. 35 states that the error introduced by the coarse-grain representation, relative to the relaxation-spectrum representation, is proportional to the degree of spatial correlation between the modal strain energy density and the function $w(\mathbf{x})D_{\omega_n}(\tau(\mathbf{x}))$.

We should be able to minimize the correlation of $w(\mathbf{x})D_{\omega_n}(\tau(\mathbf{x}))$ with all modes of practical interest by making $\tau(\mathbf{x})$ and $w(\mathbf{x})$ periodic in space, with wavelength short compared with the minimum wavelength at which the numerical wave propagation computation (e.g., finite difference, etc.) is considered accurate. We assess this strategy by

examining (34) and (35) in the simplified case of plane wave excitation of a uniform, 1D acoustic medium.

In this special case, the eigenfunction has the form

$$u_n(x) = B \cos(\omega_n x / \alpha), \quad (36)$$

(apart from an irrelevant phase shift), where α is the wavespeed and B is a constant. The deviation of the strain energy density from its mean value of $\frac{1}{4} \kappa_u (\omega_n B / \alpha)^2$ is

$$E_{n\kappa}(x) - \bar{E}_{n\kappa} = -\frac{1}{4} \kappa_u (\omega_n B / \alpha)^2 \cos(2\omega_n x / \alpha), \quad (37)$$

which has 1/2 the wavelength of the eigenfunction. We will assume that $w(x)$ and $\tau(x)$ are periodic, with period L , i.e., $\tau(x) = \tau(x - mL)$ for integer m , and similarly for w . Then the function $w(x)D_{\omega_n}(\tau(x))$ is also periodic with period L , and therefore has a Fourier series representation, the zeroth order term of which is just $\overline{wD_{\omega_n}}$, so that the deviation of $w(x)D_{\omega_n}(\tau(x))$ from its mean is

$$w(x)D_{\omega_n}(\tau(x)) - \overline{wD_{\omega_n}} = \sum_{j=1}^{\infty} a_j \cos(2\pi j x / L) + \sum_{j=1}^{\infty} b_j \sin(2\pi j x / L). \quad (38)$$

Combining (37) and (38) with (35), we find that the correlation C_{κ} is only appreciable when the condition

$$j \left(\frac{2\pi\alpha}{\omega_n} \right) = 2L, \quad j \geq 1, \quad (39)$$

is satisfied, where $2\pi\alpha/\omega_n$ is the wavelength. Therefore, the largest value of wavelength for which the error in the coarse-grain representation is significant is $2L$. In other words, the estimated error is only significant when the wavelength is less than or equal to twice the periodicity of the relaxation time function $\tau(x)$. Note, by the way, that (39) is just the Bragg condition for backscatter at normal incidence to the scattering plane.

Implementation

Eqn. 39 implies a bandwidth limitation in the coarse-grain method. Our strategy for its implementation is to match this short-wavelength cutoff to the short-wavelength limit already present in discrete numerical methods. We make $w(x)$ and $\tau(x)$ periodic, with period equal to twice the computation unit cell dimension. According to (39), this period-two coarse-graining will not result in significant error for wavelengths longer than 4 unit-cell dimensions. For relatively low-order finite difference methods, including the widely

used fourth order staggered grid methods (e.g., Levander, 1988), wavelengths shorter than 4 unit-cell dimensions suffer strong numerical dispersion and are therefore already subject to large errors. Thus, any spurious effects of period-two coarse-graining should be isolated at wavelengths which are already outside the usable bandwidth of the wave propagation calculations. High-order finite difference methods and pseudospectral methods are less restricted by numerical dispersion, but suffer other limitations associated with the representation of material interfaces (Witte and Richards, 1990) when the wavelength is shorter than 4 times the cell dimension, and the period-two coarse-grain method may turn out to be satisfactory in those applications as well.

In 3D, this 2-unit-cell periodicity allows for 8 different values of τ at grid nodes. To be specific, if this chosen set of discrete relaxation times is τ_k , $k=1,\dots,8$, and unit cells are indexed by integers p,q,r , such that stress nodes are centered at $\mathbf{x} = p\mathbf{a}_1 + q\mathbf{a}_2 + r\mathbf{a}_3$, then

$$\tau(\mathbf{x}) = \tau_{1+p \bmod 2 + 2(q \bmod 2) + 4(r \bmod 2)}, \quad (40)$$

and $w(\mathbf{x})$ has a similar discrete representation

$$w(\mathbf{x}) = w_{1+p \bmod 2 + 2(q \bmod 2) + 4(r \bmod 2)}. \quad (41)$$

Since this approach only permits a discrete set of relaxation times (8 in 3D) to be realized, implementation of criterion (21) requires first developing a discrete approximation to the continuous relaxation spectrum, i.e.,

$$\Phi(\ln \tau) \approx \sum_{i=1}^N \lambda_i \delta(\ln \tau - \ln \tau_i), \quad (42)$$

as in (12). This is the same step required in the generation of a conventional memory variable representation, and any of the optimization methods proposed in the literature (e.g., Emmerich and Korn, 1987; Carcione et al., 1988; Witte and Richards, 1990; Blanch et al. 1995) for generating conventional memory variable representations can be used at this point. Once the continuous spectrum is replaced by the discrete spectrum, the conditions defined by (18-21) will be satisfied if the w_i are identified with the quadrature weights λ_i , but normalized to have unit volumetric mean. Since the normalization of Φ implies that the λ_i sum to 1, we then have

$$w_i = N\lambda_i, \quad (43)$$

where N is 8 in 3D or 4 in 2D. Fig. 1 illustrates this period-two scheme.

Eight relaxation times should be sufficient to approximate a frequency-independent $Q(\omega)$ with very high accuracy over roughly 3 decades in frequency. In 2D, the 2-unit-cell periodicity allows for 4 distinct values of τ , adequate to approximate frequency-

independent $Q(\omega)$ over one and a half decades or more. Compared with a conventional memory variable method, i.e., one in which the memory variables are not coarse grained, the coarse-grain method with 2-unit-cell periodicity can approximate $Q(\omega)$ with the same accuracy, but reduces the memory requirement by a factor of 8 in 3D and a factor of 4 in 2D.

2.5 NUMERICAL EXAMPLE

The above analysis is approximate, and a numerical test is necessary to establish the practical accuracy of the coarse-grain method. In this section, we test its period-two implementation for the case of a plane wave in a uniform, 3D acoustic medium, with Q approximately frequency-independent. We solve the 3D acoustic equations using a staggered grid method, fourth order in space and second order in time (Graves, 1996, describes the corresponding algorithm for the elastodynamic equations). Eqn 17 is time stepped using the formula

$$\zeta(\mathbf{x}, t + \delta t) = \zeta(\mathbf{x}, t) e^{-\delta/\tau(\mathbf{x})} + w(\mathbf{x}) \frac{\delta\kappa}{\kappa_u} \frac{1}{2} [\varepsilon(\mathbf{x}, t) + \varepsilon(\mathbf{x}, t + \delta t)] [1 - e^{-\delta/\tau(\mathbf{x})}]. \quad (44)$$

A relaxation spectrum, constant on its support interval $(\ln\tau_m, \ln\tau_M)$ yields a good approximation to a frequency independent Q for $\tau_M^{-1} \ll \omega \ll \tau_m^{-1}$ (this is a change of notation from Day and Minster, 1984, in that τ_m and τ_M correspond to their τ_1 and τ_2). If ω_0 is a reference frequency near the center of the absorption band, then $Q_0^{-1} \equiv Q^{-1}(\omega_0)$ is given approximately by

$$Q_0^{-1} \approx \frac{\pi\delta\kappa}{2\kappa_u} \left[\ln\left(\frac{\tau_M}{\tau_m}\right) + \frac{\delta\kappa}{\kappa_u} \ln(\omega_0 \tau_m) \right]^{-1}. \quad (45)$$

To approximate this absorption band, we take $w(\mathbf{x})$ equal to 1 everywhere, and prescribe $\tau(\mathbf{x})$ according to (40), with the $\ln\tau_k$ uniformly spaced over the interval $(\ln\tau_m, \ln\tau_M)$:

$$\ln \tau_k = \ln \tau_m + \frac{2k-1}{16} (\ln \tau_M - \ln \tau_m). \quad (46)$$

The plane wave is given an initial displacement pulse shape $u_0(t)$, where

$$u_0(t) = \frac{2\pi i}{T} e^{-2\pi i t/T}, \quad (47)$$

which is a broadband, minimum phase pulse with its spectral corner at frequency $1/T$. In the cases shown below, T is set equal to 10π times the propagation time across the unit

cell, so that the corner frequency corresponds to a wavelength of about 30 grid-cells. The propagation direction is parallel to one of the lattice vectors of the grid.

We have set the ratio τ_M/τ_m to 10^4 , with the objective of producing a nearly frequency independent Q for $10\tau_M^{-1} < \omega < 0.1\tau_m^{-1}$. Q_0 is defined at reference frequency ω_0 , which we set equal to the geometrical mean of τ_M^{-1} and τ_m^{-1} . We perform calculations for Q_0 of 100 and 20. The lower cutoff τ_m is set equal to $(2\pi)^{-1}$ times the propagation time across the unit cell.

Fig. 2 shows the pulse for the case Q_0 equal to 100, after it has propagated a distance of 26 times the corner wavelength. Fig. 2a shows the entire pulse, with the later, low-amplitude parts of the waveform magnified by factors of 100 and 1000. Fig. 2b shows the high amplitude part of the pulse on an expanded time scale. For comparison, both parts of Fig. 2 also show the exact solution, (based on the frequency-independent Q model of Kjartansson, 1979). It is evident that the coarse-grain method reproduces the analytical solution with very high accuracy. The small, negative precursor in the numerical solution is a consequence of ordinary numerical dispersion associated with the fourth order finite difference method, and is unrelated to the anelastic relaxation model.

Fig. 3 shows the corresponding results for Q_0 equal to 20. As in the previous case, the numerical and exact solutions are compared in the figure, with the late portion magnified in Fig. 3a and the early portion expanded in Fig. 3b. The numerical solution reproduces both the attenuation and physical dispersion of the exact solution with very high accuracy. Fig. 4 compares the analytical and numerical solutions again, this time after convolution with a Ricker wavelet with dominant frequency f_R equal to twice the corner frequency. Thus, the pulse has propagated 52 times its dominant wavelength. Again, numerical and analytical solutions are virtually indistinguishable, even at late times.

We can determine an apparent Q , denoted by $\hat{Q}(\omega)$, from the numerical solutions. We do this using spectral ratios of the pulse at successive locations, i.e.,

$$\hat{Q}^{-1}(\omega) = \frac{-2 \ln[u(x + \Delta x, \omega)/u(x, \omega)]}{\omega \alpha \Delta x}, \quad (48)$$

where Δx is the propagation distance between locations and α is the wavespeed. This operational definition of Q differs from that of Eqn 10, but at large values of Q , the difference is negligible (see, e.g., O'Connell and Budiansky, 1978). The difference can become significant for small Q , and this difference will become evident in our case when Q_0 equals 20.

Fig. 5 shows $\hat{Q}(\omega)$ for the numerical solution in the case $Q_0 = 100$. Four estimates are shown, corresponding to spectral ratios at successive 200 grid-cell intervals. The $\hat{Q}(\omega)$ curves are indistinguishable from one another over the entire range of frequencies from 10^3 grids per wavelength to 4 grids per wavelength. Thus, the coarse-grain method yields a spatially homogeneous attenuative behavior over the full range of usable frequencies present in the finite difference computations. The variability of the curves at wavelengths

longer than 10^3 grid-cells is simply a result of the shorter pulse durations available for Fourier analysis at greater distances (due to later arrival times), 10^3 grids per wavelength corresponding to a period equal to the total post-arrival duration of the computation at the most distant location. Likewise, 4 grids per wavelength is well below the practical limit imposed by numerical dispersion in the fourth order method used here (Levander, 1988).

In addition to indicating a spatially homogeneous behavior, Fig. 5 shows that the method is highly successful in producing a frequency-independent $\hat{Q}(\omega)$. The dotted box encloses the usable computational bandwidth and indicates the 6% tolerance interval about a \hat{Q} of 100. For the entire computational bandwidth, \hat{Q} lies within 6% of the target value of 100. Fig. 6 shows the corresponding results for $Q_0 = 20$. In this case, the difference in definition between \hat{Q} and Q is significant, and when Q (as defined by Eqn 10) is frequency independent and equal to 20, \hat{Q} (as defined by Eqn 48) should be approximately 19, as can be verified analytically using expressions in Kjartansson (1979). As Fig. 6 indicates, this target \hat{Q} is again achieved within 6% tolerance over virtually the entire usable computational frequency band. For the 2 decades from 5 grids per wavelength to 500 grids per wavelength, the variation in \hat{Q} is less than $\pm 3\%$ in both the $Q_0 = 20$ and $Q_0 = 100$ cases.

At wavelengths shorter than 4 grid points, as predicted by the perturbation analysis, backscatter due to coarse-graining adds to the numerical errors which are already present in the form of numerical dispersion. For a low-order finite difference method (such as the fourth order method tested here), wavelengths shorter than 4 grid points are usually considered to lie outside the usable computational bandwidth, as a result of ordinary numerical dispersion alone. Whenever that is the case, the anelastic coarse-graining imposes no additional limitation on usable bandwidth. On the other hand, higher-order finite difference and pseudospectral methods may have sufficiently accuracy for some applications at wavelengths shorter than 4 grid points. When that is the case, the coarse-grain method will not be appropriate.

2.6 DISCUSSION

In the numerical example, the period-two coarse-grain method achieved a frequency-independent Q , to high accuracy, over more than 2 decades in frequency, using a single memory variable per stress component per node. This accuracy was achieved without any attempts to optimize the frequency distribution or weighting of the relaxation times in (46). In fact, we did not exploit the flexibility provided by the weight function w at all, simply setting it to 1 in the example.

The weight function can be exploited in several different ways to optimize and/or generalize the coarse-grain method. For example, if further accuracy were desired in the approximation of a frequency-independent Q , any of the optimization methods which have been proposed in the literature for generating conventional memory variable representations could be used in conjunction with period-two coarse graining (e.g., Emmerich and Korn,

1987; Carcione et al., 1988; Witte and Richards, 1990; Blanch et al. 1995). The first step in doing so would be the conventional one: choose relaxation times τ_j and quadrature weights λ_j (8 of each for 3D, 4 of each for 2D) to optimize the approximation of (11) by (15). Then those relaxation times would be identified with the discrete form of $\tau(x)$, Eqn 40; the quadrature weights, after being normalized to unit mean, would be identified with the discrete form of $w(x)$, Eqn 41.

A second application of the weight function would be to approximate some other desired frequency dependence of Q , a power law, for example. As in the case of frequency independent Q , any of the memory variable optimization techniques in the literature could be used to find the 8 relaxation times and quadrature weights, which are then identified with the coarse-grain relaxation times and (after normalization) weights.

A third application of the weight function would be to further reduce memory requirements in instances where the accuracy possible with 8 relaxation times is redundant. In some seismic exploration problems, for example, a fairly narrow-band representation of Q may be acceptable in practice. Blanch et al. (1995) have argued that 2 properly chosen relaxation times provide sufficient constant- Q bandwidth (Q constant within 8% over roughly one decade in frequency) for many practical purposes, especially given the limited problem sizes which are practical with current computers (Robertsson et al. (1994) have even found a single relaxation time to provide an adequate approximation in some narrow-band applications in high resolution reflection seismology). In cases where the two-relaxation-time approximation is acceptable, for example, we could assign these 2 values to τ_1 and τ_2 in (40), assign values to w_1 and w_2 in (41) such that $w_1 + w_2$ equals 8 (in 3D; or 4 in 2D), and set the remaining w_i to zero. This strategy would eliminate the need to store any memory variables at all at 75% of the nodes in the grid, and only 1 per node at the remaining 25%, thereby reducing the memory variable storage by a factor 8 (or a factor of 4 in 2D), relative to a conventional 2 memory-variable method. Obviously, then, with the aid of the weight function, any conventional memory variable scheme could be coarse grained to achieve an 8-fold memory reduction in 3D, or 4-fold reduction in 2D.

The above numerical example was restricted to the acoustic wave equation. There is no apparent reason, however, that the method should not work equally well for the elastodynamic case. In fact, it is for the later case that the method is likely to be most useful, because the presence of 6 stress components in 3D elastodynamics places very large memory requirements on the conventional memory variable method. Furthermore, the advantages of the coarse-grain method will become even more important as higher computing speeds become available. The speed increases will permit 3D elastodynamic simulations to be computed with ever greater usable bandwidth, and, as computational bandwidth increases, memory variables constitute a progressively larger proportion of the total computational memory requirement.

We have established the viability of the coarse-grain method for the fourth-order staggered grid finite difference method, and it should work equally well with other low-

order finite difference or finite element methods. It has yet to be established, however, whether the coarse-grain method will work effectively with higher-order finite difference methods or with pseudospectral methods. The main issue is likely to be whether coarse-graining entails any loss of usable bandwidth when applied with those numerical methods. The staggered-grid pseudospectral methods, in particular, may be questionable candidates for the coarse-grain method. In pseudospectral methods, the spatial differentiation operators are exact if the medium is homogeneous (and the wavefield spatially periodic and sufficiently band-limited). In that case, the only source of numerical dispersion arises from approximations associated with the time integration. In the case of the staggered grid pseudospectral methods, numerical dispersion can be kept very small even at the spatial Nyquist wavenumber, i.e., down to only 2 nodes per wavelength. On the other hand, when discrete interfaces or sharp transitions in wavespeed are present in the model, 3 to 4 nodes per wavelength are required in order to accurately model the reflection and transmission behavior (Witte and Richards, 1990). In cases where the practical limit of the pseudospectral method is determined to be 4 nodes per wavelength or greater, the coarse-grain method should be effective, though this conjecture will have to be tested numerically. If so, the method will provide the same degree of memory savings that it provides in the case of low-order finite difference methods.

2.7 SUMMARY

We have developed a new method for introducing anelastic attenuation into time-stepped numerical methods for solving the equations of acoustics and elastodynamics. The method is designed to reduce drastically the memory requirements of anelastic modeling. It takes as its starting point an N -pole (i.e., N -relaxation time) approximation to the relaxation spectrum. Then, the N corresponding memory variables are distributed over the stress node-points of the computational grid, one per stress component per unit cell. An analysis via perturbation theory shows that this single memory-variable method will reproduce the attenuative behavior of the N memory-variable model provided i) the weights assigned each of the N relaxations (corresponding to the residues in the N -pole representation) are rescaled to have unit volumetric mean, and provided the relaxation times are distributed in a periodic array, with period less than half the minimum wavelength to be modeled. We make N equal to 8 for 3D problems and 4 for 2D problems, and distribute the memory variables so that, for each stress component, the relaxation time array has a spatial period, in each direction, equal to twice the unit-cell dimension. This period-two coarse-grain method is accurate for wavelengths exceeding 4 unit-cell dimensions.

Accuracy of the method has been verified in numerical examples for the 3D acoustic wave equation. The test problems were solved using a fourth order staggered grid finite difference method. In the numerical examples, a frequency-independent Q was achieved within a 3% tolerance over the 2 decades in frequency from 5 grids per wavelength to 500 grids per wavelength, using only a single memory variable per stress

component per node. Straightforward generalizations of the method can be used to approximate specific frequency-dependent Q models such as power laws, or to further reduce memory requirements.

We expect the method to work equally well for low-order finite difference or finite-element solutions in elastodynamics. For higher-order finite difference methods, as well as for pseudospectral methods, the utility of the coarse-graining method will depend upon the limiting wavelength at which the underlying numerical method has acceptable accuracy. In those numerical methods in which the usable bandwidth is restricted to wavelengths longer than 4 unit-cell dimensions, the coarse-grain method should be accurate and efficient.

In those cases where it is appropriate, the method reduces storage requirements for memory variables by a factor of 8 for 3D problems and by a factor of 4 for 2D problems. As computer speeds increase, larger problems, and therefore higher computational bandwidths, will become feasible. As computational bandwidth increases, memory variables will account for an increasing proportion of total storage requirements, putting a further premium on the concision achieved by the coarse-grain method.

2.8 REFERENCES

- Aki, K., and P. G. Richards (1980). *Quantitative Seismology, Theory and Methods*, W. H. Freeman and Co., New York.
- Blanch, J.O., J.O.A. Robertsson, and W.W. Symes (1995). Modeling of a constant Q: Methodology and algorithm for an efficient and optimally inexpensive viscoelastic technique, *Geophysics* 60, 176-184.
- Carcione, J.M., D. Kosloff, and R. Kosloff, (1988). Wave propagation in a linear viscoacoustic medium, *Geophysical J. Roy. Astr. Soc.* 93, 393-407.
- Carcione, J.M., D. Kosloff, A. Behle, and G. Seriani (1992). A spectral scheme for wave propagation simulation in 3-D elastic-anisotropic media, *Geophysics* 57, 1593-1607.
- Day, S.M., and J.B. Minster (1984). Numerical simulation of attenuated wavefields using a Padé approximant method, *Geophysical J. Roy. Astr. Soc.* 78, 105-118.
- Emmerich, H., and Korn, M. (1987). Incorporation of attenuation into time-domain computations of seismic wavefields, *Geophysics* 52, 1252-1264.
- Frankel, A., and J. Vidale (1992). A three-dimensional simulation of seismic waves in the Santa Clara Valley, California, from a Loma Prieta aftershock, *Bull. Seism. Soc. Am.* 82, 2045-2074.
- Frankel, A. (1993). Three-dimensional simulations of ground motions in the San Bernardino Valley, California, for hypothetical earthquakes on the San Andreas fault, *Bull. Seism. Soc. Am.* 83, 1020-1041.
- Graves, R. W. (1993). Modeling three-dimensional site response effects in the Marina District basin, San Francisco, California, *Bull. Seism. Soc. Am.* 85, 1042-1063.
- Graves, R.W. (1996). Simulating seismic wave propagation in 3D elastic media using staggered-grid finite differences, *Bull. Seism. Soc. Am.* 86, 1091-1106.
- Igel, H., and M. Weber (1995). SH-wave propagation in the whole mantle using high-order finite differences, *Geophys. Res. Lett.* 22, 731-734.
- Kjartansson, E. (1979). Constant Q wave propagation and attenuation, *J. Geophys. Res.* 84, 4737-4748.

- Krebs, E.S., and G.Quiroga-Goode (1994). A standard finite-difference scheme for the time-domain computation of anelastic wavefields, *Geophysics* 59, 290-296.
- Levander, A.R. (1988). Fourth-order finite-difference P-SV seismograms, *Geophysics* 53, 1425-1436.
- Minster, J.B. (1980). Anelasticity and attenuation, in *Physics of the Earth's Interior, Proc. Enrico Fermi Int. School Phys.*, eds. A.M. Dziewonski, and E. Boschi, North-Holland, Amsterdam.
- O'Connell, R.J., and B. Budiansky (1978). Measures of dissipation in viscoelastic media, *Geophys. Res. Lett.* 5, 5-8.
- Olsen, K.B., J.C. Pechmann, and G.T. Schuster (1995a). Simulation of 3D elastic wave propagation in the Salt Lake Basin, *Bull. Seism. Soc. Am.* 85, 1688-1710.
- Olsen, K.B., R.J. Archuleta, and J.R. Matarese (1995b). Three-dimensional simulation of a magnitude 7.75 earthquake on the San Andreas fault, *Science* 270, 1628-1632.
- Robertsson, J.O.A., J.O. Blanch, and W.W. Symes (1994). Viscoelastic finite-difference modeling, *Geophysics* 59, 1444-1456.
- Witte, D.C., and P.G. Richards (1990). The pseudospectral method for simulating wave propagation, in Lee, D., Cakmak, R., and Vichnevetsky, Eds., *Computational acoustics, seismo-ocean acoustics and modeling*, North-Holland, 1-18.
- Yomogida, K., and J.T. Eigen (1993). 3D wave propagation in the Los Angeles Basin for the Whittier-Narrows earthquake, *Bull. Seism. Soc. Am.* 83, 1325-1344.
- Yoon, K-H., and G.A. McMechan (1995). Simulation of long-period 3-D elastic responses for whole earth models, *Geophys J. Int.* 120, 721-730.

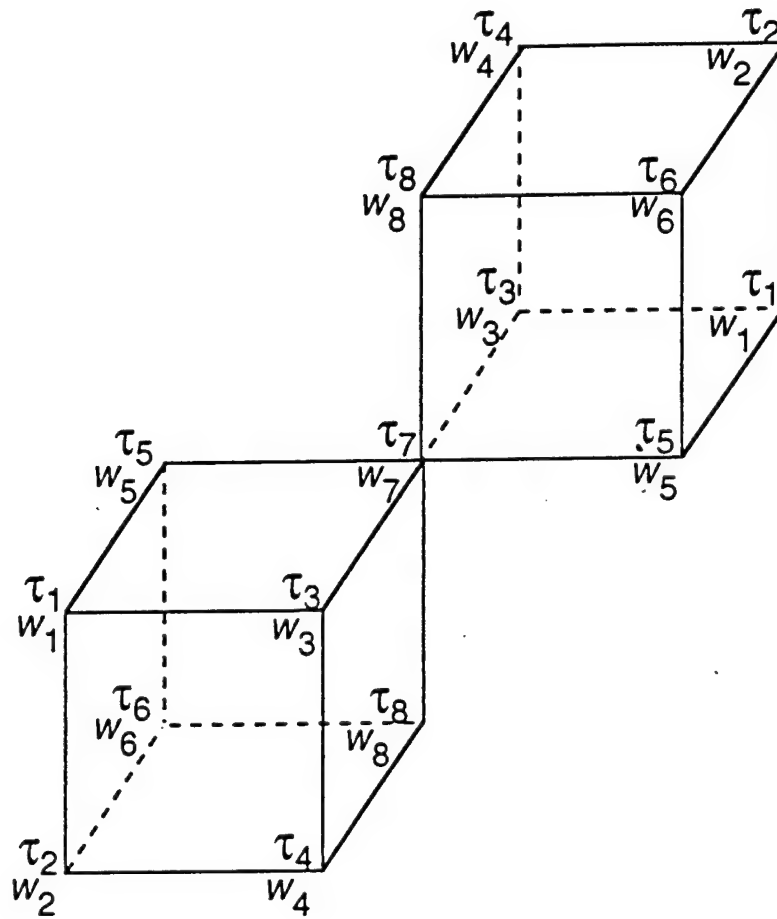


Figure 1. Distribution of relaxation times τ_i and weights w_i in the period-two coarse-grain scheme. Vertices represent computational node points for a given stress component

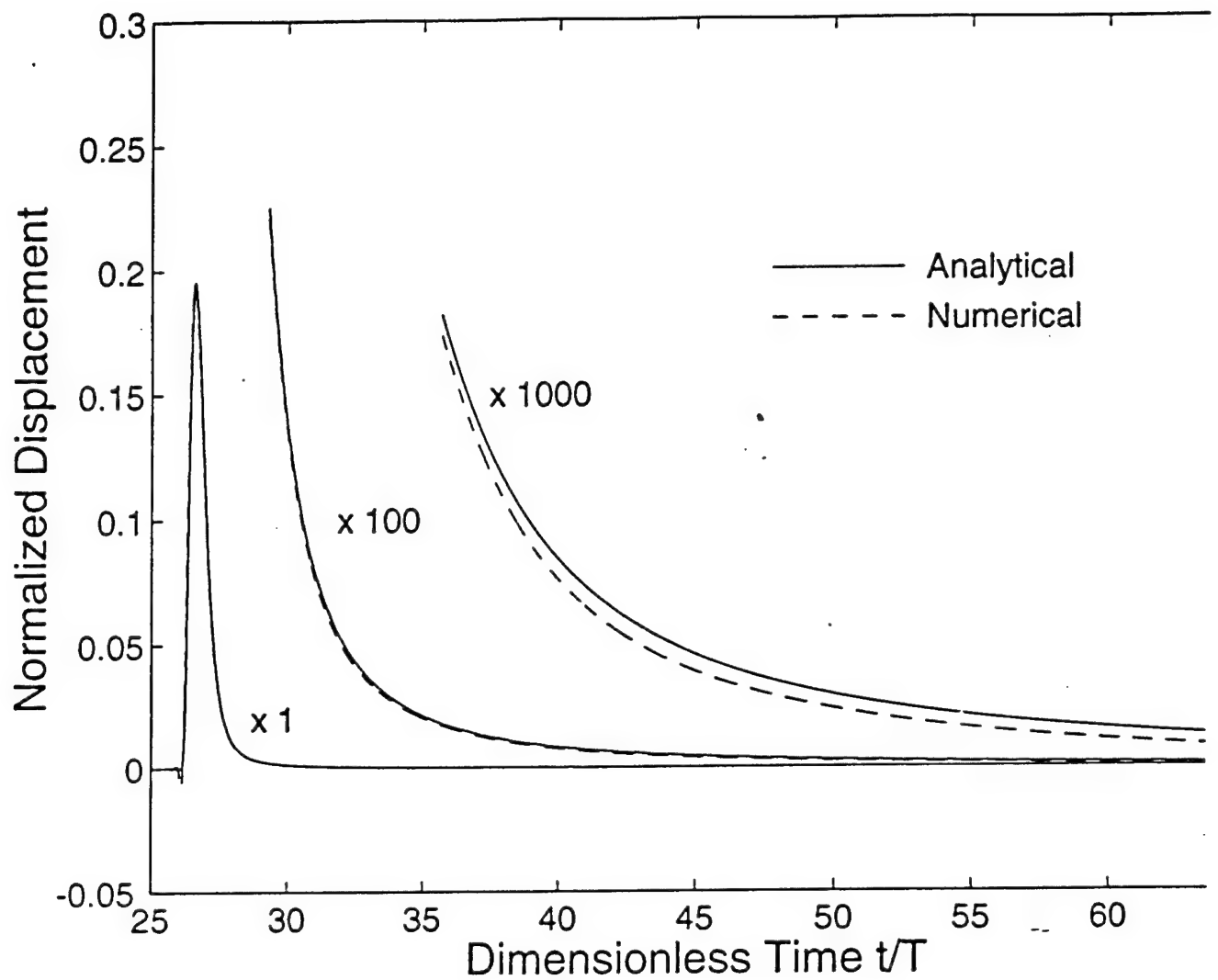


Figure 2 (a). Broadband pulse, for the case of Q_0 equal to 100, after propagating a distance of 26 times its corner wavelength. The entire pulse is shown, with low-amplitude portions magnified by factors of 100 and 1000. Time has been scaled by the source corner frequency $1/T$.

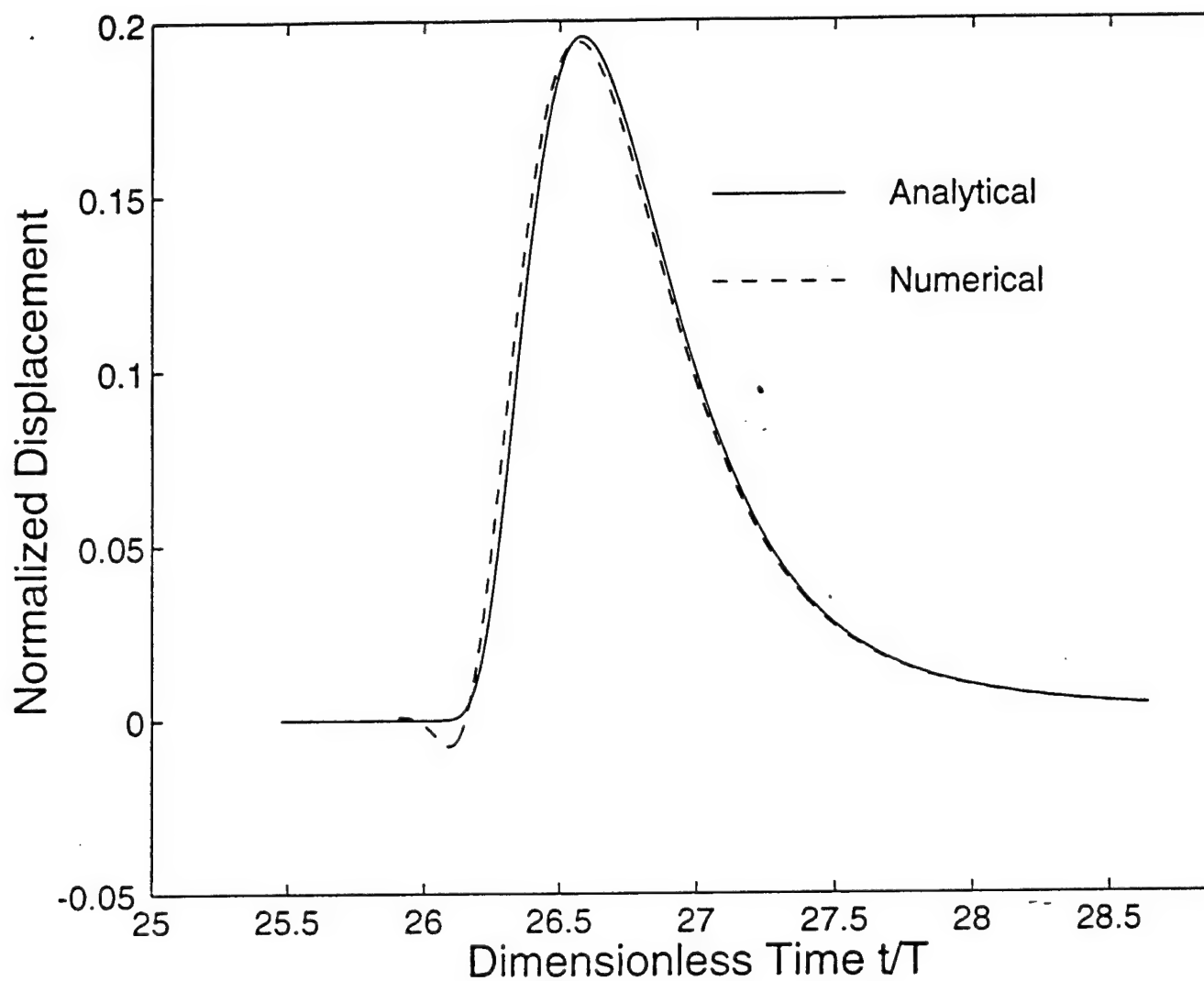


Figure 2 (b). Broadband pulse, for the case of Q_0 equal to 100, after propagating a distance of 26 times its corner wavelength. The initial portion is shown on an expanded time scale. Time has been scaled by the source corner frequency $1/T$.

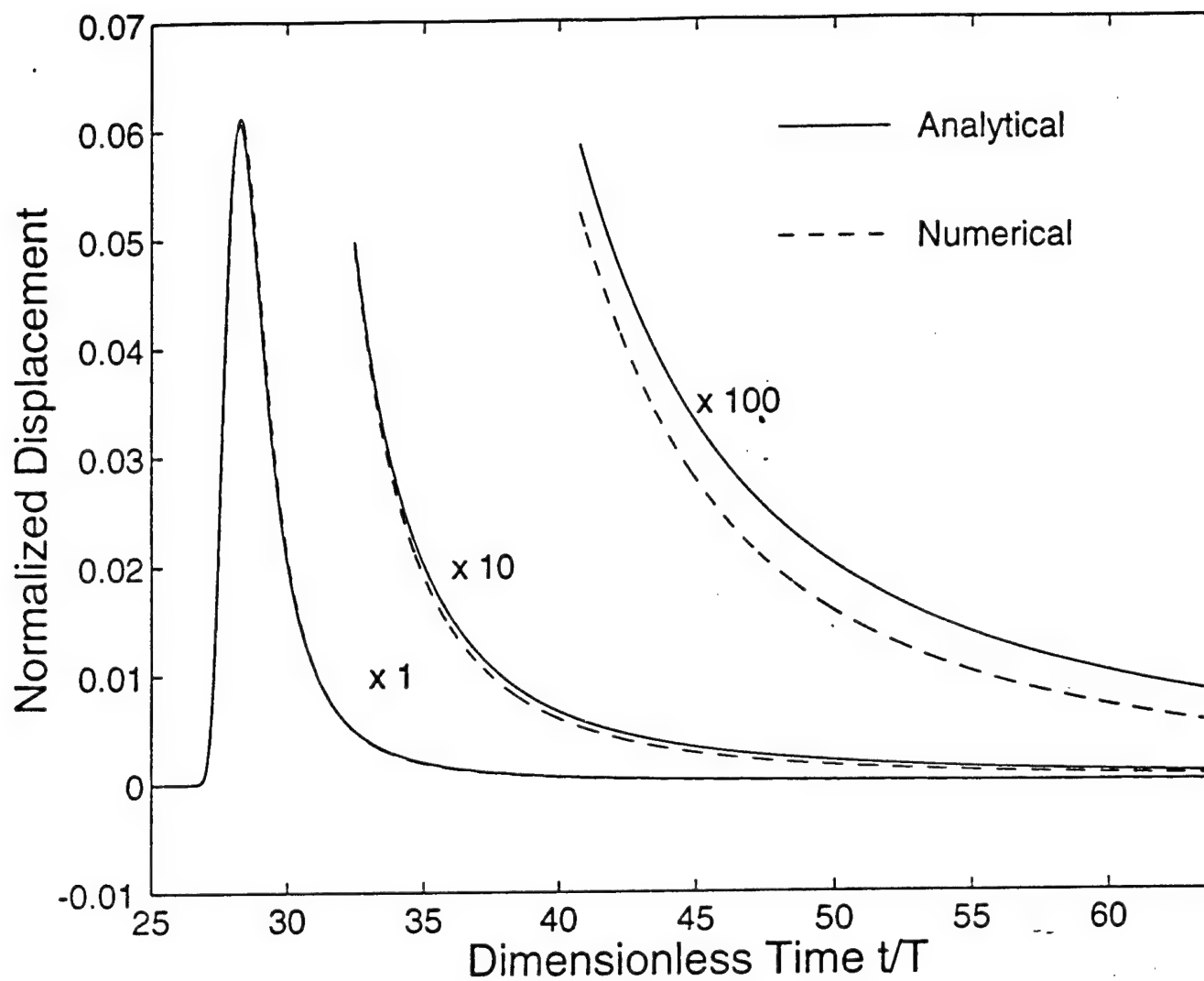


Figure 3 (a). Broadband pulse, for the case of Q_0 equal to 20, after propagating a distance of 26 times its corner wavelength. The entire pulse is shown, with low-amplitude portions magnified by factors of 10 and 100.

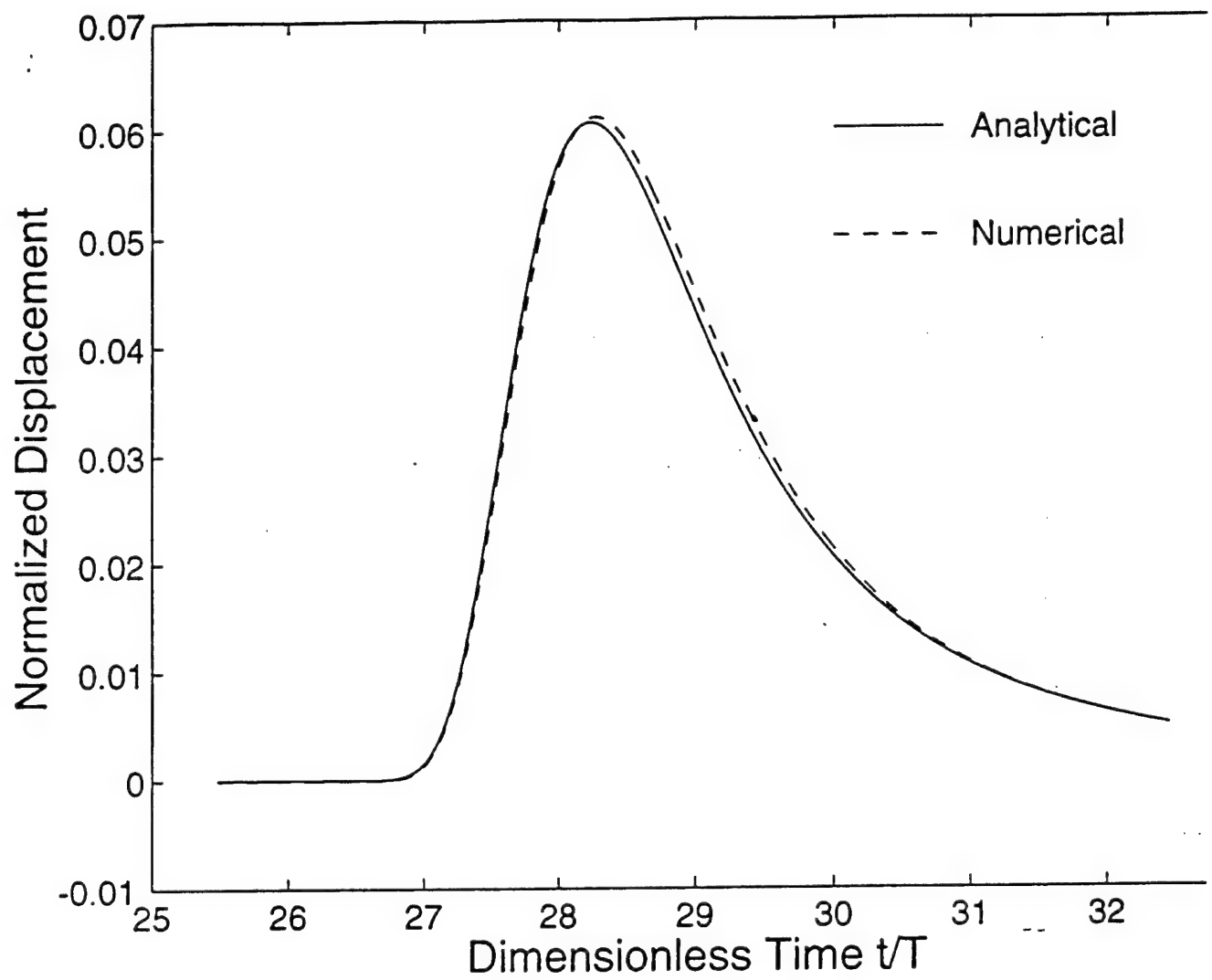


Figure 3 (b). Broadband pulse, for the case of Q_0 equal to 20, after propagating a distance of 26 times its corner wavelength. The initial portion is shown on an expanded time scale.

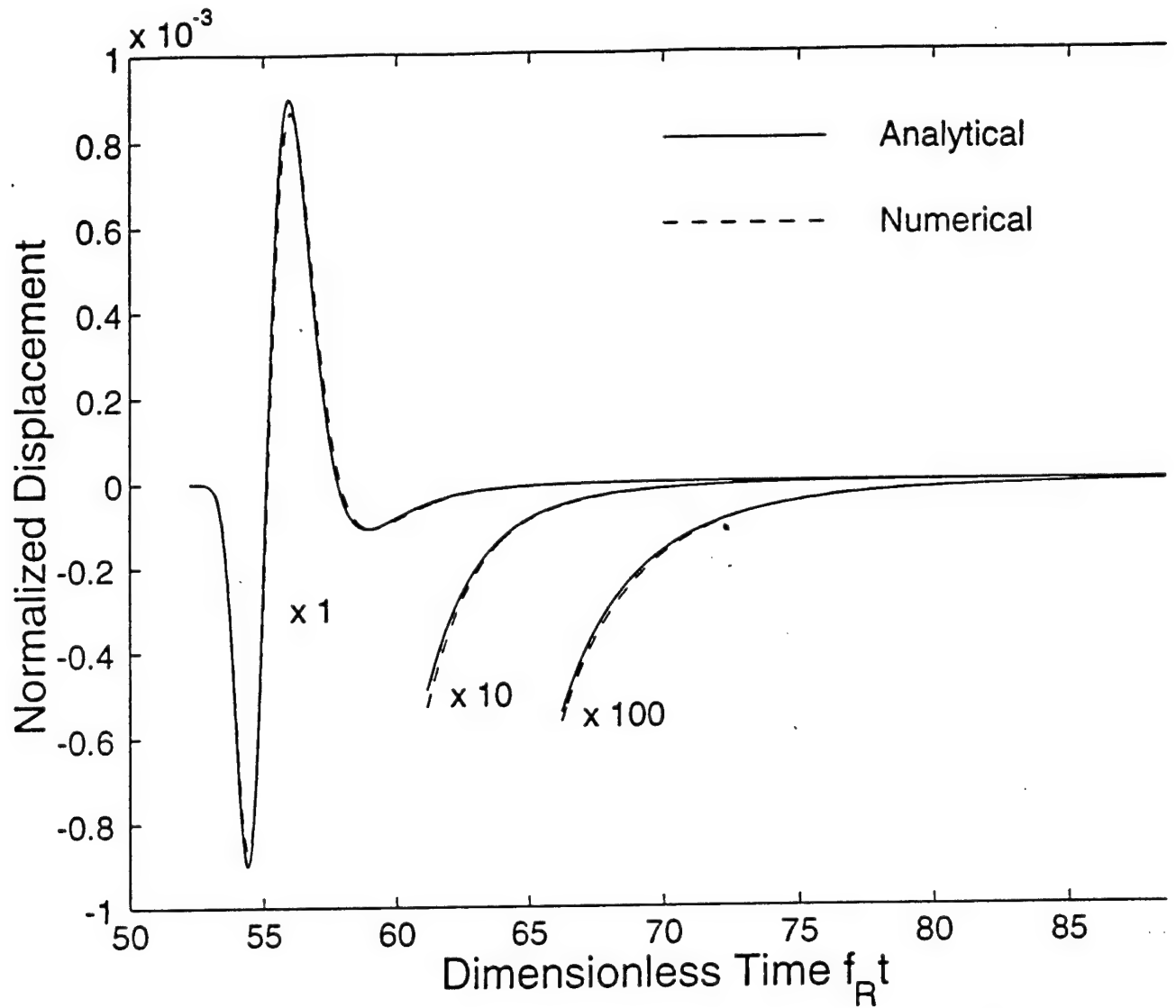


Figure 4 (a). Narrow-band pulse, for the case of Q_0 equal to 20, after it has propagated a distance of 52 times its dominant frequency. The pulse was constructed by convolving the broadband pulse with a Ricker wavelet. The latter has a dominant frequency f_R equal to twice the corner frequency of the initial broadband pulse. The entire pulse is shown, with low-amplitude portions magnified by factors of 10 and 100.

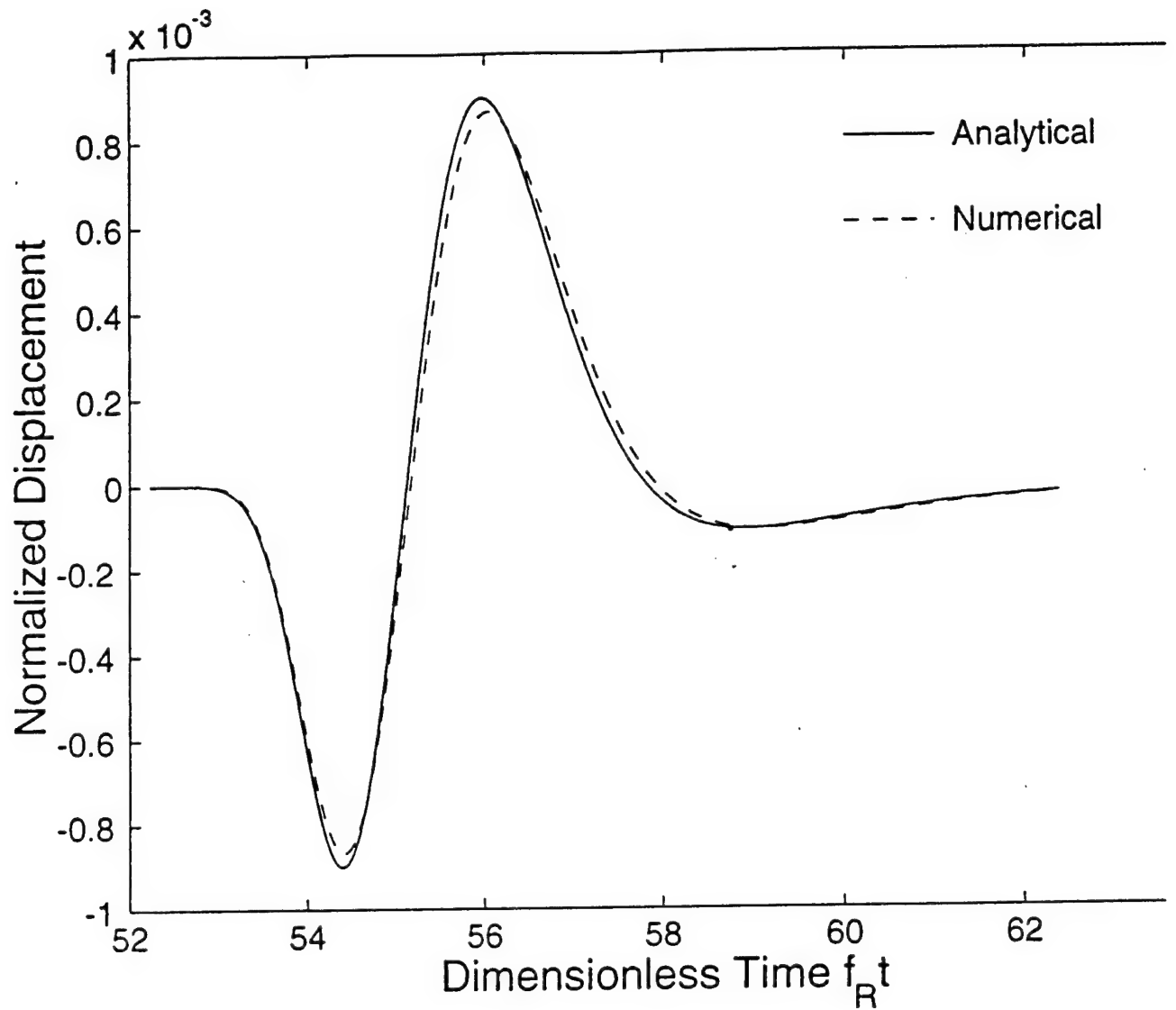


Figure 4 (b). Narrow-band pulse, for the case of Q_0 equal to 20, after it has propagated a distance of 52 times its dominant frequency. The pulse was constructed by convolving the broadband pulse with a Ricker wavelet. The latter has a dominant frequency f_R equal to twice the corner frequency of the initial broadband pulse. The initial portion is shown on an expanded time scale.

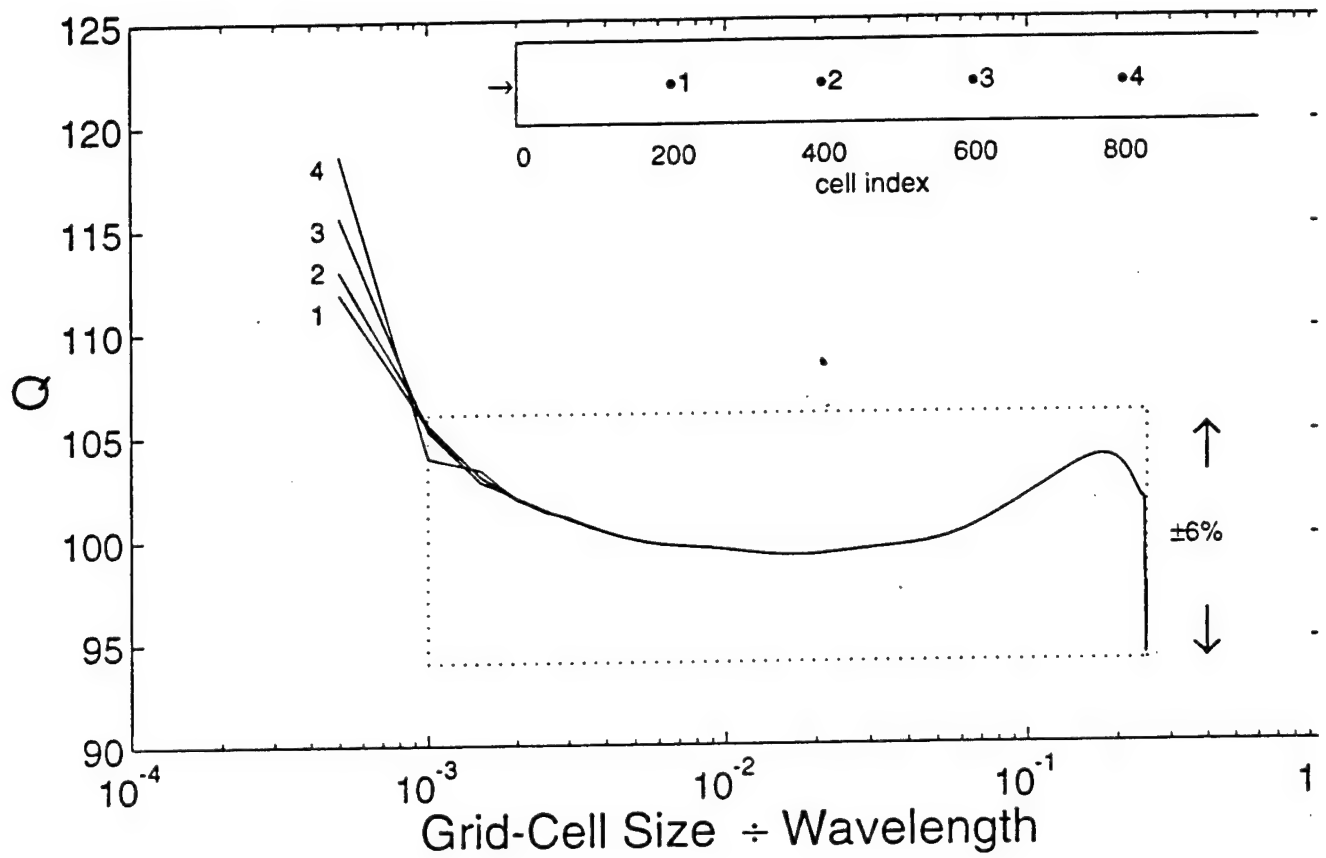


Figure 5. $\hat{Q}(\omega)$ for the numerical solution in the case Q_0 equal to 100. Four estimates are shown, corresponding to spectral ratios at successive 200 grid-cell intervals. The dotted box delimits the usable computational bandwidth and the 6% tolerance interval about a \hat{Q} of 100.

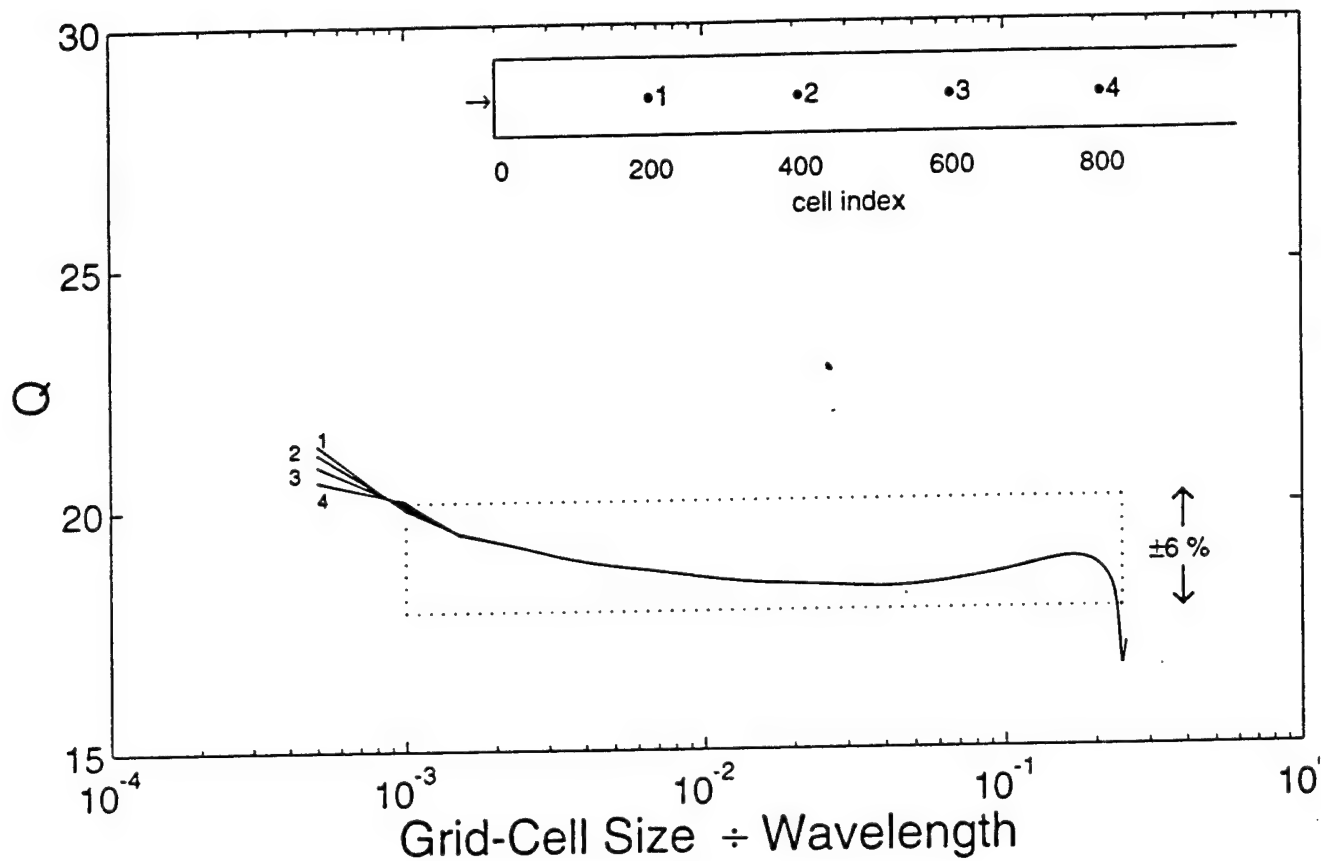


Figure 6. $\hat{Q}(\omega)$ for the numerical solution in the case Q_0 equal to 20. Four estimates are shown, corresponding to spectral ratios at successive 200 grid-cell intervals. The dotted box delimits the usable computational bandwidth and the 6% tolerance interval about a \hat{Q} of 19 (which corresponds to a Q of 20).

3 MODEL FOR NONLINEAR WAVE PROPAGATION DERIVED FROM ROCK HYSTERESIS MEASUREMENTS

Heming Xu, Steven M. Day, and Jean-Bernard H. Minster

3.1 ABSTRACT

We develop a method for modeling nonlinear wave propagation in rock at intermediate strain levels, i.e., strain levels great enough that nonlinearity cannot be neglected, but low enough that the rock does not incur macroscopic damage. The constitutive model is formulated using a singular-kernel endochronic formalism, and this formulation is shown to satisfy a number of general observational constraints, including producing a power law dependence of attenuation (Q^{-1}) on strain amplitude. Once the elastic modulus is determined, and a second parameter fixed to give Q^{-1} linear in the strain amplitude, the model has 2 remaining free parameters. One of these represents cubic anharmonicity, and we set it to agree with laboratory observations of harmonic distortion. The other parameter controls the amount of hysteresis, and it is set to approximate stress-strain curves measured in laboratory uniaxial stress experiments on Berea sandstone by Boitnott and Haupt. The constitutive equations, though fundamentally nonlinear and rate-independent, have a superficial, formal resemblance to viscoelasticity, which we exploit to produce an efficient, stable numerical algorithm. We solve 1D wave propagation problems for this constitutive model using both finite difference and pseudospectral methods. These methods are shown to reproduce, to high precision, analytical results for quasi-harmonic wave propagation in a nonlinearly elastic medium.

Application of the Berea sandstone model to quasi-harmonic wave propagation shows several departures from results obtained with nonlinear elasticity. The Berea model shows more rapid decay with distance of the fundamental frequency component, due to nonlinear, amplitude-dependent attenuation, than does nonlinear elasticity. The Berea model also shows enhanced excitation of the order 3 harmonic, in agreement with laboratory observations. In addition, the growth with propagation distance of the harmonics of the source excitation shows a saturation, relative to the nonlinear elasticity results. This behavior reflects the competing effects of amplitude growth via energy transfer from the source frequency, and energy dissipation due to hysteresis, the dissipation increasing as the harmonic amplitude grows. In additional numerical experiments, we find that a two-frequency source function generates harmonics with frequencies which can be expressed as linear combinations of integer multiples of the two source frequencies, in agreement with published laboratory results for other solids.

3.2 INTRODUCTION

There is now a rather large body of experimental data demonstrating that rocks behave nonlinearly when deformed to strain levels exceeding about 10^{-6} . An intermediate strain regime is conveniently defined as that strain range over which rocks respond nonlinearly to loading, but do not exhibit macroscopic damage. This strain range can be taken to be, very roughly, 10^{-6} - 10^{-3} .

Rocks display much more complex nonlinear behavior than most other solids since they have quite disordered compositions and structures. Because of the presence of genetic structural defects such as microcracks, dislocations and grain boundaries, inelasticity manifests itself as variations of the measured effective modulus and wave velocity with applied stress and as strain dependent attenuation. The nonlinear stress-strain relationship may lead to progressive distortion of seismic waveforms and energy transfer among different frequency bands during propagation from source to recording site, in contrast to the behavior of a linear system.

Unfortunately, few purely analytical methods are available for modeling nonlinear seismic wave propagation quantitatively. The extensive array of both exact and asymptotic methods available for linear wave propagation are not valid in the intermediate strain regime. A comprehensive understanding of stress wave propagation in this strain range requires a computational model incorporating nonlinearity.

The computational study of wave propagation in rocks in the intermediate strain regime contributes to several different areas of applied and fundamental research in seismology and acoustics. For example, strains surrounding seismic sources such as earthquakes and underground explosions reach intermediate-strain levels over volumes much larger than the volume in which failure occurs, and a better understanding of wave propagation in this volume is likely to improve our understanding of seismic source physics. Understanding wave propagation at intermediate strains may also contribute to the development of non-destructive seismic methods for inferring the internal defect structure of rock and soil masses (e.g., by relating nonlinear characteristics of the response, such as harmonic distortions, to states of internal deformation and fatigue of the rock mass).

In this paper we develop a numerical model suitable for seismic wave propagation in rocks at intermediate strain levels. To do so, we couple the linearized momentum conservation equation to a so-called "endochronic" constitutive model (Valanis and Read, 1982; Valanis and Fang, 1983; Valanis and Lee, 1984), which gives the stress as a rate-independent functional of the strain history. This constitutive functional lead to an elastic-plastic stress-strain relationship, but without a yield surface, having free parameters which are easily fit to match quasistatic, laboratory data. The framework of the model is such that it automatically preserves several widely observed generic characteristics of intermediate-strain rock response, including cusped hysteresis loops and power-law dependence of attenuation on strain amplitude. The stress-strain behavior of the model has been fit to intermediate-strain laboratory data on rock hysteresis in Berea sandstone provided by G.

Boitnott and R. Haupt of New England Research, Inc. (Boitnott, 1992; 1993). The model automatically reduces to linear elasticity at low strain. The constitutive functional is recast into a form well adapted to large computations, in that the model state is specified by a small set of memory variables which can be time-stepped by a simple, stable finite difference method. The momentum equation is also time stepped by finite differencing, with the spatial derivatives approximated by a Fourier pseudospectral method.

We begin with overviews of the general assumptions upon which the endochronic formalism rests and some generic observational constraints on constitutive models for rock. Then we outline the specifics of the endochronic model, demonstrate that the formalism is consistent with the generic observational constraints, and show the model fit to Berea sandstone data. We then describe its numerical implementation for wave propagation applications and show that this method is capable of giving accurate solutions to transient wave propagation problems. Finally we show that the model predicts harmonic distortions during wave propagation which are comparable to those observed in laboratory wave propagation experiments.

3.3 BACKGROUND

Constitutive Functionals

We fit laboratory data and simulate wave propagation using an elastic-plastic constitutive model of the so-called endochronic type. We begin this section with a brief overview of constitutive models, in order to indicate the general assumptions which underlie the endochronic formalism.

We restrict consideration to so-called simple materials, i.e., materials for which the stress-strain relationship is local, in the sense that stress at material point \mathbf{X} is a functional of the deformation gradient only (and not, for example, dependent on higher spatial derivatives of the displacements). Assuming the principle of frame indifference applies, the second Piola-Kirchhof stress tensor at time t , $\pi(t)$, is then a functional of the (Lagrangian) strain tensor time history, $\mathbf{E}(t)$:

$$\pi(\mathbf{X}, t) = \tilde{F}[\mathbf{E}(\mathbf{X}, t'), -\infty \leq t' \leq t]. \quad (1)$$

When the displacement gradients are small, we can use the Cauchy stress tensor \mathbf{S} in place of π and the infinitesimal strain tensor ϵ in place of \mathbf{E} ,

$$\mathbf{S}(\mathbf{X}, t) = \tilde{F}[\epsilon(\mathbf{X}, t'), -\infty \leq t' \leq t]. \quad (2)$$

This approximate formulation still permits nonlinearity of the constitutive functional, but neglects geometrical nonlinearities. For most applications to earthquake and explosion

ground motion, this approximation is adequate, and we adhere to it in the current study. Important exceptions would be motions very near the source, as well as ground-motion-induced soil liquefaction, both of which are beyond our scope.

If memory effects are suppressed in (1) or (2), so that stress is simply a function of the strain, we have the special case of nonlinear elasticity. In this case, there is no hysteresis, and wave propagation entails no loss of energy, but there will in general be transfer of energy among frequency components of the wavefield.

If memory effects are retained, but the functional in (2) is time shift invariant and linear, we have the special case of linear viscoelasticity, (2) reducing to a convolution

$$S(t) = M(t) * \frac{d\epsilon(t)}{dt}. \quad (3)$$

where M is the (fourth-order tensor valued) time-dependent modulus. The material will exhibit hysteresis, with elliptical loops under monochromatic loading. Superposition applies, and there is no energy transfer among frequency components. If memory effects are also suppressed in (3), we have linear elasticity.

We can rewrite the general functional (1) in the form

$$\pi(\mathbf{X}, t) = F[\mathbf{E}(\mathbf{X}, \xi'); \dot{\xi}(\mathbf{X}, \xi'); -\infty \leq \xi' \leq \xi(\mathbf{X}, t)] \quad (4)$$

where ξ is the strain path length, the increment of which is given, in terms of positive definite tensor \mathbf{g} , by

$$d\xi = d\mathbf{E} : \mathbf{g} : d\mathbf{E}. \quad (5)$$

If the stress is a functional of strain, expressed as a function of ξ , but has no explicit dependence on the strain rate $\dot{\xi}$, the rheology is said to be rate-independent, and (4) reduces to

$$\pi(\mathbf{X}, t) = F[\mathbf{E}(\mathbf{X}, \xi'); -\infty \leq \xi' \leq \xi(\mathbf{X}, t)]. \quad (6)$$

In this case, the wavefield (in a homogeneous medium) obeys a simple, well-known scaling relationship: if $\mathbf{u}_1(\mathbf{X}, t)$ is a displacement field obeying the equations of motion, then a positive parameter λ generates a family of solutions $\mathbf{u}_\lambda(\mathbf{X}, t)$ given by

$$\mathbf{u}_\lambda(\mathbf{X}, t) = \lambda \mathbf{u}_1(\lambda^{-1}\mathbf{X}, \lambda^{-1}t). \quad (7)$$

The scaling relationship remains valid whether or not geometrical nonlinearities are significant. Linear and nonlinear elasticity and classical plasticity are examples of rate-independent rheologies, but linear viscoelasticity is not (apart from the special case of linear elasticity). Rate-independent materials may exhibit hysteresis, and the wavefield will lose energy during wave propagation. In contrast to the viscoelastic case, however, the hysteresis loops are, in general, not elliptical.

Here we adopt the so-called endochronic plasticity formalism of Valanis and Read (1982), which employs a special case of the rate-independent functional (6). This formalism partitions strain increments into elastic and inelastic ("plastic") components, such that

$$d\pi = \mathbf{G}(d\mathbf{E} - d\mathbf{E}^p), \quad (8)$$

where \mathbf{G} is an elastic tensor and $d\mathbf{E}^p$ denotes the plastic strain increment. A constitutive functional is constructed in which the strain in (6) is parameterized in terms of some plastic strain path length z

$$\pi(\mathbf{X}, t) = F[\mathbf{E}(\mathbf{X}, z(\xi')); 0 \leq \xi' \leq \xi(\mathbf{X}, t)]. \quad (9)$$

The functional (9) is then written in the form of an integral of a shift-invariant (in z) kernel over the plastic strain path. The theory thus has some formal resemblance to viscoelasticity, but with the role of time as the integration variable in the constitutive functional replaced by z (as a result of this formal similarity, z is sometimes referred to as an "intrinsic time," which is responsible for the designation "endochronic"). The formalism is inherently rate-independent, the constitutive functional having no explicit dependence upon the deformation rate.

We next outline some general observational constraints that apply to constitutive models for rock at intermediate strain, then present a suitable one-dimensional, small-strain implementation of (8-9). The resulting constitutive model can be shown to have a number of features consistent with the observational constraints outlined below, though it is by no means unique in that respect. We can also exploit the superficial resemblance to viscoelasticity to obtain a concise, efficient, and stable numerical formulation, rendering the model very suitable for wave propagation simulations.

Observations of Nonlinear Attenuation

At low strain levels, less than about 10^{-6} , viscoelasticity has been found to provide an adequate framework for interpreting energy losses in seismic wave propagation, including the frequency dependence of those losses (e.g., Minster, 1980). At intermediate strain levels, however, the situation is different. In this strain regime, the inadequacy of

linear viscoelasticity can be seen in both amplitude dependence and frequency scaling of the energy loss mechanism. While the deformation is not sufficient to cause macroscopic failure, it is large enough that preexisting microcracks may propagate, new ones may be created under stress, and even microplasticity may be induced (Mashinsky, 1994). Because the rheology depends on amplitude, wave propagation is characterized by nonlinearity and reflects the influence of inelastic mechanisms. In the intermediate strain regime, these mechanisms dominate and control the rate and mode of energy dissipation, but in the low strain regime, their effects are masked by linear, amplitude-independent viscoelastic mechanisms. Since high to intermediate-level strains occur near seismic sources, the proper representation of nonlinear constitutive equations for rocks in this regime is a potentially important ingredient of quantitative source models.

Seismic wave attenuation at intermediate strain levels has been observed to be amplitude dependent on the basis of both laboratory and field experiments. Apparent Q^{-1} , as estimated from resonance bar and pulse transmission experiments in the laboratory, has been found to be approximately proportional to strain amplitude for strains exceeding about 10^{-6} (e.g., Winkler et al., 1979; Mavko, 1979; Johnston and Toksoz, 1980; Stewart et al., 1983; Bonner and Wanamaker, 1990). From analysis of seismic data from field experiments with explosive sources, Minster and Day (1986) concluded that propagation losses in salt are amplitude dependent at intermediate strain levels, and that the apparent Q^{-1} is compatible with the linear dependence of apparent Q^{-1} on strain amplitude commonly observed in laboratory experiments.

When propagation losses in the intermediate strain range are analyzed in the context of linear viscoelasticity, nonlinearity can induce an apparent frequency dependence of Q . For example, Wortman and McCartor (1987) estimated $Q(f)$ from spectral ratios of ground motion recordings (maximum strain $\sim 4 \times 10^{-4}$) from the Salmon explosion (5.3 kt) in salt. They found $Q(f)$ decreasing sharply with decreasing frequency below the 6 Hz corner frequency of the explosion. They performed the same analysis for one of the much smaller Cowboy explosions (corner frequency ~ 100 Hz), also in salt, with recordings at the same scaled range and similar maximum strain level. In the latter case, Wortman and McCartor found an absorption band of very similar shape, but shifted up in frequency in proportion to the corner frequency ratio of the sources. This result is incompatible with the assumption of linear viscoelasticity. However, the shift in the apparent absorption band is precisely the scaling that would be predicted for a nonlinear, rate-independent rheology (i.e., Eqn 7).

Observations of Harmonic Distortion

The amplitude dependence of attenuation at intermediate strains is most likely associated with friction along microcracks and joints (Boitnott, 1992; 1993). Considerable experimental and theoretical interest is developing in this and other nonlinear effects

associated with the propagation of sound waves in nonlinear solids. Continuous acoustic wave phase detections of wave propagation in solids, including rocks, have found that when a sinusoidal ultrasonic wave of a given frequency and of sufficient amplitude is introduced, the fundamental wave distorts as it propagates and the higher harmonics of the fundamental frequency are generated (Breazeale and Ford, 1965; Hirata et al., 1965; Thompson et al., 1976; Thompson and Tiersten, 1977; Meegan et al., 1993). In summary, ultrasonic experiments have identified these characteristics of wave propagation and interaction: 1) harmonics of all orders are generated for a single frequency sinusoidal source; 2) the fundamental component decays away from source and the second harmonic amplitude increases linearly with the propagation distance and quadratically with both source amplitude and the source frequency (e.g., Meegan et al., 1993 for Berea sandstone samples). 3) two-frequency sound beams are found to interact in nonlinear solids so as to produce frequencies of combinations (sums and differences of integer multiples) of the two driving frequencies (Bonner and Wanamaker, 1990, 1991; Johnson et al., 1987, 1991; Johnson and Shankland, 1989). Since energy transfer between frequency bands can not occur in a linear system, such observations are clearly diagnostic of nonlinear rheology at intermediate strain levels. The potential use of these nonlinear effects as a means of exploring the early stages of the plastic deformation and mechanism of dislocation damping has been demonstrated in the experiments of Hirata et al. (1965) and Morris et al. (1979).

The harmonic distortions during wave propagation may result from at least two causes. The lattice itself can be anharmonic, or dislocations within the solid can produce such nonlinear effects (Breazeale and Ford, 1965). The formalism of nonlinear elasticity has been applied to describe the consequences of lattice anharmonicity (Breazeale and Ford, 1965), which implies material imperfection on the atomic scale. Nonlinear effects due to dislocation displacements have been considered as well (Hirata et al., 1965). Nonlinear interactions of frequency components in large-amplitude elastic waves in rocks were analyzed with perturbation expansions and Green function techniques in terms of nonlinear elasticity (McCall, 1994; Thompson and Tiersten, 1977). For a monochromatic longitudinal plane wave, for example, the excitation of higher harmonics can be shown to scale with a dimensionless coefficient β , which represents the cubic anharmonicity, and is defined in terms of the second and third order elastic moduli. For example, when the amplitudes of higher harmonics measured in wave propagation experiments in Berea sandstone were interpreted in the context of nonlinear elasticity theory, the coefficient β was estimated to be about 7×10^3 (Meegan et al. 1993). Other models have incorporated asymmetries between loading and unloading moduli to represent solids with microplasticity; for example, Nazarov et al. (1988) propose such a model to account for the experimental results on harmonics generation by standing waves on a copper rod.

Observations of Stress-Strain Curves

Laboratory stress-strain curves under cyclic loading characteristically demonstrate the following features which a successful model must emulate: 1) Hysteresis occurs, implying energy loss, and the effective Q characterizing the dissipation is strain-amplitude dependent. 2) Hysteresis loops are cusped at reversal points, rather than elliptical (as would typify linear anelastic behavior); 3) No yield surface is evident in the loading curves, at least for strains up to 10^{-4} . 4) Upon reversal of strain path, the tangent modulus is roughly equal to the instantaneous elastic modulus (Gordon and Davis, 1968; Liu and Peselnick, 1979; McKavanagh and Stacey, 1974; Minster et al., 1991). These hysteresis loops indicate that weak microplasticity is created during the cyclic loading processes at the intermediate strain levels. Attempts to simulate this kind of hysteretic behavior using linear anelasticity as the point of departure fail to replicate one or more of the foregoing features (Minster et al., 1991; Day et al., 1992). The observed behavior can be represented in terms of an ensemble of many simple hysteretic units (McCall and Guyer, 1994; Guyer et al., 1995; 1997), and the properties of the ensemble may provide insight into the micromechanics underlying the hysteresis, but such representations do not of themselves provide a formulation suitable for large numerical simulations of wave propagation.

3.4 IMPLEMENTATION OF THE ENDOCHRONIC MODEL

Singular-Kernel Formulation

We assume, following Valanis and Read (1982), that (9) can provide an adequate phenomenological description of intermediate-strain behavior of rock when restricted to shift-invariant integral form. Here we will consider only scalar waves in one dimension, in the small displacement gradient approximation (Heming et al., 1998, in preparation, describe the generalization to 3D). Denoting the single stress and strain components by S and ϵ , respectively, (8) and (9) become

$$dS = G(d\epsilon - d\epsilon^p), \quad (10)$$

and

$$S = \int_0^{\epsilon} K(z - z') \frac{d\epsilon^p}{dz'} dz', \quad (11)$$

where G is the elastic modulus, and the intrinsic time increment dz is defined in terms of the plastic strain increment $d\epsilon^p$ by

$$dz \equiv |d\epsilon^p|. \quad (12)$$

If the kernel function is given, then, given an increment of strain, the stress increment can be calculated from the Equations 10-12, as we will show below.

If the kernel function is weakly singular at $z=0$, taking the form

$$K(z) \sim z^{-\alpha} \quad (13)$$

where α is positive, then the constitutive functional satisfies the 4 observational constraints on hysteresis loops noted in the previous section. In particular, Valanis and Read (1982) show that (13) implies that both initial loading and subsequent unloading and reloading at stress reversals will occur along the elastic slope G in the stress-strain plane, in general agreement with the behavior of rocks at intermediate strain levels.

Amplitude Scaling of Q

We can also demonstrate that the singular kernel ensures power law dependence of Q^{-1} on strain amplitude at intermediate strain levels, in agreement with the experimental observations reviewed earlier. We consider a cycle through a particular hysteresis loop $S_1(z)$. Construct $S_1(z)$ by the following sequence of steps. First load monotonically until the stress reaches some prescribed maximum value S_{1m} . At that point z equals some value z_1 , so $S_{1m}=S_1(z_1)$. Then unload and load in the reverse direction to $-S_{1m}$, corresponding to some $z=z_2$, and finally reverse again and reload back to S_{1m} , corresponding now to some $z=z_3$. The inelastic work W_1 done (per unit volume) by the load over the loop S_1 is

$$W_1 = \oint S_1(z) \frac{d\epsilon^p}{dz} dz. \quad (14)$$

Consider a similar cycle, but with the reversal-point stress amplitudes scaled such that z at each reversal point changes by some positive scale factor γ , to give reversals at γz_i , $i=1, 2, 3$. It is clear from (11-13) that the new stress function, denoted $S_\gamma(z)$, is a scaled version of S_1 ,

$$S_\gamma(z) = \gamma^{1-\alpha} S_1(\gamma^{-1} z), \quad (15)$$

By (14) and (15), the inelastic work W_γ over the scaled loop is

$$W_\gamma = \gamma^{2-\alpha} W_1. \quad (16)$$

We define Q^{-1} for a loop of a given amplitude, by analogy with viscoelastic Q^{-1} , as $1/2\pi$ times the ratio of net inelastic work done over the cycle to average strain energy during the cycle. We assume that the inelastic work is small compared with the average strain energy, i.e., $Q \gg 1$, in which case the peak strain is approximately proportional to peak stress, and the average strain energy is approximately proportional to the product of peak strain and peak stress. Then, combining (15) and (16), we find

$$Q_\gamma^{-1} = \gamma^\alpha Q_1^{-1}. \quad (17)$$

where Q_1 denotes Q for the reference loop S_1 . Using (15) we can rewrite the scale factor in (17) in terms of maximum stress amplitude, and with the low loss approximation noted above, we can replace maximum stress amplitude with maximum strain amplitude. Denoting the maximum strain amplitude by ϵ_m , and value of ϵ_m for the reference loop by ϵ_{1m} , we obtain

$$Q^{-1}(\epsilon_m) \approx \left(\frac{\epsilon_m}{\epsilon_{1m}} \right)^{\alpha/(1-\alpha)} Q^{-1}(\epsilon_{1m}), \quad (18)$$

where we have now written $Q(\epsilon_{1m})$ to denote Q_1 . Thus, Q^{-1} has approximately power law dependence on strain amplitude, with scaling exponent $\alpha/(1-\alpha)$. For the choice $\alpha = 1/2$, we have an approximately linear dependence of Q^{-1} on strain amplitude ϵ_m , in agreement with numerous laboratory observations.

Memory Variable Approximation

The integral form for the stress, (11), is intractable for numerical wave propagation computations, since the integral is performed over the entire strain history. This limitation is analogous to that faced in the numerical implementation of viscoelasticity (Day and Minster, 1984), and our solution is similar. That is, recognizing the convolutional form of (11), we can replace the integral with an approximation to the corresponding differential operator. This operator follows once the kernel function is expanded in terms of decaying exponentials in z (e.g., Valanis and Read 1982). We develop such an expansion for the kernel function C/z^α using the method of Prony (e.g., Marple, 1987), leading to an approximation of the form

$$K(z) = \sum_{r=1}^p A_r e^{-u_r z} \quad (19)$$

Once $K(z)$ is approximated by the exponential sum (19), (11) gives stress in the form

$$S = \sum_{r=1}^p q_r \quad (20)$$

where

$$q_r = A_r \int_0^z e^{-a_r(z-z')} \frac{d\epsilon^p}{dz'} dz' \quad (21)$$

The p constants a_r and A_r , are, respectively, the exponents and coefficients from the order p Prony expansion of K . Then (21) may be differentiated to yield the following linear, first-order differential equations for the p internal, or "memory," variables q_r :

$$\frac{dq_r}{dz} + a_r q_r = A_r \frac{d\epsilon^p}{dz} \quad r=1,2,\dots,p. \quad (22)$$

The integral form (11) has been changed to incremental form (22), and the memory requirement reduced to storing the p memory variables. It is no longer necessary to store the full strain history, nor even to explicitly save the reversal points. In practice, we have found that 3 to 4 memory variables per stress node provides an approximation adequate for simulation of wave propagation in the intermediate-strain range.

Numerical Solution

The constitutive equations now consist of (22), (10) and (12), which may be solved numerically. A convenient numerical scheme for the solution of such a system is given by Murakami and Read (1989). We found it necessary to generalize the Murakami and Read approach somewhat, retaining higher order accuracy in the time stepping of (22). Taking $d\epsilon^p/dz$ to be constant $\delta\epsilon^p/\delta z$, integrating (21) from z_0 to $z_0+\delta z$, we obtain

$$q_r(z_0 + \delta z) = q_r(z_0) e^{-a_r \delta z} + \frac{A_r}{a_r} (1 - e^{-a_r \delta z}) \frac{\delta\epsilon^p}{\delta z} \quad (23)$$

Combining (23) with (10), (12) and (20) yields

$$G \delta z + \sum_{r=1}^p \left(\frac{A_r}{a_r} - q_r(z_0) \frac{\delta\epsilon^p}{\delta z} \right) (1 - e^{-a_r \delta z}) = G \delta\epsilon \frac{\delta\epsilon^p}{\delta z} \quad (24)$$

Isolating $\delta\epsilon^p$ and squaring leads to an equation for δz which is easily solved numerically. Then (23) can be stepped forward by δz to update the memory variables, after which the updated stress is evaluated from (20).

3.5 FITTING QUASI-STATIC LABORATORY DATA

We have shown that the singular-kernel model is consistent with the main generic features of rock nonlinearity. Nonetheless, the model is essentially phenomenological, in that it is not derived from micromechanical considerations. The constant factor C which scales the kernel function must be calibrated by matching the model to laboratory stress-strain observations. Furthermore, the range of z over which the Prony expansion of the kernel is optimized will affect the shape of hysteresis loops at larger strain amplitudes, which introduces a further degree of freedom which may be constrained by fitting laboratory data. Here we fit the model to stress-strain data from quasi-static uniaxial tests of Berea sandstone (G. Boitnott and R. Haupt, New England Research, personal communication; Boitnott, 1992; 1993).

Typical raw laboratory data in the form of stress and strain histories are often rather noisy at the relatively low strain levels of interest to us, and require filtering. Simple low-pass filtering smooths the cusps, thereby masking the onset of nonlinear behavior, and affecting the measurement of moduli at and near the cusps. We have therefore developed a technique to filter separately the loading and unloading portions of the loops. It relies on the construction of a longer time series out of a half-loop—that is a portion of stress-strain history between two reversals, in which both stress and strain are monotonic. This is done by extending it in both directions with versions of itself, rotated by $\pm\pi$ about its end points. The extended time series is then de-meaned, de-trended, and low-pass filtered using a zero-phase filter to avoid introduction of a phase shift. The filtered version is truncated to the original length after restoring trend and mean, and the stress-strain path reconstructed by concatenation of filtered segments. The rotation by $\pm\pi$ of the extensions has the advantage of preserving the continuity of the time series and its derivative, thereby limiting undesirable end effects. It is important to avoid introducing cusps into hysteresis loops when they are not present, and to avoid smoothing through a cusp or changing its angle, when one is present. Too strong a filter will change the slope near the end points, and therefore introduce a fictitious cusp. Misapplication of the technique is detectable because this will create overlaps or gaps between successive segments. The technique gives very satisfactory results for noise levels as large as 10 percent, as we have been able to verify using synthetic loops contaminated with additive noise. This approach facilitates considerably the estimation of the tangent modulus, particularly near the loop ends where noise contamination is most worrisome.

We first find the two constants G and C . As shown by Valanis and Read (1982), if the kernel function takes the form $K(z) = C z^{-\alpha}$, then during the initial loading process the stress and strain have an explicit relationship which is

$$\epsilon = \frac{S}{G} + \left(\frac{(1-\alpha)S}{C} \right)^{1/(1-\alpha)} \quad (25)$$

We use a least squares fit to stress and strain values at hysteresis loop reversal points, for varying maximum stress levels, to determine the constants G and C . This is shown, for example, in Fig. 1a for the Berea sandstone data of Boitnott and Haupt. We then use the Prony expansion to get a_T and A_T . A comparison between the exact and approximate kernel functions for $\alpha=1/2$, using 4 terms in the expansion, is shown in Fig. 1b. The exponent is fixed at $\alpha=1/2$ since that value yields a linear dependence of Q^{-1} on strain amplitude, as shown by (18), a result consistent with experimental data. Table 1 lists all model parameters resulting from the fitting. Fig. 1c and 1d show a series of calculated hysteresis loops for the exact and approximate kernels, respectively. There is a saturation effect associated with the Prony approximation when the strain level is sufficiently high ($>10^{-4}$) which is not evident in these figures. This is due primarily to the exponential decay of the Prony approximation at large values of z_k , compared with the power law decay of the exact kernel. Further terms in the Prony approximation (and therefore additional memory variables) would be required to maintain the power law decay of the exact kernel to higher strain levels. Thus, data collected at very large strains may require a higher order approximation to achieve a good fit.

We test the resulting model by computing synthetic hysteresis loops for a range of maximum strain levels, which we compare with the corresponding laboratory curves. The comparison for 3 different peak strain levels is shown in Fig. 2. As illustrated in Figure 2, this model is very successful for modeling high signal-to-noise data sets such as the Berea sandstone loops for strain levels between $7-40 \times 10^{-6}$. The theoretical loops simulate the amplitude dependence of Q and the non-elliptical loop shapes, including cusps at the ends.

There is no reason that the elastic modulus G in the endochronic model need be constant. The modulus could be made strain dependent, thereby adding a component of nonlinear elasticity to the Berea model. Doing so does not discernibly improve the fit to the quasi-static data, however. Our preliminary model therefore uses a strain-independent modulus. But when we apply the preliminary model to wave propagation in the next section, comparison of the simulations with laboratory narrowband wave propagation data reveals a deficiency in the simulation of even harmonics of the source frequency. This deficiency is readily corrected by giving the elastic modulus a weak strain dependence. The generation of harmonics thus provides a particularly sensitive further test of the model.

In its ability to match observations of rock hysteresis, this approach represents a substantial improvement over attempts to simulate amplitude-dependent attenuation using

variants of viscoelasticity (Minster and Day, 1986; Minster et al., 1991; Day et al., 1992). Although purely phenomenological, the endochronic approach has the decided advantage that it readily reduces to a relatively simple differential equations which are easily programmed and solved numerically. The algorithm described above is sufficiently stable and efficient that it can be applied to compute stress-strain behavior in large numerical wave propagation simulations. Efficiency and stability of the algorithm are critical in large 2D or 3D simulations, in which 10^{10} or more evaluations of the constitutive functional will typically be necessary. We demonstrate the method for the 1D case.

3.6 NONLINEAR WAVE PROPAGATION

Methods

Standard Fourier synthesis methods for simulating ground motion fail when rock or soil nonlinearity is introduced into the continuum model. While considerable insight into the resultant wave propagation phenomena has been obtained through approximations (e.g., McCall, 1994), general treatment of the problem requires volume discretization methods such as finite differencing. In the intermediate strain regime, nonlinear losses, pulse distortions and harmonic generation have been well documented for solids in the laboratory. In this study, two methods have been developed for one-dimensional nonlinear wave propagation with the endochronic model: (i) a one dimensional fourth-order finite difference method which is fourth-order accurate in space (second order in time), and (ii) a one-dimensional pseudospectral method, with second-order finite differencing in time (e.g., Kosloff and Baysal, 1982; Fornberg, 1987; Daudt et al., 1989). In the latter method, spatial derivatives are approximated to infinite order via discrete Fourier transforms. We have found that these methods, both of which use spatial differencing of higher than second order accuracy, work well in this application, just as they known to in linearly elastodynamic computations. This is in part because we have confined consideration to sources with dominant wavenumber several octaves below the Nyquist wavenumber of the grid, and restricted the computations to relatively low strain levels. As a result, nonlinear effects are not strong enough to transfer appreciable energy to wavenumbers approaching the Nyquist. Since we are studying waves in the intermediate strain regime, shock and macroscopic failure phenomena are not important factors, and losses from hysteresis further smooth the wavefield. In this situation, the preponderance of the computational load arises from repeated evaluations of the constitutive functional. The computational advantage of using differencing of higher than second order thus becomes very attractive, because the number of stress evaluations for a given level of accuracy can be significantly reduced; in the case of fourth-order differencing, for example, stress evaluations can be reduced by approximately a factor of $2n$, relative to second-order differencing, where n is

the number of spatial dimensions. The pseudospectral method further reduces the relative contribution of the constitutive equations to the total computational load.

A further computational advantage of the fourth-order and pseudospectral methods over the second-order methods which may be more familiar in nonlinear computational studies is the reduction of numerical dispersion. Dispersion associated with low-order differencing mainly affects high frequencies, but in nonlinear computations (and in contrast to linear elastodynamic computations), numerical artifacts at high frequency can couple back into low frequency components of the wavefield, and vice versa. For this reason, artificial viscosity is essential in second-order nonlinear computations to continuously suppress the high frequency content. We have found, for the relatively low strain levels considered in this study, that both the fourth-order and pseudospectral methods obviate the need for artificial viscosity in intermediate-strain computations with the endochronic model. This simplifies the task of modeling and analyzing the spectral distortions introduced by the nonlinear constitutive model.

One of the better understood consequences of material nonlinearity on waveforms is harmonic distortion (e.g., Hirata et al., 1965; Breazeale and Ford, 1965). A monochromatic source generates harmonics which grow both with propagation distance and with source amplitude. Response to quasi-monochromatic excitation is of interest in its own right (for example, in the field of non-destructive testing (Bonner and Wanamaker, 1990, 1991; Morris et al, 1979)); it is also a starting point for building a good understanding of spectral distortions in nonlinear solids in general. Furthermore, previous analytical work and experimental results provide a starting point for validation and interpretation of numerical computations (Beresnev and Nikolaev, 1988; McCall, 1994; Meegan et al, 1993; Thompson and Tiersten, 1977). For these reasons, we will apply the numerical method to quasi-monochromatic sources in the following sections.

We have tested the two one dimensional wave propagation codes for the case of linear elasticity. With both methods, we calculated the propagation of a narrowband wavelet consisting of a sinusoid modulated with a Gaussian envelope and verified that the fundamental pulse remains invariant with distance and that no higher harmonics are generated in the spectra.

Nonlinear Elasticity

As a verification of the accuracy of the wave propagation calculations in a nonlinear problem, we present numerical results from nonlinear elastic wave propagation calculations. Much theoretical work has been focusing on wave propagation in nonlinear elastic materials (e.g., McCall, 1994). We compare the numerical solutions from finite difference and pseudospectral methods with the approximate analytical solutions obtained using McCall's perturbation expansion method. For this comparison, the stress-strain relationship is

$$\sigma = G(\epsilon)\epsilon, \quad (26)$$

where

$$G(\epsilon) = G_0(1 + \beta\epsilon), \quad (27)$$

and β is the cubic anharmonicity coefficient. We have set β to 5000, which is in the range of 10^3 - 10^4 for rock suggested by Johnson and McCall (1994), and near the estimate of Meegan et al. (1993) for Berea sandstone. The source is taken to be a longitudinal, planar force distribution (i.e., point force in 1D). For comparison with analytical results for monochromatic excitation, we use a narrowband source time function, a Gaussian-modulated sinusoid

$$F(t) = A \exp[-(t - 2wT)^2 / (wT)^2] \sin(2\pi t / T), \quad (28)$$

where T is the dominant period and w is a measure of the duration of the source, in units of the dominant period. Eqn. 28 has a Gaussian-shaped spectral peak with amplitude equal to the time domain peak amplitude times the factor $\sqrt{\pi}wT/2$. To ensure applicability of the perturbation solution, with which we wish to compare the numerical solution, the constant A was set to produce a relatively low peak strain amplitude of 0.6 μ strain. Numerical solutions were obtained by both finite difference and pseudospectral methods, using a grid spacing of 1/20 the dominant wavelength. The analytical solution for this source was approximated using the first and second perturbation terms obtained using the method given by McCall.

We specify the source strength in terms of the peak strain of the induced plane wave. We present results in dimensionless form, giving numerical results for dimensionless stress S/G_0 and velocity \dot{u}/c (where c is the infinitesimal-strain wavespeed). It then follows from the scaling relationship (7) that the solutions for these dimensionless quantities depend on propagation distance only through the ratio of distance to wavelength of the dominant frequency (i.e., x/cT , where c is the (infinitesimal-strain) wavespeed), and on time only through the ratio of time to the source period (i.e., t/T). The source duration w is set to 3 for all computations.

Fig. 3 shows the velocity spectra at distances from the source of 8 and 12 times the wavelength of the source frequency. The left half of the figure compares the numerical and analytical solutions near the fundamental frequency. The right half of the figure shows the comparison of solutions at the second multiple ($f=2/T$) and third multiple ($f=3/T$) of the source frequency. The comparison shows that the two numerical methods give nearly identical results for excitation of higher harmonics, and that both agree remarkably well

with the perturbation solution. The comparison confirms the applicability of our finite difference and pseudospectral methods to nonlinear problems, and incidentally verifies that McCall's perturbation solution is highly accurate in this instance.

We perform similar computations and examine the evolution with distance of the harmonics, and their dependence on source amplitude. For these computations, the source wave shape was slightly different from that used for the above comparison; we used a moment density to excite the plane wave, resulting in a velocity waveform which is the derivative of (28). For this narrowband source, the difference is negligible in both time domain waveform and in the spectral envelope (once we scale the source amplitude to produce a given peak strain amplitude). In particular, the ratio cited above between time domain peak and spectral peak (of the fundamental harmonic) still applies. The stress waveforms and spectra at distances 4, 8, 12, 16 wavelengths from the source, respectively, are shown in Fig. 4a for the case where peak strain is equal to $1.2 \mu\text{strain}$. As expected, the excitation of the higher harmonics is greater, at a given propagation distance, than was the case for the lower amplitude case in Figure 3.

Figures 4b shows the variation with propagation distance of both velocity waveforms and spectral amplitudes for the case of the $1.2 \mu\text{strain}$ source. Though significant higher order harmonics are evident in the spectra, and their amplitudes increase systematically with propagation distance, the waveforms themselves are nearly indistinguishable at the different distances. The inset shows the amplitudes of the second and third harmonics, as functions of propagation distance, in the form of ratios to the fundamental (source frequency) harmonic. Note that the growth rate of the second multiple approaches an asymptotic slope of 1, i.e., proportional to distance. This can be compared with the approximate theoretical result for purely monochromatic excitation (Thompson and Tiersten, 1977; McCall, 1994; Meegan et al., 1993), according to which the displacement amplitude U_{2f} of the harmonic at twice the source frequency, $2f_0$, depends on displacement amplitude U_f at the source frequency f_0 , the wavenumber k_0 of the source frequency, the nonlinearity parameter β , and distance x ,

$$U_{2f} = U_f^2 \frac{\beta k_0^2 x}{4}. \quad (29)$$

This result can also be written in dimensionless form as an expression for the ratio U_{2f}/U_f , in terms of the ratio L of distance to source wavelength and the strain amplitude E_f at the fundamental frequency f_0 .

$$\frac{U_{2f}}{U_f} = \frac{\pi}{2} \beta E_f L. \quad (30)$$

The asymptotic slope for the $2f_0$ harmonic in Fig. 4b indicates growth with the first power of distance, in agreement with (30). The growth rate differs somewhat from (30), as we would expect, since the source, while quite narrowband, is not purely monochromatic (note also that Eqn 30 gives the ratio of displacement amplitudes, and the velocity ratio \dot{U}_{2f}/\dot{U}_f appropriate for comparison with Fig. 4b is a factor of 2 higher). The asymptotic slope for the $3f_0$ harmonic is 2, which also agrees with theory (McCall, 1994), according to which \dot{U}_{3f}/\dot{U}_f is proportional to $(\beta E_f L)^2$.

Figure 4c shows the variation of the velocity spectral amplitudes with source amplitude, at a fixed distance of 13 wavelengths from the source. The calculations are again consistent with the scaling expected on the basis of (30). The fundamental component decreases slightly as it loses energy to the higher harmonics. The ratio \dot{U}_{2f}/\dot{U}_f increases nearly linearly with source strain amplitude, as predicted by (30); the ratio \dot{U}_{3f}/\dot{U}_f increases approximately with the square of the source strain amplitude, also in agreement with theory.

Berea Sandstone Model 1--Strain-Independent Elastic Modulus

The nonlinear elastic simulations in the last section were useful because they could be compared with analytical approximations, and that comparison demonstrates that the numerical methods can be used successfully to model pulse propagation and harmonic distortion. However, the nonlinear elastic model is not realistic for rocks, in that it neglects hysteresis and attenuation. In this section we examine the evolution of a plane wave propagating through the Berea sandstone model described earlier, represented with the endochronic formulation. This section considers the Berea model developed from quasi-static data alone, which has a constant (strain-independent) elastic modulus. Comparison of the results to data from wave propagation experiments will demonstrate the need (in the context of the constitutive formalism used here) to add a weakly strain-dependent term to the elastic modulus.

We use the same plane wave source described in the previous section, giving a plane wave at the source whose velocity waveform is the derivative of (28). Figure 5 shows the stress pulse after propagation by 4, 8, 12 and 16 fundamental-frequency wavelengths, for the case of a source with peak strain of $1.2 \mu\text{strain}$. While little change in wave shape is detectable in the time domain, a distinct decay of peak time-domain amplitude is evident, in contrast to the nonlinear elasticity results in Fig. 4a. Harmonic distortion effects are also evident, as seen in the spectral plots in Figure 5. As the pulse propagates, the amplitude of the fundamental component gradually diminishes with the propagation distance. The losses in the fundamental are much greater than the very small losses (attributable to energy transfer to higher harmonics) seen in the fundamental in the nonlinear elastic examples in the previous section, and are a consequence of the hysteresis in the Berea model. No viscous loss mechanism has been added to the Berea model derived earlier from fitting the endochronic model to laboratory data. Harmonics

representing the odd multiples of the fundamental frequency are generated and progressively increase in amplitude with propagation distance. The amplitudes of these odd harmonics are somewhat greater than they were for the nonlinear elastic case at the same strain level and propagation distance (i.e., Fig 4a). On the other hand, their growth rate appears to diminish with propagation distance. This can be understood as a consequence of increasing hysteretic loss at higher amplitude. The amplitudes of the harmonics are determined by competing effects: growth due to energy transfer from lower harmonics and attenuation due to amplitude-dependent losses in hysteresis.

The most striking characteristic of Fig. 5, in comparison with Fig. 4a, is the complete absence of the even harmonics in the Berea simulations. Spectra from wave propagation experiments in Berea sandstone presented by Meegan et al (1993), do show that the odd harmonics dominate the spectrum. These authors propose that higher order terms (i.e., cubic anharmonicity) might be required to explain the relative strength with which the odd harmonics are observed. Our simulations show that incorporation of realist hysteresis into the Berea model is capable of explaining dominance of the odd harmonics. On the other experiments, commonly show excitation of harmonics of both even and odd order (e.g., Beresnev and Nikolaev, 1988). The absence of the even harmonics in the Berea simulations shows that, despite accounting well for the shape of laboratory stress-strain curves, our Berea model lacks the slight asymmetry of response between loading and unloading directions present in, for example, the nonlinear elastic model with cubic anharmonicity. This model deficiency, while too subtle to be readily evident in comparisons of quasistatic stress-strain curves, becomes striking evident in the spectra of the wave propagation experiments. In this respect, the generation of harmonics provides a particularly sensitive test of nonlinear constitutive models.

Berea Sandstone Model 2--Strain-Dependent Elastic Modulus

In view of the foregoing results, we modify the Berea model through the addition of a strain dependence to the modulus G , as in (27), again using $\beta=5000$, and keeping the infinitesimal-strain value of the modulus, G_0 , equal to 8.96×10^9 . For strains up to about 10^{-5} , this change affects the modulus by at most 5%. The modified Berea model yields hysteresis loops whose agreement with the laboratory data is indistinguishable from that of the model with strain-independent modulus. Yet the harmonics generation predicted by the model is affected substantially.

Figure 6a shows the stress pulse at distances of 4, 8, 12, 16 wavelengths, together with the corresponding amplitude spectra, for a source with peak strain of $1.2 \mu\text{strain}$. The spectra exhibit some of the same features seen with the preliminary Berea model, including the progressive attenuation of the amplitude of the fundamental, strong excitation of the odd harmonics, and apparent reduction of the growth rate of the harmonics with propagation distance. In contrast to the preliminary model, however, the modified Berea

model also excites the even harmonics. Figures 6b shows the variation of particle velocity spectral amplitude with propagation distance (the inset shows ratios of the fundamental, second, and third harmonics to the initial amplitude of the fundamental). The second harmonic increases nearly linearly with distance and the third harmonic also increases, but at a slower rate. Comparison of Fig. 4b with the corresponding figure for nonlinear elasticity, Fig. 4b, shows some significant differences. The Berea model excites a significantly stronger $3f_0$ harmonic, for example. But, as a result of hysteretic losses, the amplitude of that harmonic quickly saturates with propagation distance in the Berea model, rather than continuing to grow. The $2f_0$ harmonic also shows some pronounced effects from hysteresis. It is somewhat weaker at all distances in the Berea model, compared with its amplitudes in the nonlinear elasticity model, even though the elastic modulus as a function of strain is the same in both cases. The second harmonic also shows a diminishing growth rate with increasing distance of propagation.

Both second and third harmonics exhibit approximately the same rate of increase with source amplitude in the modified Berea model, as Fig. 6c shows. Comparison with Fig. 4c again shows significant differences between the Berea model and nonlinear elasticity. The amplitude of the fundamental is nearly proportional to source amplitude for the nonlinear elasticity model, but diminishes with increasing source amplitude in the Berea model. The latter effect is a result of nonlinearity of the hysteretic loss mechanism, which leads to amplitude-dependence of apparent Q . The second and third harmonics have quite different rates of growth with source amplitude in the nonlinear elasticity case, but very similar dependence on source amplitude in the Berea model. The behavior of the Berea model reflects the competing effects of amplitude-dependent attenuation and energy transfer among harmonics.

Experiments have shown that propagation distortion from a dual frequency source is qualitatively different from what is seen with a single frequency source (Beresnev and Nikolaev, 1988; Bonner and Wanamaker, 1990, 1991; Johnson et al, 1987; Johnson and Shankland, 1989; Johnson et al., 1991). While a single-frequency source incurs only harmonic distortion, a two-frequency source is subject not only to harmonic distortion but also to intermodulation distortion, that is the production of components at frequencies which are the sums and differences of integer multiples of the two source frequencies.

We numerically simulate an intermodulation experiment for the Berea model using a two-frequency source consisting of a sum of narrowband sources of the form used in the previous simulations. The two source frequencies are in the ratio 3:2; their displacement amplitudes are equal, imparting a 3:2 ratio to their strain (and velocity and stress) amplitudes. The sources are scaled to give a combined peak strain at the source of $1.2 \mu\text{strain}$. Figure 7 shows the waveforms and the corresponding spectra, at distances of 4, 8, 12, and 16 wavelengths from the source, respectively. Spectral peaks associated with the sum and difference frequencies (e.g., f_1+f_2 , $2f_1+f_2$, f_1-f_2), are seen in this picture, as are the harmonics of the two source frequencies (e.g., $2f_1$, $2f_2$). At the relatively low source

strain amplitude used in this simulation, the harmonics and intermodulation terms remain relatively small compared with the fundamental source frequencies. Field experiments have shown that it is possible, under some circumstances and for some materials, for the higher harmonics from a monochromatic source, or the interaction-generated peaks from a dual frequency source, to exceed the amplitudes of the fundamental frequency components (Beresnev and Nikolaev, 1988).

3.7 DISCUSSION

The foregoing model for nonlinear rock behavior in the intermediate strain regime has relatively few parameters: G_0 , β , α , and C . Of these, the first is simply the elastic modulus. Of the 3 nonlinearity parameters, β is just the conventional cubic anharmonicity parameter, and we fix α to the value 1/2 to match the generally observed power law scaling of Q^{-1} with strain amplitude. Only C was adjusted to match the quasistatic observations of hysteresis in Berea sandstone. However, C can also be related to the slope of Q^{-1} versus strain amplitude. Thus, the model may be applicable in cases where one has an estimate of this slope, either from laboratory wave propagation experiments or from seismic observations, even if direct measurements of stress-strain curves are lacking. That is, it may have utility as a generic model for nonlinear seismic wave propagation in the intermediate strain range, parameterized by the anharmonicity coefficient and the Q^{-1} slope.

Besides having parameters which can be related to fairly standard observables, the model has the additional advantage of having governing equations which are easily programmed, require minimal storage, and are efficiently and stably solved. These latter attributes are essential in any constitutive model which is to be used in large, multi-dimensional wave propagation simulations. As an example, a typical 3D simulation with 300^3 grid cells will require of the order of 10^{10} to 10^{11} evaluations of the constitutive functional.

The endochronic formulation is not the only available theoretical framework for modeling the phenomenology of plasticity without a yield surface (e.g., Defalias and Popov, 1976; Bardet, 1996), and it is likely that other formulations can also be adapted to reproduce key observables associated with intermediate strain levels in rock, at least over some limited strain range. The endochronic formulation may itself be quite limited in its strain range of applicability. Its most significant limitation is probably that the endochronic constitutive model inevitably produces so-called "ratcheting" when cycled repeatedly over highly asymmetrical paths. That is, high-amplitude hysteresis loops cycled repeatedly through, e.g., one-sided loads, do not retrace themselves exactly. This phenomenon of ratcheting is also sometimes called cyclic creep. While this phenomenon can be turned to advantage for modeling the response of granular soils, where ratcheting is frequently observed experimentally, it is a decided limitation for modeling consolidated rock. Ratcheting in the Berea model, for example, becomes significant at strains exceeding

several 10's of μ strain, above which the endochronic formulation may not be appropriate for some applications.

The Fourier pseudospectral and fourth-order finite difference methods work well, without the incorporation of artificial viscosity, at the strain levels investigated here. However, this is largely because at the low strain levels which we simulated, there was negligible harmonic generation near the spatial Nyquist wavenumber. At higher strains, the stronger nonlinearity will excite those much higher harmonics significantly. It may be that incorporation of a realistic anelastic mechanism in series with the endochronic model will suffice to suppress these harmonics. Otherwise, it will be necessary to use smaller grid elements, artificial viscosity, or both, to achieve stable simulations at higher strain levels. If the generation of higher harmonics is not sufficiently counterbalanced by losses in hysteresis, it may become desirable to apply differencing methods tailored to strongly nonlinear waves (e.g., Cheng, 1996).

Quasi-harmonic numerical simulations with the Berea model reveal wave propagation phenomena which are absent in the nonlinear elastic simulations and theory. Decay of the fundamental frequency component was very evident in these simulations, in contrast to the nonlinear elastic case. In the nonlinear elastic simulations, decay of the fundamental was negligible at the strain levels and propagation distances considered here, resulting only from energy transfer to the higher harmonics. In the Berea model, however, decay of the fundamental was pronounced and strongly amplitude dependent. The attenuation of the fundamental was dominated by amplitude dependent hysteretic losses rather than by energy transfer.

Strong excitation of the third harmonic U_{3f} was also evident in our Berea simulations. This result is consistent with laboratory observations of wave propagation in Berea sandstone. Johnson and Rasolofosaon (1996) suggested that cubic anharmonicity alone may be inadequate to explain the high excitation level of harmonic U_{3f} , and proposed that hysteresis effects may be the most physically reasonable explanation (higher order anharmonicity being another potential contributor). Our Berea simulations provide some support for this proposal, demonstrating that a realistic model of hysteresis enhances the relative level of third harmonic excitation in a manner consistent with laboratory observations.

The Berea simulations also exhibit saturation effects in the growth of harmonics, i.e., reduction of harmonic growth rates with distance of propagation. This result reflects the amplitude dependence of the hysteretic loss mechanism--as amplitudes increase, increasing attenuation counteracts the energy transfer from low to higher harmonics. Similar saturation effects for harmonics have been measured experimentally in other solids (e.g., in copper by Breazeale and Ford, 1965).

It is easy to formally generalize the endochronic constitutive model to 2D or 3D, and the numerical procedures will not be significantly more complex. Such a generalization, however, entails more unknown parameters, including parameters

representing possible nonlinear coupling among the strain components. We have successfully fit the parameters of a model of this type to laboratory observations involving coupled volumetric and shear strains. The main difficulty is that there is no guarantee, *a priori*, that the resulting model (or any other purely phenomenological constitutive model) will accurately predict stress-strain behavior over loading paths much different from those used to obtain the fit. This caveat will apply to any purely phenomenological constitutive model. At a minimum, the method continues to provide, in 2D and 3D, a convenient way to parameterize laboratory hysteresis observations in a form suitable for efficient wave propagation computations. It may be possible to use observations of wave interactions (e.g., P-SV wave interactions, as in Qian, 1995) to provide further constraints on 2D or 3D forms of the model.

3.8 CONCLUSIONS

We have demonstrated a method for modeling nonlinear wave propagation in rock that appears to provide a stable, efficient, and accurate algorithm for numerical simulations at intermediate strain levels. The method is based upon a singular-kernel endochronic plasticity model of hysteresis, linked to either a finite difference or pseudospectral wave propagation scheme. The constitutive model preserves rate-independence (and simple scaling), produces hysteresis loops with initial loading and unloading at the elastic slope at reversal points, and provides a power law dependence of apparent Q^{-1} on strain amplitude. We have shown that the model parameters can be successfully fit to quasistatic stress-strain curves obtained at intermediate strain levels, and demonstrate the fit for Berea sandstone. The method should be applicable to other rocks under conditions for which attenuation is amplitude dependent, and will help fill an existing gap in seismic theory at intermediate strains.

Application of the Berea sandstone model to quasi-harmonic wave propagation reveals a number of contrasts with comparable simulations using nonlinear elasticity (with cubic anharmonicity). (i) The amplitude of the fundamental frequency component decays much more rapidly in the Berea model, indicating significant amplitude-dependent, hysteretic losses. (ii) The harmonic at 3 times the fundamental frequency is significantly larger for the Berea model, especially at short propagation distances, and in better agreement with laboratory measurements. (iii) Growth of higher harmonics with propagation distance in the Berea model shows a saturation effect, a behavior which is consistent with amplitude dependent attenuation, but which is absent from the nonlinear elasticity model. Application to dual-frequency wave propagation predicts the excitation of intermodulation distortions, with the production of components corresponding to sums and differences of integer multiples of the source frequency.

The methods of this paper have potential application to both applied and fundamental research problems in seismology, including modeling the influence of near-

source intermediate strains on the source signature of earthquakes and underground explosions. The methods may also have applications to the development of nondestructive seismic methods for *in situ* rock mass characterization.

3.9 REFERENCES

- Bardet, J.P., Scaled memory description of hysteretic material behavior, *Journal of Applied Mechanics, ASME*, 63, 750-757, 1996.
- Beresnev, I.A., and A.V. Nikolaev, Experimental investigations of nonlinear seismic effects, *Phys. Earth Planet. Interior*, 50, 83-87, 1988.
- Boitnott, G.N., Nonlinear attenuation in the near-source region: characterization of hysteresis in the deformation of rock joints, *Proc. 14th DARPA/PL Seismic Res. Symposium*, PL-TR-92-2210, ADA256711, 1992
- Boitnott, G.N., Fundamental observations concerning hysteresis in the deformation of intact and jointed rock with applications to nonlinear attenuation in the near source region, in *Proceedings of the Numerical Modeling for Underground Nuclear Test Monitoring Symposium, Los Alamos National Laboratory Report, LA-UR-93-3839*, 121, 1993.
- Bonner, B.P. and B.J. Wanamaker, Nonlinear acoustic effects in rocks and soils, in *Review of progress in quantitative nondestructive evaluation*, vol. 9, edited by D.O. Thompson and D.E. Chimenti, Plenum Press, New York, 1709-1713, 1990.
- Bonner B. P. and B.J. Wanamaker, Acoustic nonlinearities produced by macroscopic fractures in granite, in *Review of progress in quantitative nondestructive evaluation*, vol 10B, edited by D.O. Thompson and D.E. Chimenti, Plenum Press, New York, 1861-1867, 1991.
- Breazeale, M.A. and J. Ford, Ultrasonic studies of the nonlinear behavior of solids, *J. Appl. Phys.*, 36, 3486-3490, 1965.
- Cheng, N., Nonlinear wave propagation in sandstone: A numerical study, *Geophysics*, 61, 1935-1938, 1996.
- Daudt, C.R., L.W. Braile, R.L. Nowack and C.S. Chiang, A comparison of finite difference and Fourier method calculations of synthetic seismograms, *Bull. Seism. Soc. Amer.*, 79, 1210-1230, 1989.
- Day, S.M., J.B. Minster, and L. Yu, Numerical simulation of nonlinear attenuation using an endochronic formulation, *Proc. 14th DARPA/PL Seismic Res. Symposium*, PL-TR-92-2210, ADA256711, 1992.

- Day, S.M. and J.B. Minster, Numerical simulation of attenuated wavefields using a Pade approximant method, *Geophys. J. R. Astr. Soc.*, 78, 105-118, 1984.
- Defalias, Y.F., and E. Popov, Plastic internal variables formalism of cyclic plasticity, *Journal of Applied Mechanics*, 98, 645-651, 1976.
- Fornberg, B., The pseudospectral method: Comparison with finite difference for the elastic wave equation, *Geophysics*, 52, 483-501.
- Gordon, R.B. and L.A. Davis, Velocity and attenuation of seismic waves in imperfectly elastic rock, *J. Geophys. Res.*, 73, 3917-3935, 1968.
- Guyer, R.A., K.R. McCall, and G.N. Boitnott, Hysteresis, discrete memory, and nonlinear wave propagation in rock: A new paradigm, *Physical Review Letters*, 74, 3491-3494, 1995.
- Guyer, R.A., K.R. McCall, G.N. Boitnott, L.B. Hilbert Jr., and T.J. Plona, Quantitative implementation of Preisach-Mayergoyz space to find static and dynamic elastic moduli in rock, *J. Geophys. Res.*, 102, 5281-5293, 1997.
- Hirata, A., B.B. Chick, and C. Elbaum, Dislocation contribution to the second harmonic generation of ultrasonic waves, *J. Appl. Phys.*, 36, 229-236, 1965.
- Kosloff, D., and E. Baysal, Forward modeling by a Fourier method, *Geophysics*, 47, 1402-1412, 1982.
- Johnson, P.A., and P.N.J. Rasolofosaon, Manifestation of nonlinear elasticity in rock: Convincing evidence over large frequency and strain intervals from laboratory studies, *Nonlinear Processes in Geophysics*, 3, 77-88, 1996.
- Johnson, P.A., T.J. Shankland, R.J. O'Connell and J.N. Albright, Nonlinear generation of elastic waves in crystalline rock, *J. Geophys. Res.*, 92, 3597-3602, 1987.
- Johnson, P.A. and T.J. Shankland, Nonlinear generation of elastic waves in granite and sandstone: continuous wave and travel time observations, *J. Geophys. Res.*, 94, 17729-17733, 1989.
- Johnson, P.A., A. Migliori, and T.J. Shankland, Continuous wave phase detection for probing nonlinear elastic wave interactions in rocks, *J. Acoust. Soc. Amer.*, 89, 598-603, 1991.

- Johnson, P.A. and K.R. McCall, Observation and implications of nonlinear elastic wave response in rock, *Geophys. Res. Lett.*, 21, 165-168, 1994
- Johnston, D.H., and M.N. Toksoz, Thermal cracking and amplitude dependent attenuation, *J. Geophys. Res.*, 85, 937-942, 1980.
- Liu H-P, L. Peselnick, Mechanical hysteresis loops of an anelastic solid and the determination of rock attenuation properties, *Geophys. Res. Lett.*, 6, 545-548, 1979.
- Marple, S.L., *Digital spectral analysis with applications*, Eaglewood Cliffs, N. J., Prentice-Hall, 1987.
- Mashinsky, E.I., Quasi-microplasticity processes and nonlinear seismicity, *Phys. Solid Earth*, 30, 97-102, 1994.
- Matsumoto, E., Variation of the strain spectra of random waves in nonlinear elastic materials, *J. Acoust. Soc. Amer.* 81, 1713-1717, 1987.
- Mavko, G.M., Frictional attenuation: An inherent amplitude dependence, *J. Geophys. Res.* 84, 4769-4775.
- McCall, K.R., Theoretical study of nonlinear elastic wave propagation, *J. Geophys. Res.*, 99, 2591 - 2600, 1994.
- McCall, K.R. and R.A. Guyer, Equation of state and wave propagation in hysteretic nonlinear elastic materials, *J. Geophys. Res.*, 99, 23887, 1994.
- McKavanagh, B. and F.D. Stacey, Mechanical hysteresis in rocks at low strain amplitudes and seismic frequencies, *Phys. Earth Planet. Interior*, 8, 246-250, 1974.
- Meegan, G.D., P.A. Johnson, R.A. Guyer, and K.R. McCall, Observations of nonlinear elastic wave behavior in sandstone, *J. Acoust. Soc. Amer.*, 94, 3387-3391, 1993.
- Minster, J.B., Anelasticity and attenuation, in *Physics of the Earth's Interior, Proceeding of the International Schools of Physics " Enrico Fermi "*, edited by A.M. Dziewonski and E. Boschi, pp151-212, North-Holland, Amsterdam, 1980.
- Minster, J.B. and S.M. Day, Decay of wave fields near an explosive source due to high-strain, nonlinear attenuation, *J. Geophys. Res.*, 91, 2113-2122, 1986.

- Minster, J.B, S.M. Day, and P.M. Shearer, The transition to the elastic regime in the vicinity of an underground explosion, in *Explosion Source Phenomenology, American Geophysical Union Monograph 65*, 229-238, 1991.
- Morris, W.L., O. Buck and R.V. Inman, Acoustic harmonic generation due to fatigue damage in high-strength aluminum, *J. Appl. Phys.*, 50, 6737-6741, 1979.
- Murakami, H and H.E. Read, A second-order numerical scheme for integrating the endochronic plasticity equations, *Computers and Structures*, 31, 663-672, 1989
- Nazarov, V. E., L.A. Ostrovsky, I.A. Soustova and A.M. Sutin, Nonlinear acoustics of micro-inhomogeneous media, *Phys. Earth Planet. Interior*, 50, 65-73, 1988.
- Qian, Z., Nonlinear interaction between P and SV wave in isotropic elastic media, *Chinese J. Acoust.*, 14, 193-199, 1995.
- Stewart, R. R., M.N. Toksoz and A. Timur, Strain-dependent attenuation: Observations and a proposed mechanism, *J. Geophys. Res.*, 88,546-554, 1983
- Thompson, R.B., O. Buck and D.O. Thompson, Higher harmonics of finite amplitude waves in solids, *J. Acoust. Soc. Amer.*, 59, 1087-1094, 1976.
- Thompson, R.B. and H.F. Tiersten, Harmonic generation of longitudinal elastic waves, *J. Acoust. Soc. Amer.*, 62, 33-37, 1977.
- Valanis, K., and H. Read, A new endochronic plasticity model for soils, S-CUBED report, SSS-R-80-4292, San Diego, Calif., 1982.
- Valanis, K., and J. Fang, Endochronic analysis of cyclic elastoplastic strain fields in a notched plate, *J. Appl. Mechanics*, 50, 789-794, 1983.
- Valanis, K. and F. Lee, Endochronic theory of cyclic plasticity with applications, *J. Appl. Mechanics*, 51, 367-374, 1984
- Winkler, K., A. Nur, and M. Gladwin, Friction and seismic attenuation in rocks, *Nature*, 227, 528-531, 1979.
- Wortman, W.R., and G.D. McCartor, Nonlinear seismic attenuation from Cowboy and other explosive sources, *Mission Research Corporation Report MRC-R-1107*, 1987.

FIGURE CAPTIONS

Figure 1: Fitting the constitutive model to Berea sandstone data. (a) Calculation of the elastic modulus G and hysteresis parameter C from the reversal points. Stars denote observations, and the dashed curve is the model prediction using the optimal values of G and C . The parameter α was fixed at a value of $1/2$. (b) Prony approximation to the kernel function, in the range $z=2 \times 10^{-8}$ to 4×10^{-4} . The exact kernel is shown as a solid curve, the approximation as a dashed curve. (c) The resulting synthetic hysteresis loops calculated by direct integration using the exact kernel function, at maximum strain levels of 10, 15, 20, 25, 30, 35, 40, 45 and 50 μ strains, respectively. (d) Same as (c), but calculated using the Prony approximation to the kernel.

Figure 2: Comparison of hysteresis loops calculated from the Prony approximation kernel described in Fig. 1, dashed lines), with observed loops for Berea sandstone, solid lines (G. Boitnott and R. Haupt, New England Research, Inc., personal communication). Peak strain levels are 7.4, 9, 19.6 and 37 μ strains, respectively.

Figure 3: Propagation of a quasi-harmonic plane wave in a nonlinearly elastic medium: comparison of approximate analytic solution, obtained by the method of McCall (1994), with finite difference and pseudospectral numerical solutions. The analytic solution is shown by the solid curve. The two numerical solutions are indistinguishable from each other, and only the pseudospectral case is plotted. The source was scaled to give a maximum time domain strain of 0.6×10^{-6} . Diamonds and stars denote the numerical solution at distances of 8 and 12 times the source wavelengths, respectively. The left portion of the figure shows the spectrum near the source frequency, and the right portion shows the next two higher order harmonics. Frequency has been normalized by the source frequency ($1/T$). The velocity spectral amplitude V has been normalized by the wavelength of the source excitation ($1/cT$).

Figure 4: (a) Numerical solution for the evolution of a modulated sinusoidal pulse, with increasing propagation distance, in a nonlinearly elastic solid with cubic anharmonicity. The maximum strain of the source pulse is 1.2×10^{-6} . Stress waveforms (shown in the inset) and the corresponding spectra are shown for propagation distances of 4, 8, 12, and 16 wavelengths. (b) The same results shown in the form of particle velocity spectra. The inset shows the spectral ratios of the $2f_0$ and $3f_0$ harmonics, respectively, to the fundamental. The harmonics increase with distance as predicted by theory. (c) Variations of the amplitude spectra with strain amplitude of the source, at fixed position 13 wavelengths from the source. The amplitude scaling of the numerical solution agrees with theory. The source strain amplitudes are 0.24, 0.6, 1.2, and 2.3 μ strain, respectively.

Figure 5: Numerical solution for the evolution of a modulated sinusoidal pulse, with increasing propagation distance, in the preliminary Berea model (i.e., without strain dependence of the elastic modulus). The maximum strain of the source pulse was 1.2×10^{-6} . Waveforms (shown in the inset) and the corresponding spectra are shown for propagation distances of 4, 8, 12, and 16 wavelengths. Note the complete absence of even-order harmonics in this case, as well as the attenuation of the fundamental component with distance, distinguishing this model from the nonlinear elastic model.

Figure 6: (a) Numerical solution for the evolution of a modulated sinusoidal pulse, with increasing propagation distance, in the final Berea sandstone model (with strain-dependent elastic modulus). The maximum strain of the source pulse is 1.2×10^{-6} . Stress waveforms (shown in the inset) and the corresponding spectra are shown for propagation distances of 4, 8, 12, and 16 wavelengths. (b) The same results shown in the form of particle velocity spectra. The inset shows the spectral ratios of the $2f_0$ and $3f_0$ harmonics, respectively, to the fundamental. The increase with distance of the higher order harmonics shows saturation effect associated with nonlinear attenuation. (c) Variations of the amplitude spectra with strain amplitude of the source, at fixed position 13 wavelengths from the source. The source strain amplitudes are 0.3, 0.6, 1.2, and $2.4 \mu\text{strain}$, respectively.

Figure 7: Numerical solution for the evolution of a sum of modulated sinusoids, with increasing propagation distance, in the final Berea sandstone model (with strain-dependent elastic modulus). The maximum strain of the source pulse is 1.2×10^{-6} . Waveforms (shown in the inset) and the corresponding spectra are shown for propagation distances of 4, 8, 12, and 16 wavelengths. Note the generation of spectral peaks at frequencies equal to sums and differences of integer multiples of the source frequencies.

Table 1. Model Parameters

Constitutive Model		Prony Expansion	
G_0	$8.96 \times 10^9 \text{ Pa}$	A_1	$3.61 \times 10^{10} \text{ Pa}$
C	$3.87 \times 10^7 \text{ Pa}$	A_2	$1.49 \times 10^{11} \text{ Pa}$
β	5×10^3	A_3	$5.67 \times 10^{10} \text{ Pa}$
α	$1/2$	A_4	$4.56 \times 10^{11} \text{ Pa}$
		a_1	1.0×10^5
		a_2	5.07×10^6
		a_3	2.75×10^7
		a_4	9.27×10^7

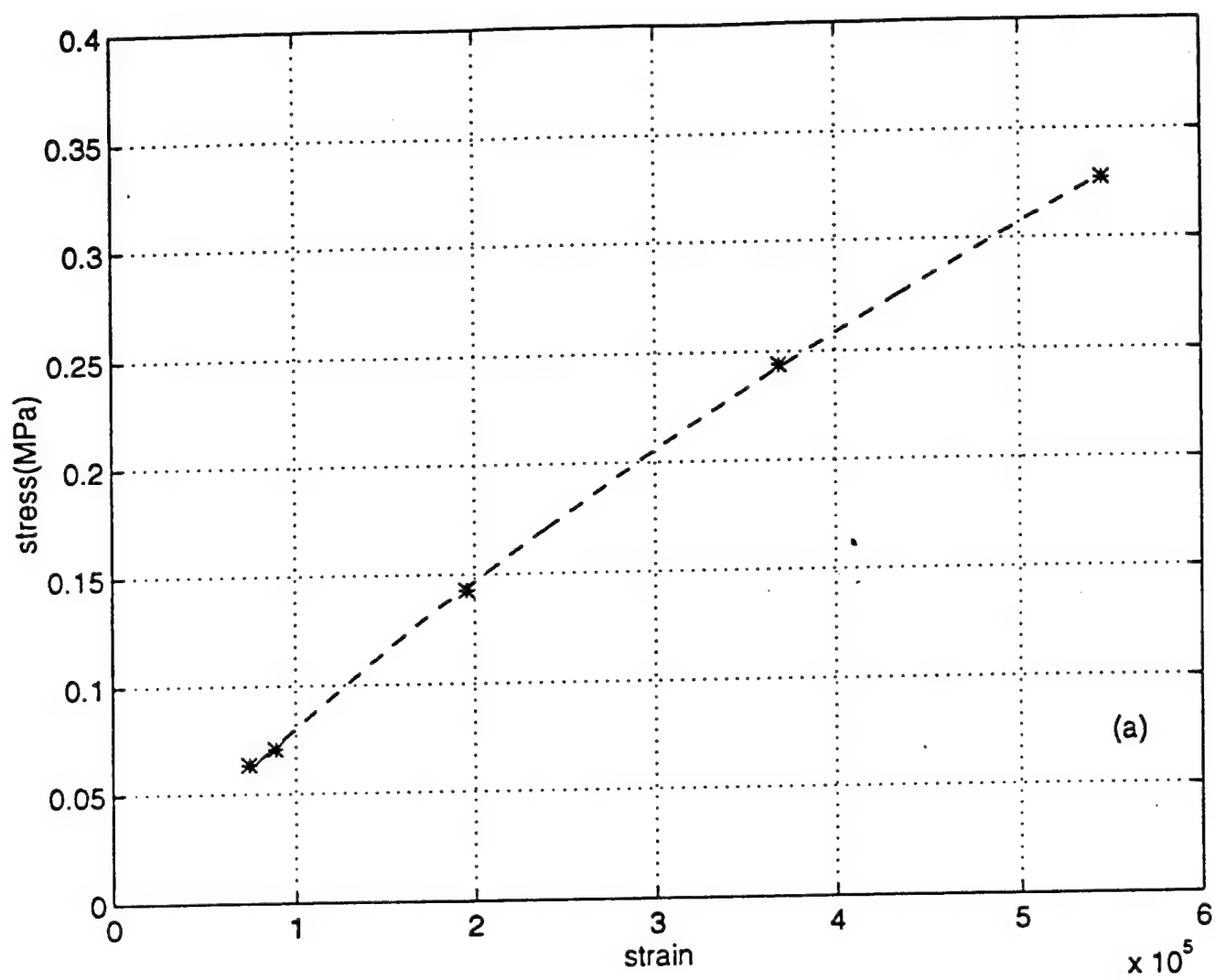


FIGURE 1 (a)

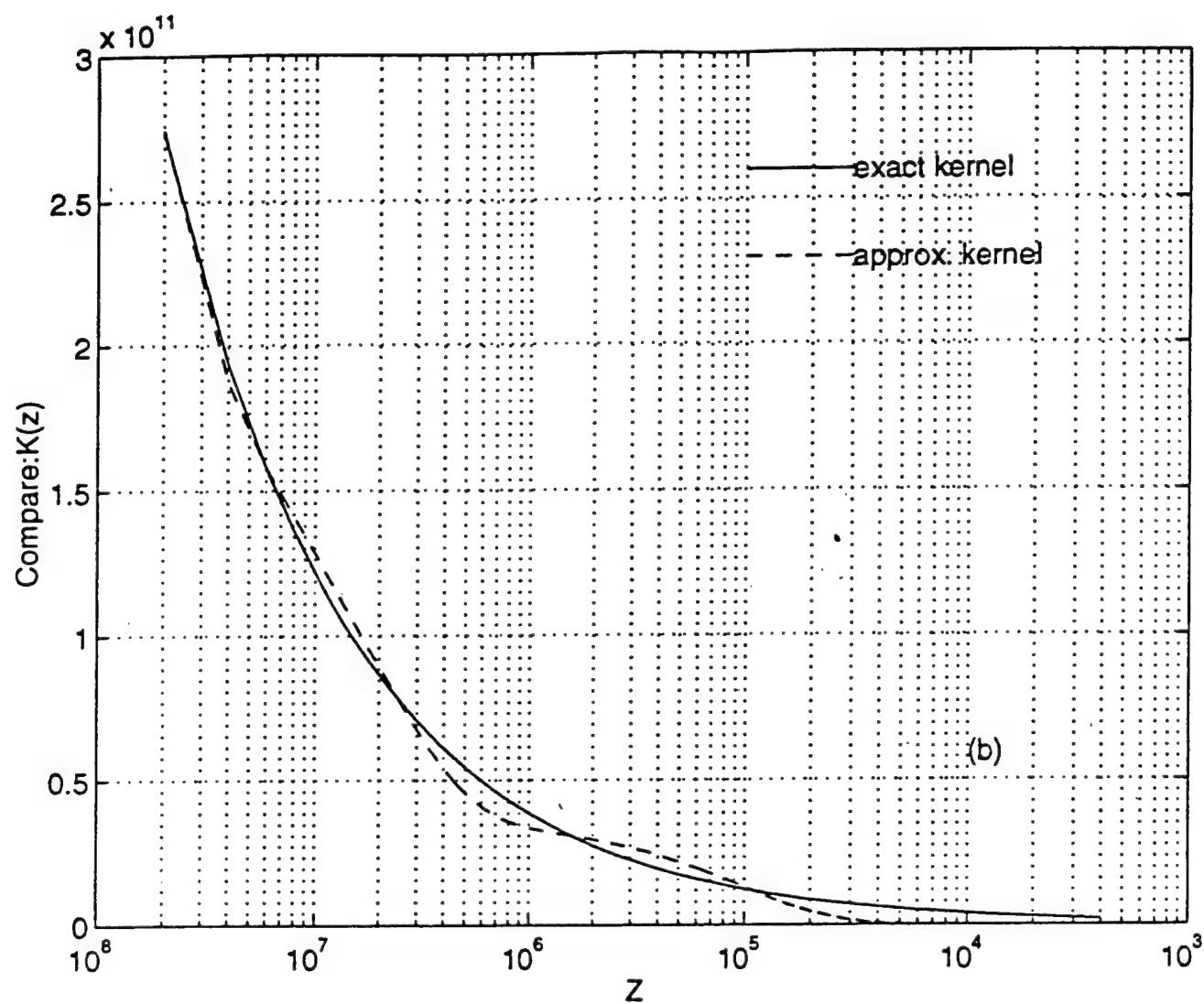


FIGURE 1 (b)

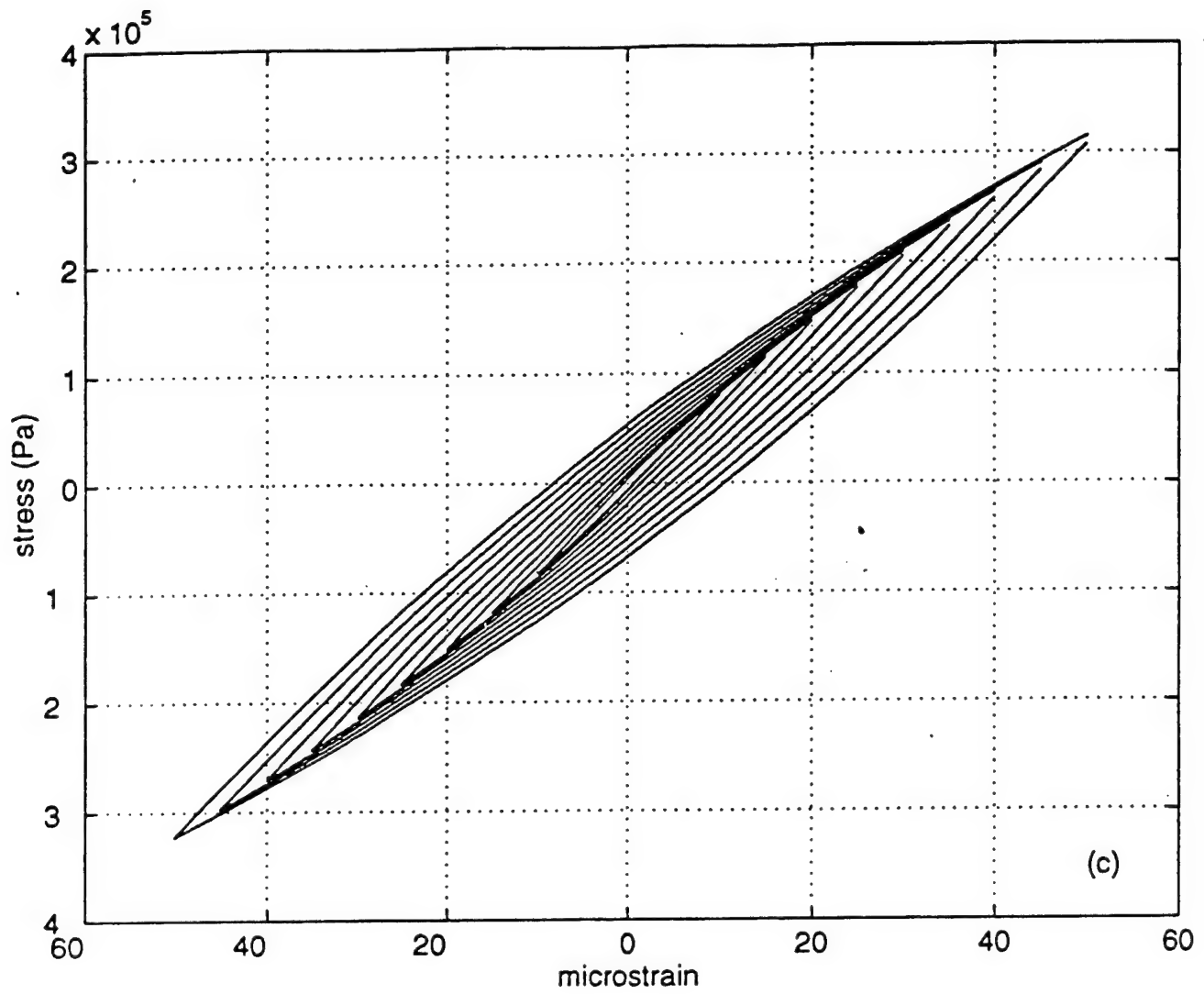


FIGURE 1 (c)

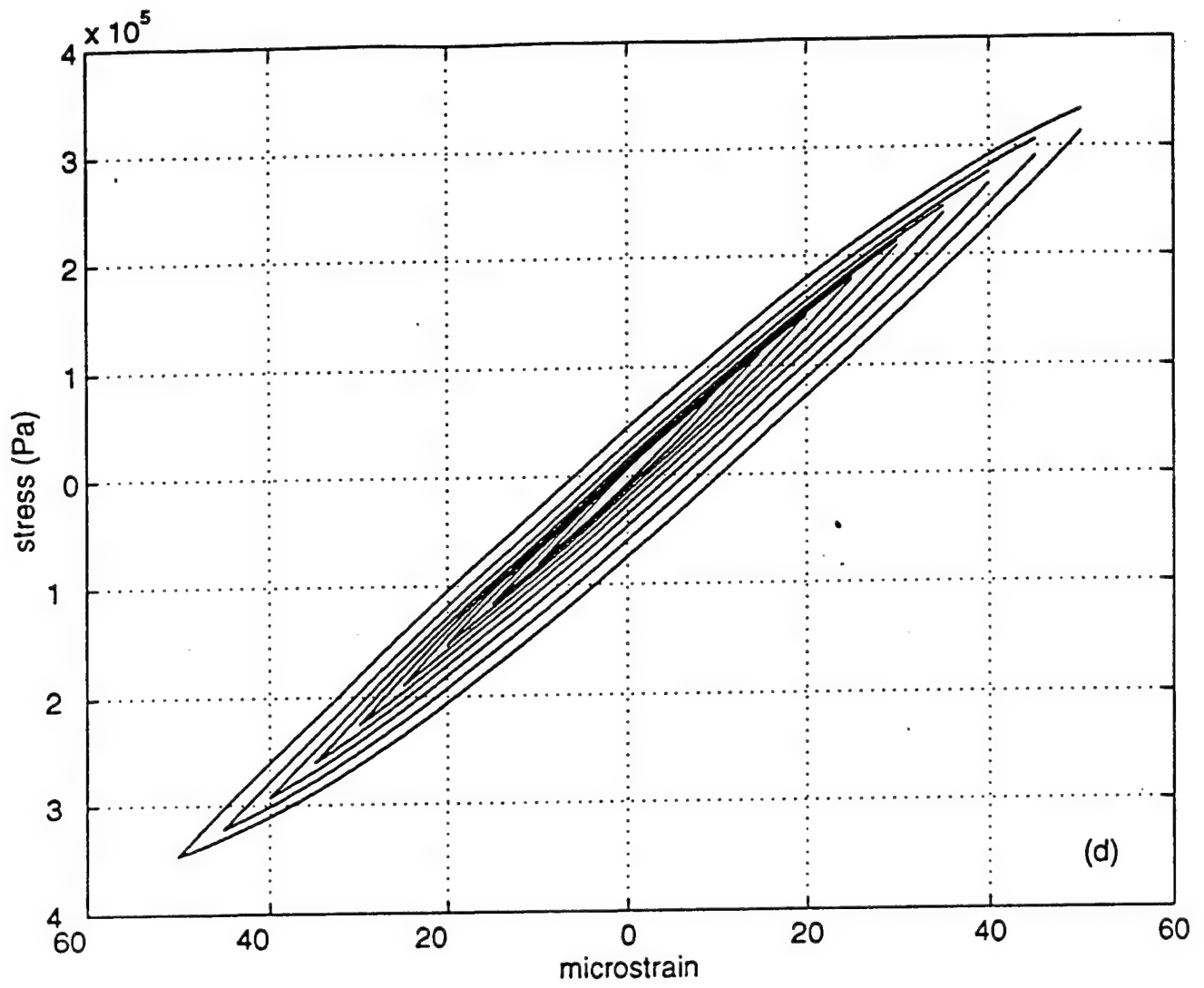


FIGURE 1 (d)

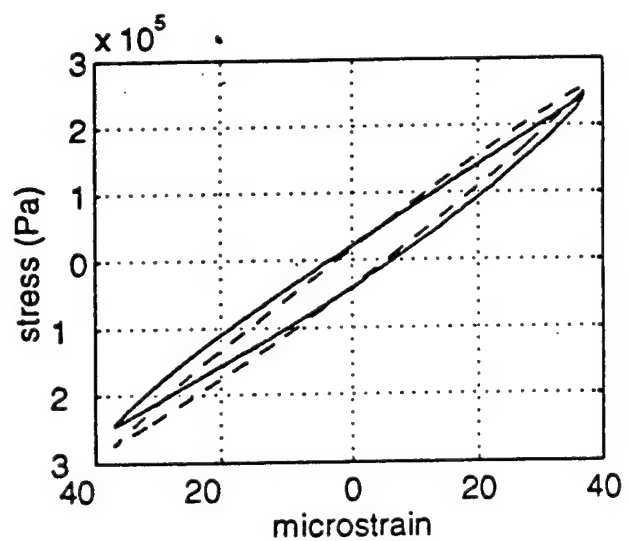
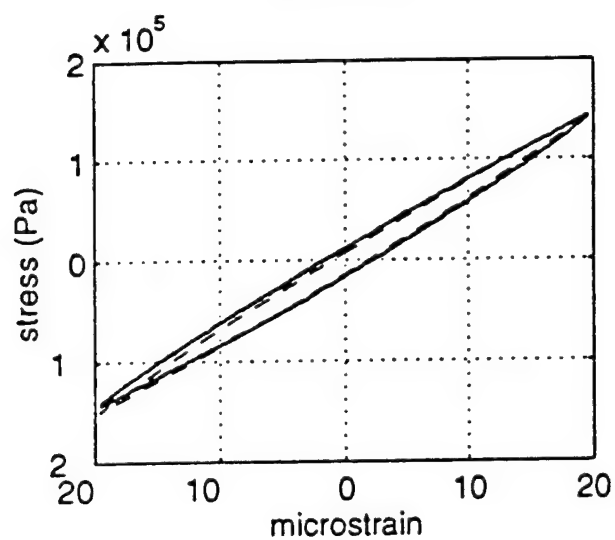
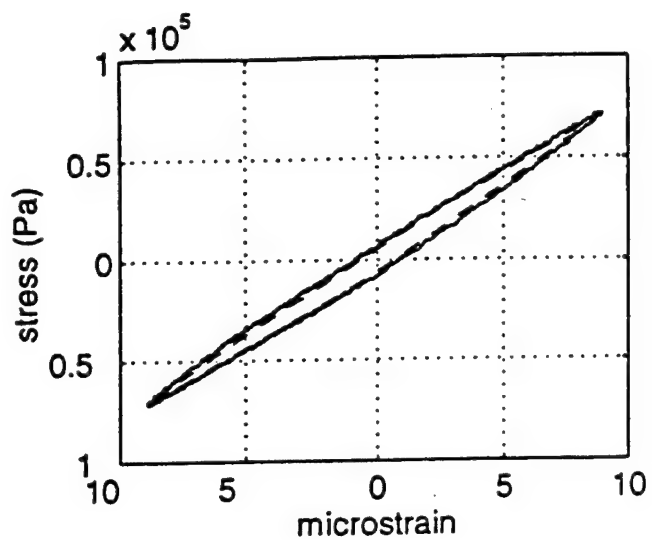
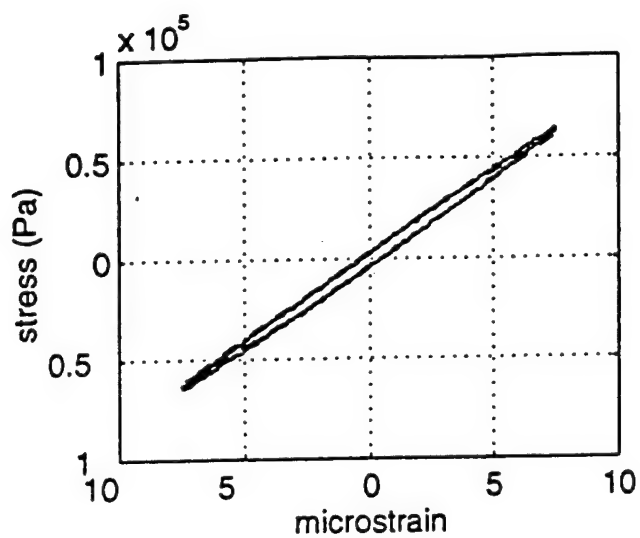


FIGURE 2

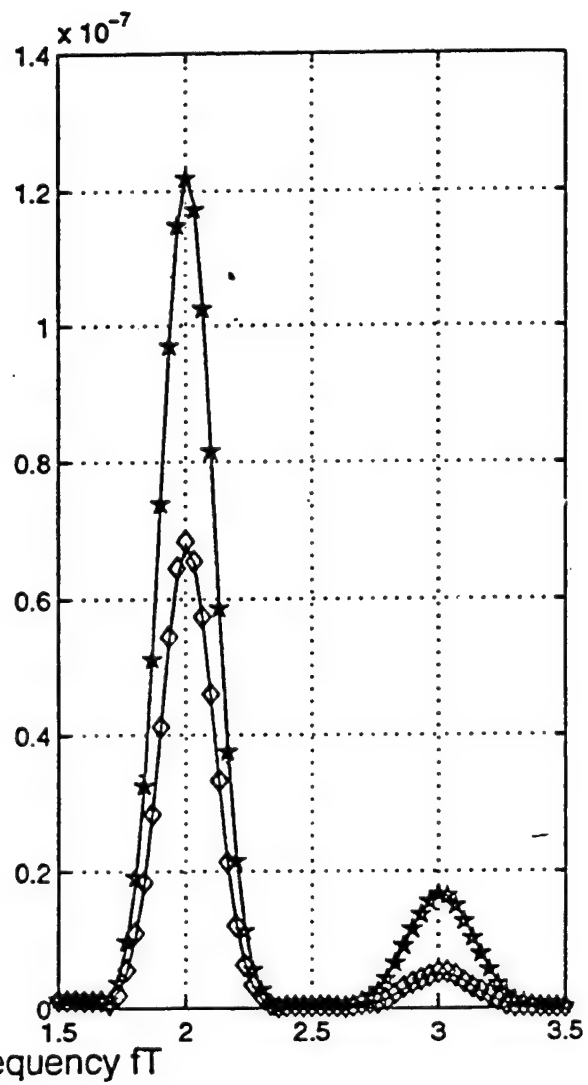
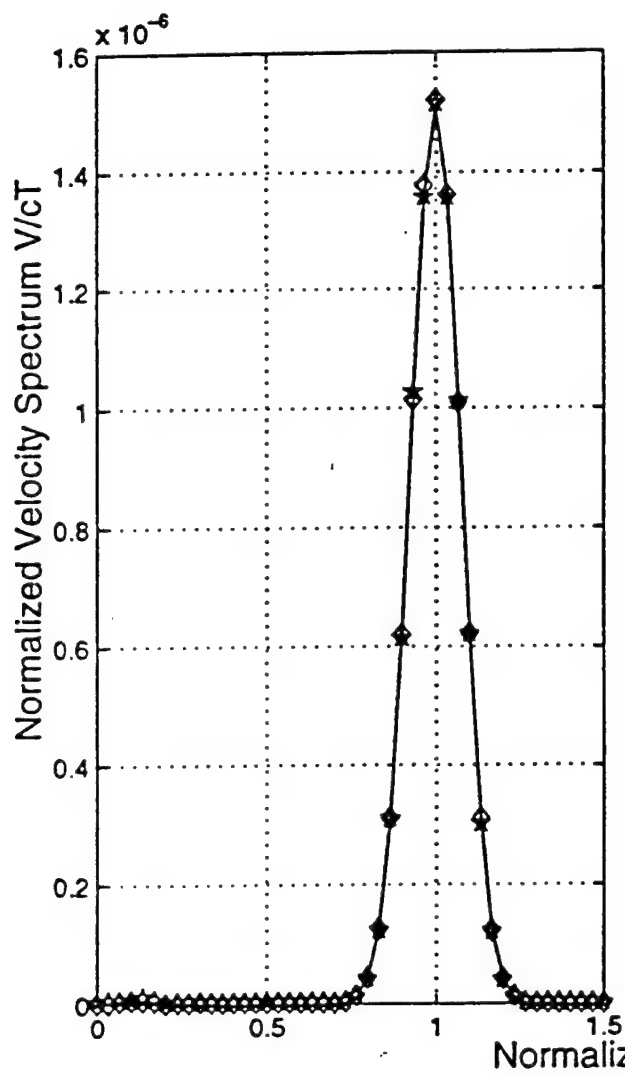


FIGURE 3

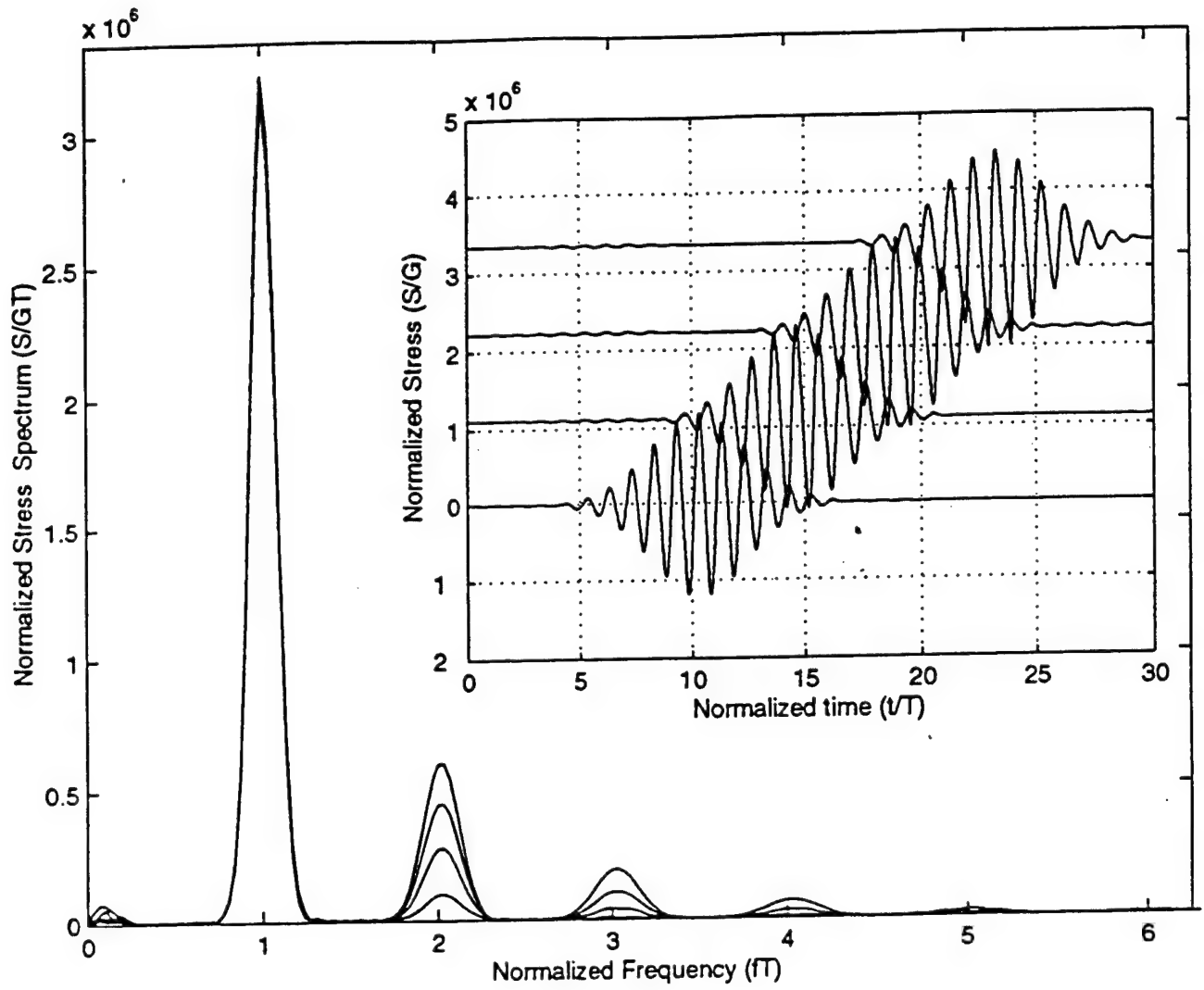


FIGURE 4 (a)

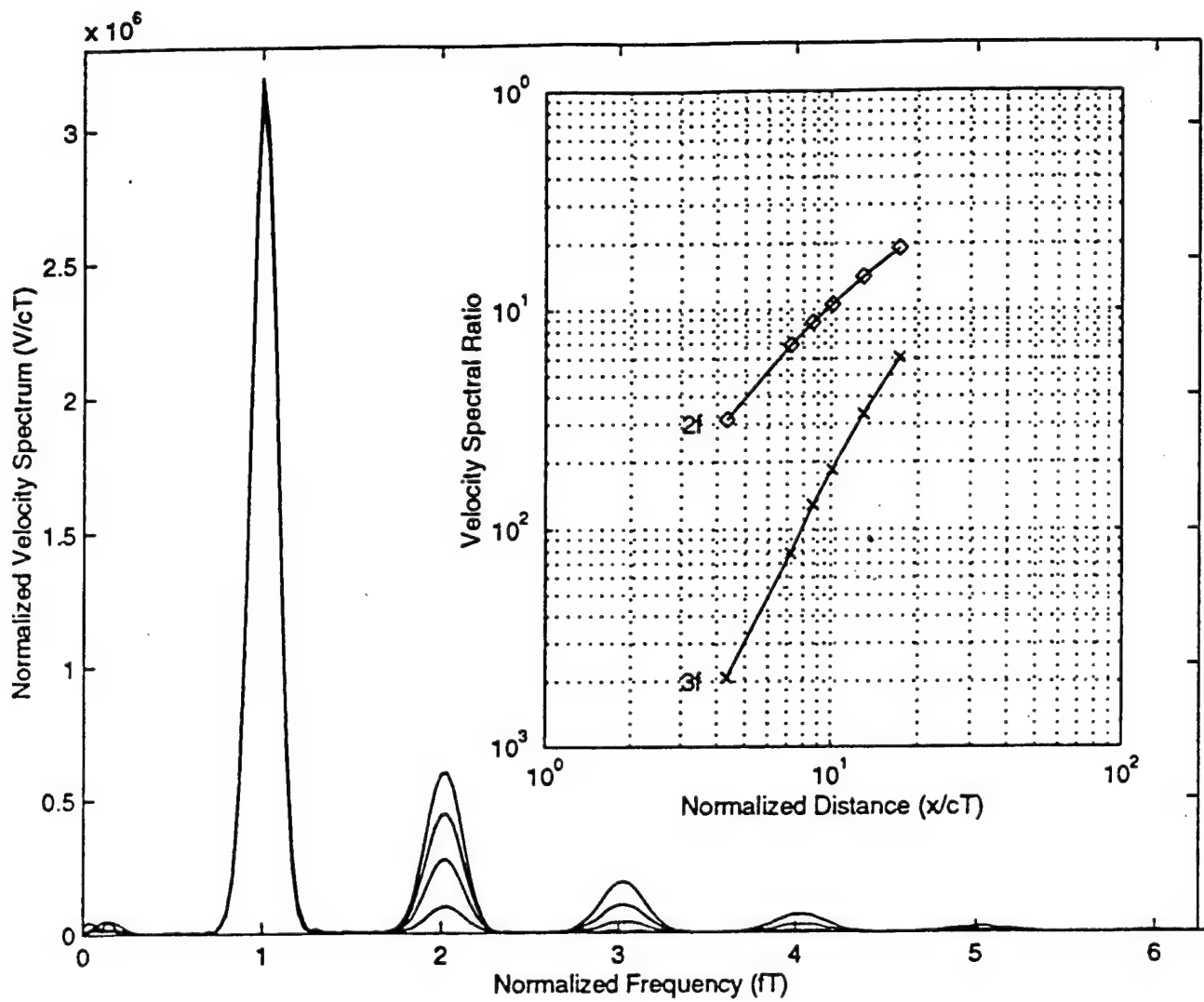


FIGURE 4 (b)

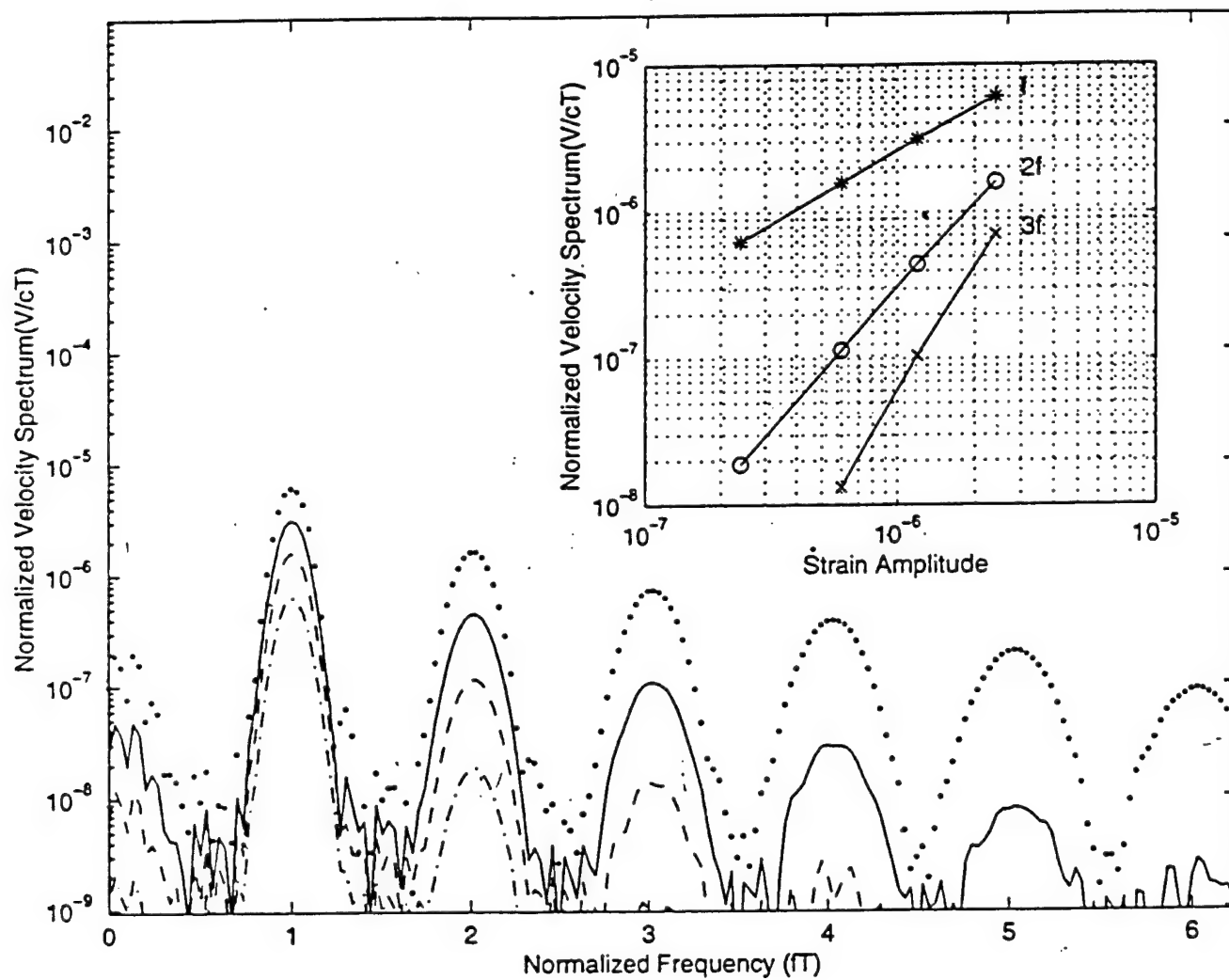


FIGURE 4 (c)

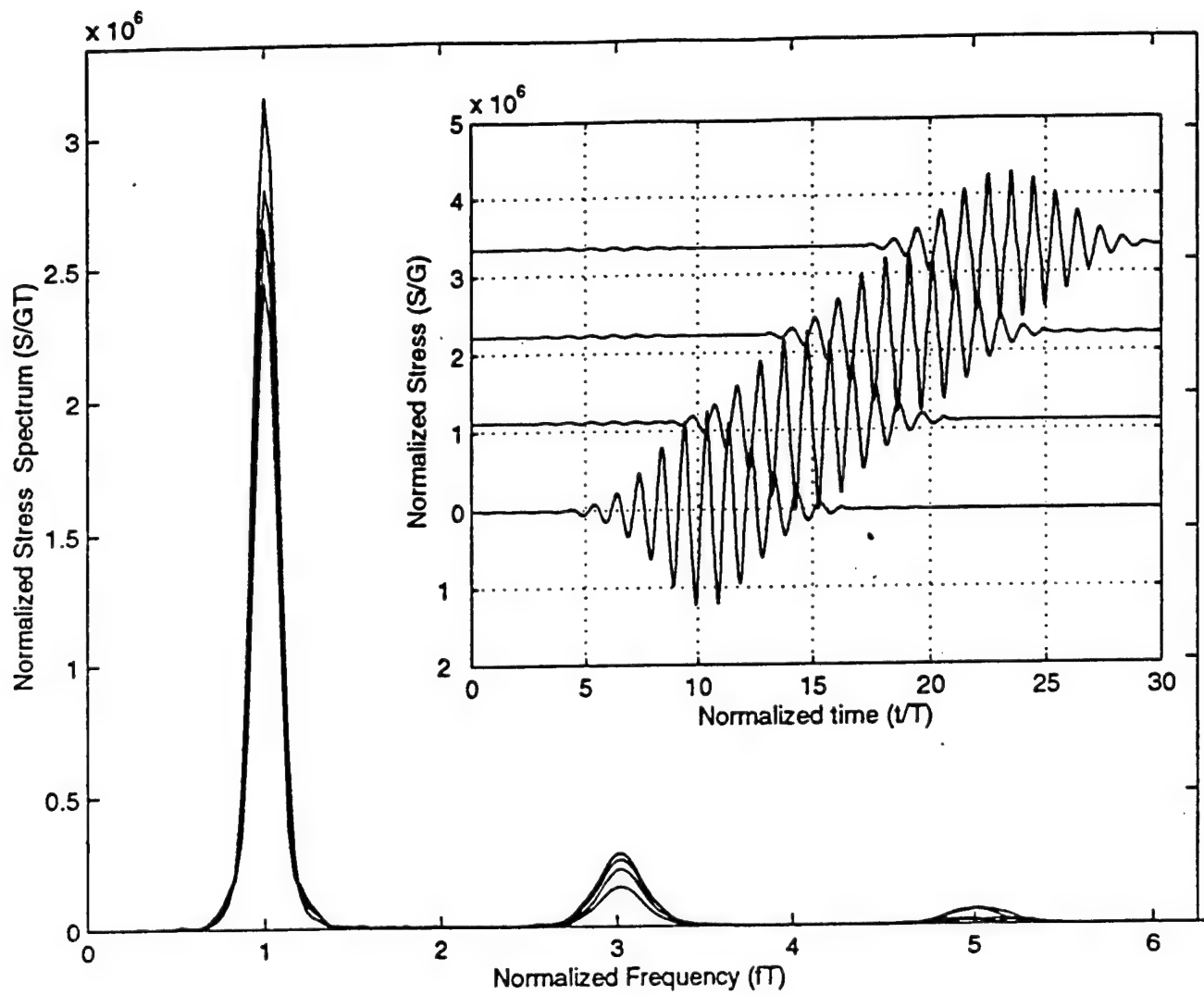


FIGURE 5

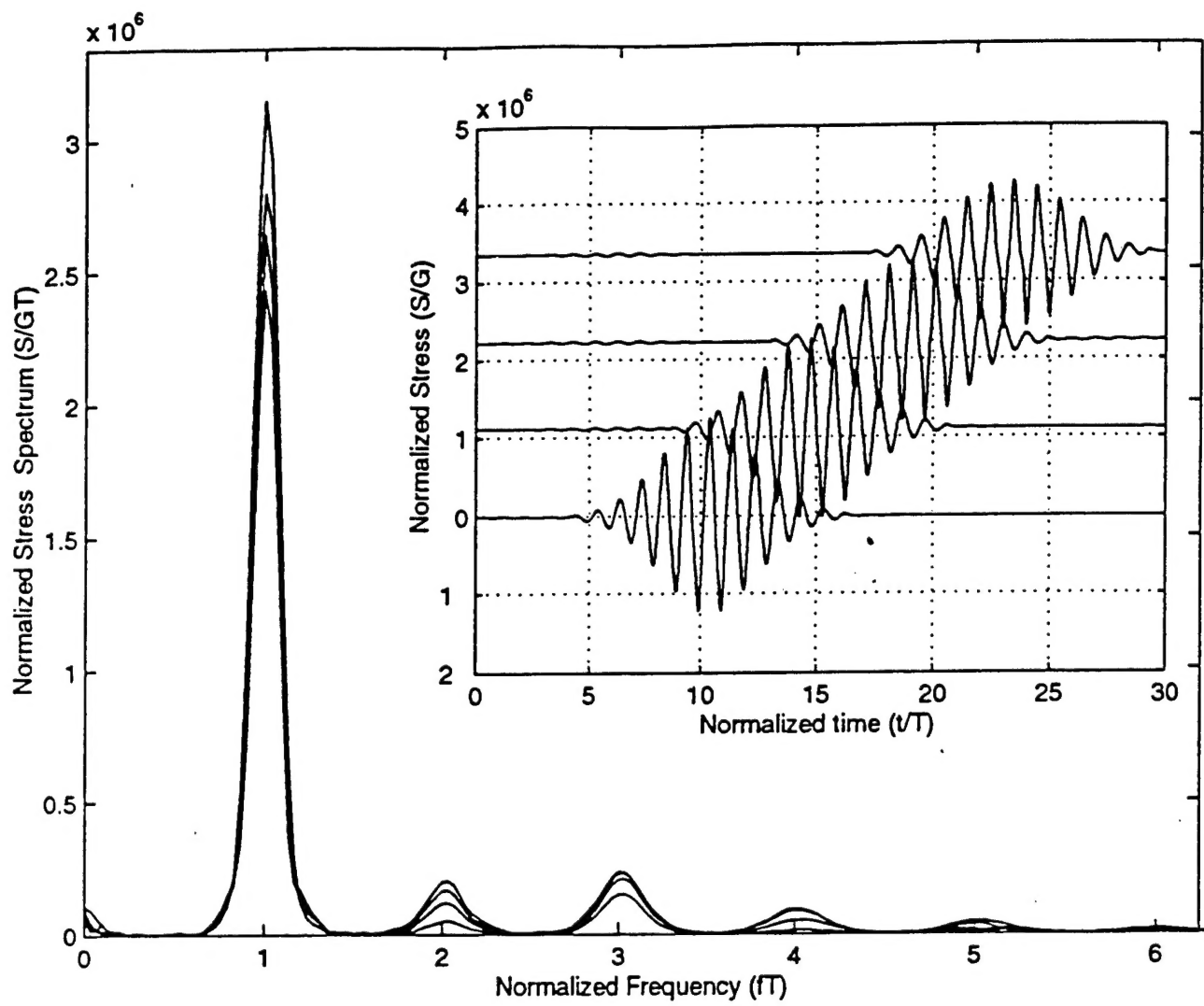


FIGURE 6 (a)

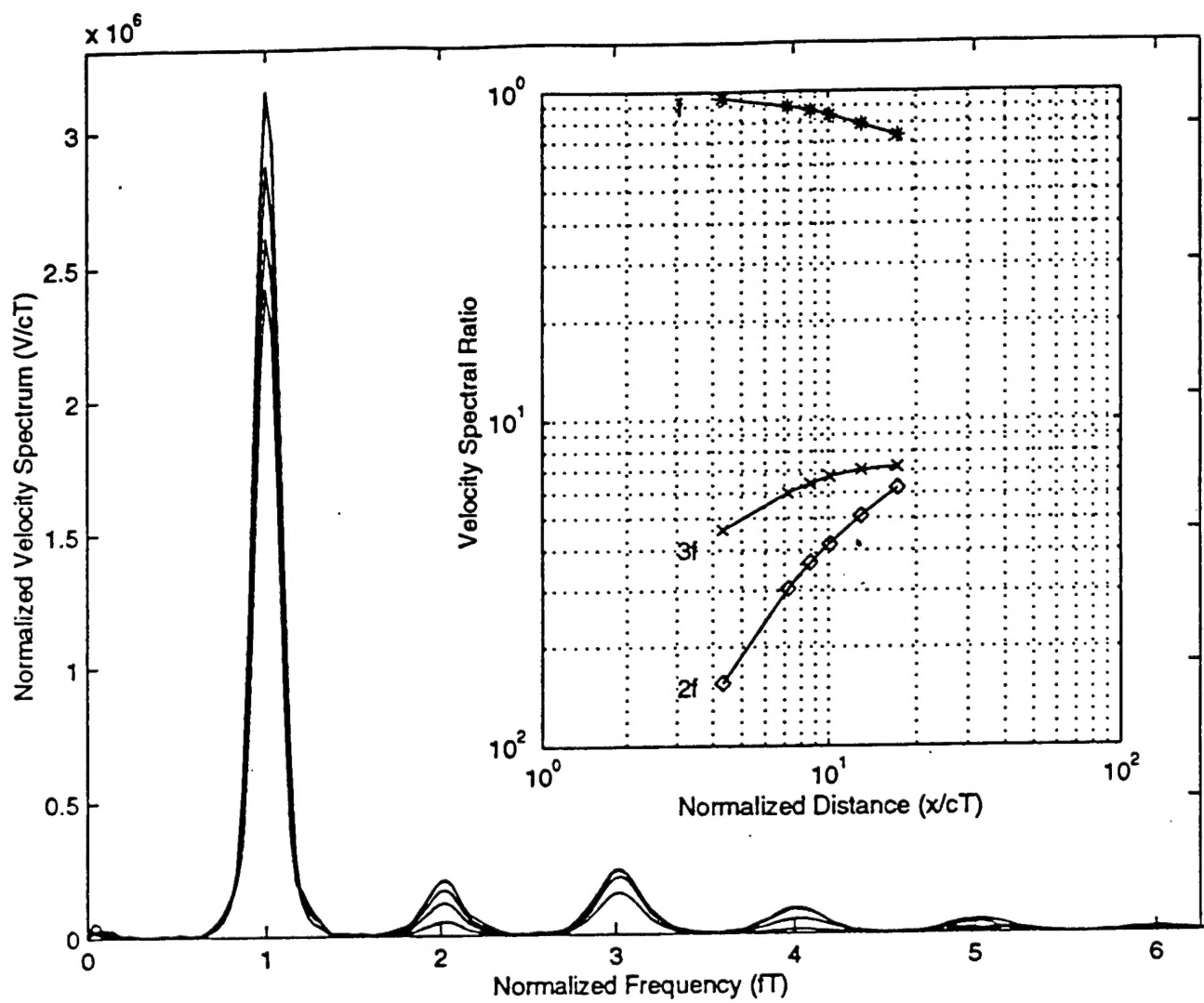


FIGURE 6 (b)

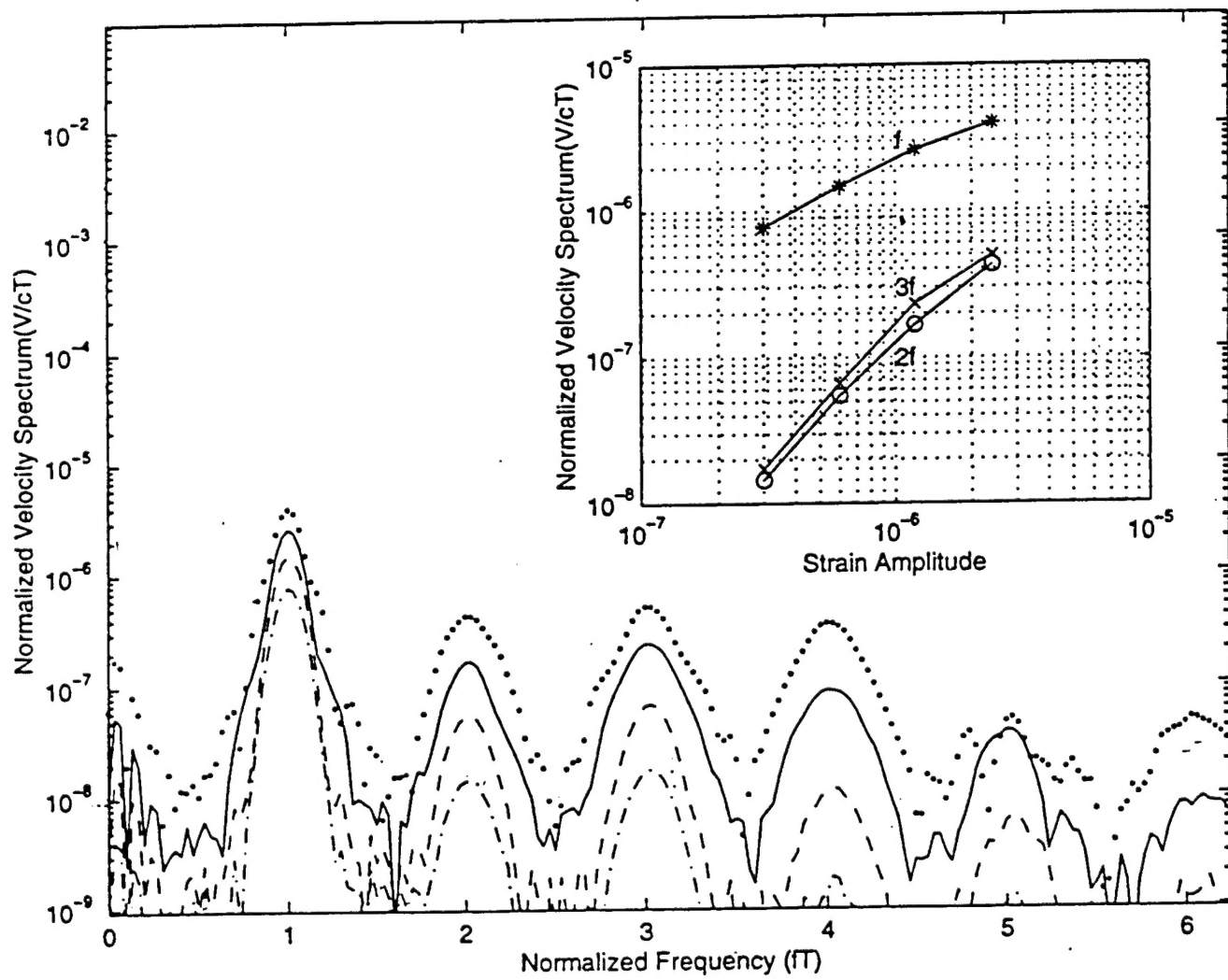


FIGURE 6 (c)

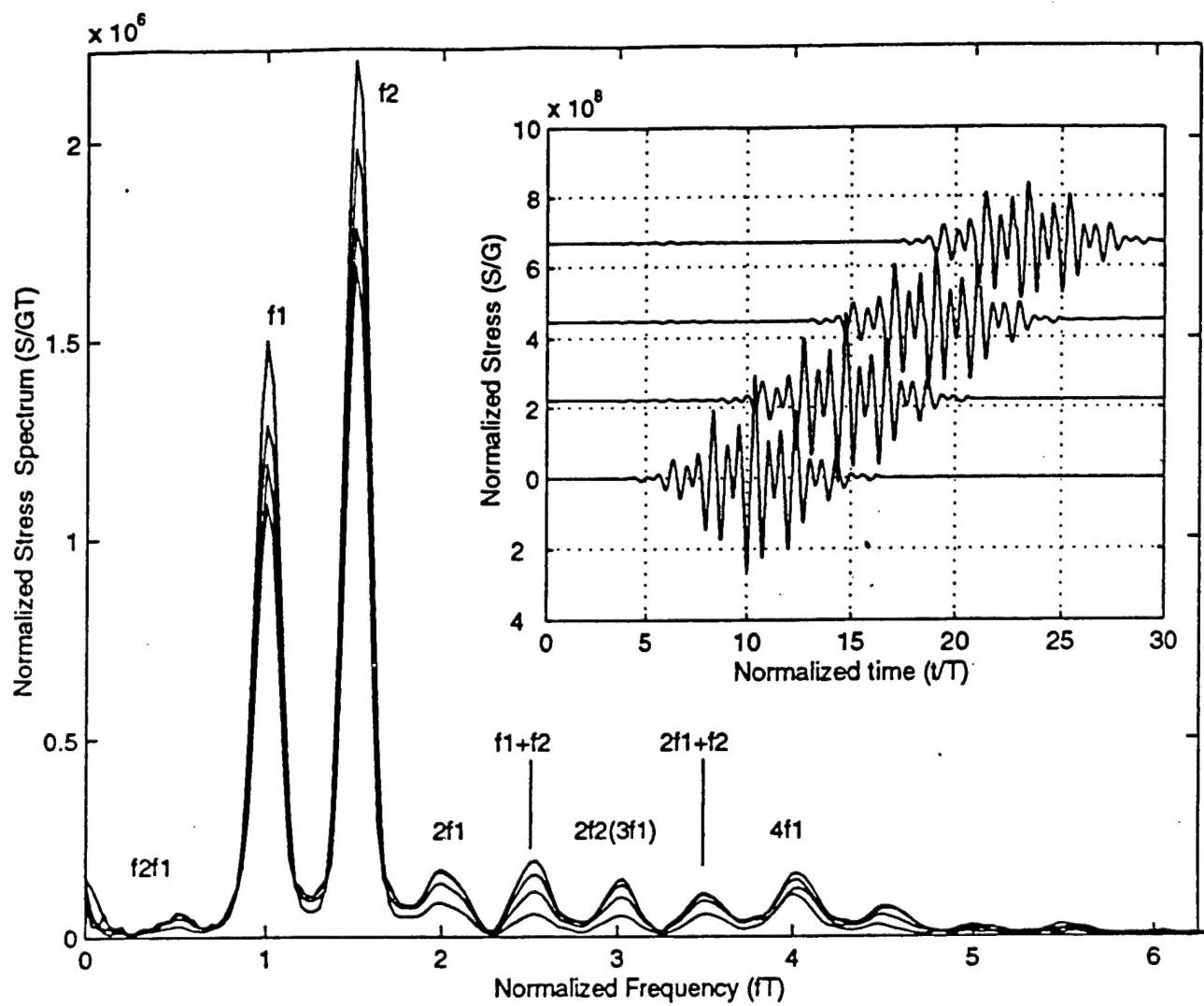


FIGURE 7